UC Berkeley
UC Berkeley Electronic Theses and Dissertations

Title

Stable interface design and characterization in all-solid-state batteries

Permalink

https://escholarship.org/uc/item/5wb0s46n

Author

Tian, Yaosen

Publication Date

2020

Peer reviewed|Thesis/dissertation

eScholarship.org Powered by the California Digital Library
University of California

Stable interface design and characterization in all-solid-state batteries

by

Yaosen Tian

A dissertation submitted in partial satisfaction of the
requirements for the degree of
Doctor of Philosophy
in
Engineering – Materials Science and Engineering

in the
Graduate Division
of the
University of California, Berkeley

Committee in charge:

Professor Gerbrand Ceder, Chair
Professor Mary C. Scott
Professor Bryan D. Mccloskey

Spring 2020

© University of California, Berkeley 2020

Yaosen Tian

All rights reserved.

Abstract

Stable interface design and characterization in all-solid-state batteries

by

Yaosen Tian

Submitted to the Department of Materials Science and Engineering
on February 2020, in partial fulfillment of the
requirements for the degree of
Doctor of Philosophy

Solid-state batteries (SSBs) have received considerable attention due to their reduced flammability and the ability to use high-energy-density metal anodes compared with those of liquid-electrolyte battery systems. Among known inorganic solid electrolytes (SEs), thiophosphates offer the advantage of a combination of high ionic conductivity, low cost and ease of processing, making them strong candidates for large-scale applications. However, thiophosphate electrolytes suffer from poor stability, leading to unstable interfaces upon contact with electrodes. The (electro-)chemical stability of various interfaces in SSBs has become the bottleneck for stable cycling of SSBs.

Thiophosphates are subjected to Li extraction under high voltages. In this thesis, we present a methodology that combines computational and experimental tools to determine the voltage windows of the electrolytes (both the thermodynamic-driven lower bound and kinetic-stabilized upper bound). We demonstrate that sufficient contact between the solid electrolyte and electron source(s) is particularly important in identifying the electrolyte stability window using electrochemical methods. The intrinsic instability of solid electrolyte is related to the capacity loss in solid state batteries, in particular during the first cycle. In this thesis, we also develop a methodology based on *in situ* synchrotron X-ray diffraction techniques to analyze the capacity fade due to electrolyte decomposition in a full-cell SSB.

A thermodynamically stable cathode–electrolyte pair is rare in SSBs. A chemical reaction between the cathode and SE can occur during battery cycling. In this thesis, we employ relatively simple and rapid XRD and SDT experiments to describe the interfacial reactions between electrolytes and electrodes. With the aid of high-throughput density

functional theory calculations, we screen the compatibility between SEs and cathodes in a large chemical space and understand the thermodynamics and kinetics behind the reactions between incompatible electrolyte/electrode pairs.

To suppress the reaction between the cathode and thiophosphate SEs, various cathode coating materials have been developed to serve as a buffer layer and prevent direct contact between the cathode and SE. In this thesis, we directly observe the severity of the interfacial reactions between a thiophosphate electrolyte (Li_2S-P_2S_5) and oxide cathode (NCM) during normal battery operations using different microscopy techniques. A new borate ($Li_3B_{11}O_{18}$) is developed and exhibits excellent oxidation stability and chemical stability, leading to substantially improved performance over cells with Li_2ZrO_3–coated or uncoated cathodes.

The use of Li/Na metal anodes is essential for SSBs to achieve a high energy density. In this thesis, we demonstrate the degradation of the solid electrolyte results in the formation of mixed electronic and ionic conductive decomposition, leading to significantly increased overall cell impedance and poor rate performance. With the aid of first principles computations, we identify passivating products to stabilize the highly reactive interface between a thiophosphate electrolyte (Na_3SbS_4) and Na metal. A passivating interface is constructed through introduction of elements and/or compounds that beneficially reacts with Na metal and forms the passivating products. A general strategy of interface design to stability the electrolyte/metal interface is proposed.

Prof. Gerbrand Ceder, Chair
Professor of Materials Science & Engineering
Daniel M. Tellep Distinguished Professor in Engineering

Dedicated
to my beloved and inspiring parents,

for being the
pillows, role models, catapults,
cheerleading squad and sounding boards
I have needed.

献给我亲爱的父母，
感谢你们
做我曾一直需要的
保护伞、领路人、助推器、啦啦队、策划团。

Acknowledgements

To my advisor, Professor Gerbrand Ceder: Thank you for your guidance and support through my Ph.D. You have been my role model as a scientist with high standards for scientific rigor, big and clear scientific vision and effective communication. I have always been motivated, inspired and invigorated by your passion towards addressing deep and relevant scientific questions. It has been a privilege to see you in action, to have deep discussion with you while you sit on my desk, to listen to your talk and have you give me suggestions on my presentation slide by slide, and to joke with you and laugh out all tough moments in life. You like to walk upstairs, and I start to do so too!

To my first teacher in Ceder Group, Dr. Shou-hang Bo: Thank you for teaching me how to be an experimentalist through days and nights of working in the lab and how to be a researcher through our numerous office discussions and debates, and for guiding me through the vast array of experimental skills necessary for my research.

To my best friends in Ceder Group, Dr. Piero Canepa and Dr. Jaechul Kim: Thank you for the joy and happiness you brought to my Ph.D. life, and for being always available when I needed you!

To my close collaborators in Ceder Group: The projects were made so much more enjoyable by all the members of the Ceder Group who I've had the pleasure of working with, including Juchuan Li, Yaqian Zhang, Jaechul Kim, Yingzhi Sun, Yihan Xiao, Will Richards, Dan Hannah, Tan Shi, Zhengyan Lun, Tina Chen, Huiwen Ji, Piero Canepa, Deok-Hwang Kwon, Bin Ouyang, Luis Barroso-Luque, Raphaele Clement, Valentina Lacivita, Nong Artrith, Howard Tu, Matteo Bianchini, Wenhao Sun, Eric Wang, Penghao Xiao, Jingyang Wang and Haegyum Kim. I'm also grateful for discussion with collaborators including Dr. Lincoln Miara, Dr. Yuichi Aihara from Samsung and Geoff McConohy, Eddie Barks, and Emma Kaeli from the Chueh group in Stanford.

To all my friends in Ceder Group: Thank you all for the good memories. We have worked together days and nights (and midnights in synchrotron beamlines). We have discussed how to improve battery's performance to the extreme. We have debated how to make good and clear slides for Gerd. We have eaten, travelled, played card games, and celebrated holidays. All of these have brought valuable, enjoyable and unique experience to my life in the group.

List of publications（2017-2020）

U.S. Patent:

1. Gerbrand Ceder, **Yaosen Tian**, Yingzhi Sun, Daniel C. Hannah, and Shou-Hang Bo. "Interlayer sodium electrodes for sodium ion batteries." U.S. Patent Application 16/297,385, filed September 12, 2019.

Journal articles:

2. **Yaosen Tian**, Yingzhi Sun, Daniel C. Hannah, Yihan Xiao, Hao Liu, Karena W. Chapman, Shou-Hang Bo, and Gerbrand Ceder. "Reactivity-Guided Interface Design in Na Metal Solid-State Batteries." Joule (2019).
3. **Yaosen Tian**†, Tan Shi†, William D. Richards, Juchuan Li, Jae Chul Kim, Shou-Hang Bo, and Gerbrand Ceder. "Compatibility issues between electrodes and electrolytes in solid-state batteries." Energy & Environmental Science (2017). ***(† equal contribution)***
4. Yaqian Zhang†, **Yaosen Tian**†, Yihan Xiao, Lincoln J. Miara, Yuichi Aihara, Tomoyuki Tsujimura, Tan Shi, Mary C. Scott, and Gerbrand Ceder. "Direct visualization of the interfacial degradation of cathode coatings in solid state batteries: a combined experimental and computational study." Adavnced Emergy Materials, *submitted* ***(† equal contribution)***
5. Bin Ouyang†, **Yaosen Tian**†, Zhengyan Lun, Yaqian Zhang, Tina Chen, Daniil Kitchaev, Zijian Cai, Kelvin Ye, and Gerbrand Ceder. "Zero-strain cathodes of FCC anion framework for Li-ion batteries." *in preparation* ***(† equal contribution)***
6. **Yaosen Tian**†, Guobo Zeng†, Ann Rutt†, Tan Shi†, Haegyeom Kim†, Jingyang Wang, Julius Koettgen, Yingzhi Sun, Bin Ouyang, Tina Chen, Zhengyan Lun, Ziqin Rong, Kristin Persson, and Gerbrand Ceder. "Promises and challenges of next-generation "beyond Li-ion" batteries for electric vehicles and grid decarbonization." Chemical Reviews, *in preparation* ***(† equal contribution)***
7. Tan Shi†, Qingsong Tu†, **Yaosen Tian**, Yihan Xiao, Olga Kononova, Gerbrand Ceder. "High Active Material Loading in All-Solid-State Battery Electrode via Particle Size Optimization." Advanced Energy Materials (2020). ***(† equal contribution)***
8. Huiwen Ji, Jinpeng Wu, Zijian Cai, Jue Liu, Deok-Hwang Kwon, Hyunchul Kim, Alexander Urban, Joe Papp, Emily Foley, **Yaosen Tian**, Mahalingam Balasubramanian,

Haegyeom Kim, Raphaele J. Clement, Bryan D. McCloskey, Wanli Yang and Gerbrand Ceder. "Ultrafast rate capability in high energy density spinel cathodes." Nature Energy (2020).

9. Jingyang Wang, Yan Wang, Dong-Hwa Seo, Tan Shi, Shouping Chen, **Yaosen Tian**, Haegyeom Kim and Gerbrand Ceder. "A High-energy NASICON-type Cathode Material for Na-ion Batteries." Advanced Energy Materials (2020).
10. Zhengyan Lun, Bin Ouyang, Zijian Cai, Raphaële J. Clément, Deok-Hwang Kwon, Jianping Huang, Joseph K. Papp, Mahalingam Balasubramanian, **Yaosen Tian**, Bryan D. McCloskey, Huiwen Ji, Haegyeom Kim, Daniil A. Kitchaev, Gerbrand Ceder. "Design principles for high-capacity Mn-based cation-disordered rocksalt cathodes." Chem (2020).
11. Huiwen Ji, Daniil A. Kitchaev, Zhengyan Lun, Hyunchul Kim, Emily Foley, Deok-Hwang Kwon, **Yaosen Tian** et al. "Computational Investigation and Experimental Realization of Disordered High-Capacity Li-Ion Cathodes Based on Ni Redox." Chemistry of Materials (2019).
12. Zhengyan Lun, Bin Ouyang, Daniil A. Kitchaev, Raphaële J. Clément, Joseph K. Papp, Mahalingam Balasubramanian, **Yaosen Tian**, Teng Lei, Tan Shi, Bryan D McCloskey, Jinhyuk Lee, Gerbrand Ceder. "Improved Cycling Performance of Li-Excess Cation-Disordered Cathode Materials upon Fluorine Substitution." Advanced Energy Materials (2019).
13. Haegyeom Kim, Dong-Hwa Seo, Matteo Bianchini, Raphaële J. Clément, Hyunchul Kim, Jae Chul Kim, **Yaosen Tian**, Tan Shi, Won-Sub Yoon, and Gerbrand Ceder. "A New Strategy for High-Voltage Cathodes for K-Ion Batteries: Stoichiometric $KVPO_4F$." Advanced Energy Materials, (2018).
14. Pieremanuele Canepa, Shou-Hang Bo, Gopalakrishnan Sai Gautam, Baris Key, William D. Richards, Tan Shi, **Yaosen Tian**, Yan Wang, Juchuan Li, and Gerbrand Ceder. "High magnesium mobility in ternary spinel chalcogenides." Nature communications, (2017).
15. Deok-Hwang Kwon, Jinhyuk Lee, Nongnuch Artrith, Lijun Wu, Zhengyan Lun, Hyunchul Kim, **Yaosen Tian**, Yimei Zhu and Gerbrand Ceder. "The impact of surface structure transformations on the performance of Li-excess cathodes." Energy & Environmental Science, *submitted*

Contents

ABSTRACT **1**

ACKNOWLEDGEMENTS ..... **I**

CONTENTS ..... **VII**

LIST OF FIGURES ..... **IX**

LIST OF TABLES ..... **XII**

1. INTRODUCTION **1**

1.1. MOTIVATION AND APPLICATION 1
1.2. OVERVIEW OF SOLID ELECTROLYTES 4
1.3. CHALLENGES IN SOLID-STATE BATTERIES 7
1.4. ORGANIZATION OF THIS THESIS 9

2. COMPATIBILITY BETWEEN CATHODES AND SOLID ELECTROLYTES **11**

2.1. INTRODUCTION 11
2.2. METHODOLOGY 13
2.3. ELECTROCHEMICAL STABILITY OF SOLID ELECTROLYTE 15
2.4. COMPATIBILITY BETWEEN CATHODE AND SOLID ELECTROLYTE 19
2.5. DISCUSSION AND OUTLOOK 29

3. DEVELOPMENT OF BORATE CATHODE COATING AND ANALYSIS OF FIRST CYCLE CAPACITY LOSS IN SOLID-STATE BATTERIES **34**

3.1. INTRODUCTION 34
3.2. DFT COMPUTATION OF COATING STABILITY 36
3.3. EFFECTIVENESS OF LZRO AND LBO COATINGS 38
3.4. INTERFACIAL REACTION(S) BETWEEN NCM AND LPS 46
3.5. INSTABILITY OF LPS AND FIRST-CYCLE CAPACITY LOSS IN SSBS 49
3.6. DISCUSSION AND OUTLOOK 52

4. PASSIVATING INTERFACE DESIGN AND CONSTRUCTION BETWEEN Na_3SbS_4 AND NA METAL **55**

4.1. INTRODUCTION 55
4.2. REVERSE DESIGN AND STABILITY OF NA/Na_3SbS_4 INTERFACE 56
4.3. ELECTROLYTE HYDRATION PROCESS AND DISCOVERY OF $Na_3SbS_4 \cdot 8H_2O$ 62
4.4. INTERFACE STABILIZATION MECHANISM AND CHARACTERIZATION OF INTERFACE PRODUCTS 67
4.5. DISCUSSION 69

5. CONCLUSION REMARKS **72**

APPENDIX A. ENERGY DENSITY ESTIMATION FOR LIBS AND SSBS **74**

APPENDIX B. EXPERIMENT METHODS **75**

APPENDIX B-1. INORGANIC MATERIAL SYNTHESIS 75

APPENDIX B-2. ELECTROCHEMICAL MEASUREMENTS ····77
APPENDIX B-3. MATERIAL CHARACTERIZATION ····78
APPENDIX C. COMPUTATION METHODS ····82
APPENDIX C-1 PHASE DIAGRAMS AND BULK ENERGIES ····82
APPENDIX C-2 VOLTAGE STABILITY CALCULATIONS ····82
APPENDIX C-3 INTERFACIAL STABILITY CALCULATIONS ····83
APPENDIX C-4 ION DIFFUSION CALCULATIONS ····84
APPENDIX D. ADDITIONAL COMPUTATION RESULTS ····85
APPENDIX E. ADDITIONAL EXPERIMENT RESULTS ····91
APPENDIX F. CRYSTAL STRUCTURE OF $NA_3SBS_4 \cdot 8H_2O$ ····94
BIBLIOGRAPHY ····97

List of figures

Figure 1-1 A typical LIB cell and one conception of a lithium metal SSB cell.
Figure 1-2 Specific energy and energy density calculations of LIBs and conceptual SSBs using selected cathode active materials.
Figure 1-3 Progress in discovery of fast Li-ion solid conductors.
Figure 1-4 Progress in discovery of fast Na-ion solid conductors.
Figure 1-5 Interfaces existing in a Li-metal solid-state battery.
Figure 1-6 Ionic conductivity of selected conductors and the corresponding calculated oxidation and reduction limits.
Figure 1-7 Schematic illustration of major issues in SSB fabrication and cycling.
Figure 2-1 Calculated stability window and decomposition products for Na_3PS_4.
Figure 2-2 Calculated stability window and decomposition products for Na_3PSe_4.
Figure 2-3 Electrochemical cycling of the Na_3PX_4 (mixed with carbon) cathode composite at constant current.
Figure 2-4 Diffraction patterns of the Na_3PX_4 cathode composite before and after being fully charged/discharged.
Figure 2-5 XRD patterns of the reaction products of (a) $NaCrO_2$ and Na_3PS_4 at RT, 300°C, 500°C, and 700°C, and (b) $NaCrO_2$ and Na_3PSe_4 at RT (25°C), 300°C, and 500°C.
Figure 2-6 TGA measurements (total weight) of the reactions between (a) $NaCrO_2$ and Na_3PS_4 and (b) $NaCrO_2$ and Na_3PSe_4.
Figure 2-7 Diffraction patterns of desodiated compound(s) of (a) $NaCrO_2$, (b) $NaFeO_2$, (c) $NaCoO_2$, and (d) $NaNiO_2$.
Figure 2-8 XRD results for reaction between (a) $Na_{0.5}CrO_2$ and Na_3PS_4 and (b) $Na_{0.5}CrO_2$ and Na_3PSe_4 at RT (25°C) and 300°C.
Figure 2-9 DSC results for reaction between (a) $Na_{0.5}CrO_2$ and Na_3PS_4 and (b) $Na_{0.5}CrO_2$ and Na_3PSe_4.
Figure 2-10 XPS spectra of Cr 2p from the surfaces of (a) mixture of $Na_{0.5}CrO_2$ and Na_3PS_4 at RT (25°C), (b) mixture of $Na_{0.5}CrO_2$ and Na_3PSe_4 at RT (25°C), (c) $Na_{0.5}CrO_2$, and (d) $NaCrO_2$.
Figure 3-1 DFT computation of stability of Li_2ZrO_3 (LZrO) and $Li_3B_{11}O_{18}$ (LBO) coatings. (a) Stability window of LPS, LZrO and LBO. (b) Chemical reactivity energies (in meV/atom) of reaction pairs among NCM^{523}, LPS, LZrO, and LBO.
Figure 3-2 Coating procedure using a sol-gel method. The precursors of the LBO coating are shown in the figure.
Figure 3-3 SEM, TEM, and HRTEM images of the morphology of uncoated/coated NCM^{523} particles: (a-c) uncoated NCM^{523}, (d-f) LZrO-coated NCM^{523}, and (g-i) LBO-coated NCM^{523}. The scale bars are presented individually.
Figure 3-4 Electrochemical cycling of full cells using uncoated (grey), LZrO-coated (blue), and LBO-coated (red) NCM^{523} cathodes: discharge capacity (a) and capacity retention (b).
Figure 3-5 Electrochemical cycling of full cells using uncoated NCM^{523} cathodes.
Figure 3-6 Electrochemical cycling of full cells using LZrO-coated NCM^{523} cathodes.
Figure 3-7 Electrochemical cycling of full cells using LBO-coated NCM^{523} cathodes.
Figure 3-8 Comparison of LZrO- and LBO- coated NCM^{523} cathode composite prior to electrochemical cycling and after 1st cycle.
Figure 3-9 LZrO-coated NCM^{523} cathode composite after 1st cycle.
Figure 3-10 LBO-coated NCM^{523} cathode composite after 10 cycles.

Figure 3-11 LZrO-coated NCM^{523} cathode composite after 50 cycles.
Figure 3-12 LZrO/LBO coated NCM^{523} cathode composite after 50 cycles.
Figure 3-13 HAADF-STEM image and EDX mappings of LBO coated NCM^{523} after 50 cycles.
Figure 3-13 SSB cell for *in situ* synchrotron XRD measurement.
Figure 3-14 *In situ* XRD and electrochemical cycling of full-cell SSB using LBO-coated NCM^{523} active cathode.
Figure 3-15 Lattice parameters of NCM^{523} during electrochemical cycling.
Figure 3-17 SEM images of cathode composite of LBO-coated NCM^{523}, LPS, and CNF ground using different forces.
Figure 3-18 Electrochemical cycling of cathode composite of LBO-coated NCM^{523}, LPS, and CNF ground using different forces.
Figure 4-1 Synchrotron X-ray diffraction pattern and Rietveld refinement of the Na_3SbS_4.
Figure 4-2 EIS data of Na_3SbS_4 switched by electrodes at temperatures ranging from 25 °C to 80 °C.
Figure 4-3 Arrhenius plot for total Na-ion conductivity obtained from EIS analysis.
Figure 4-4 Galvanostatic cycling of Na/Na_3SbS_4/Na symmetric cells with (orange) and without (grey) surface hydration pretreatment at a current density of 0.1 mA cm^{-2}.
Figure 4-5 SXRD pattern and Rietveld refinement of Na_3SbS_4/Na interface products.
Figure 4-6 Comparison of surface of solid-state electrolyte pellet before and after contact with Na metal and electrochemistry cycling.
Figure 4-7 SEM images of the surface of Na_3SbS_4 pellet after air exposure for different durations.
Figure 4-8 Schematic illustration of solid electrolyte/Na metal interface before (left) and after (right) electrochemical cycling.
Figure 4-9 Voltage of Na/Na_3SbS_4/Na symmetric cells after different surface hydration pretreatment durations before (grey) and after (red) 25 cycles.
Figure 4-10 SXRD patterns of Na_3SbS_4 after different durations of air exposure.
Figure 4-11 (a) SXRD pattern and Rietveld refinement of Na_3SbS_4 after 10 min of air exposure. **(b)** Crystal structure viewed along the [001] direction of $Na_3SbS_4{\cdot}8H_2O$.
Figure 4-12 Na vacancy migration barriers and transport mechanism in $Na_3SbS_4{\cdot}8H_2O$ and $Na_3SbS_4{\cdot}9H_2O$.
Figure 4-13 Spatially resolved *post-operando* SXRD profiles of Na/Na_3SbS_4/Na symmetric cell with surface hydrate coating.
Figure 4-14 Comparison of *ex situ* and *post-operando* synchrotron XRD patterns of Na/$Na_3SbS_4{\cdot}8H_2O$ interface.

Figure E-1 (a–b) Diffraction patterns of $NaCrO_2$, Na_3PX_4, and mixture of the paired materials at RT (25°C); the tick marks indicate $NaCrO_2$ (purple, top) and Na_3PX_4 (orange for Na_3PSe_4, pink for Na_3PS_4, bottom) peaks. The diffraction pattern of the mixed materials is almost the same as the sum of those of each individual component, suggesting that no bulk reaction occurs between $NaCrO_2$ and Na_3PX_4 after mixing at RT.
Figure E-1 (c–d) Diffraction patterns of $NaMnO_2$, Na_3PX_4, and a mixture of the paired materials at RT (25°C); the tick marks indicate $NaMnO_2$ (purple, top) and Na_3PX_4 (orange for Na_3PSe_4, pink for Na_3PS_4, bottom) peaks. No bulk reaction is observed between $NaMnO_2$ and Na_3PX_4 after mixing at RT.
Figure E-1 (e–f) Diffraction patterns of $NaFeO_2$, Na_3PX_4, and a mixture of the paired materials RT (25°C); the tick marks indicate $NaFeO_2$ (purple, top) and Na_3PX_4 (orange for Na_3PSe_4, pink for Na_3PS_4, bottom) peaks. Peak shifts are observed in (e) at 30°, 39°, and 46°, indicating that $NaFeO_2$ reacts with Na_3PSe_4 at RT. Note that only peak shifts of Na_3PSe_4 are observed (one peak of

$NaFeO_2$ is marked as reference). No bulk reaction is observed between $NaCrO_2$ and Na_3PS_4 after mixing at RT in (f).

Figure E-1 (g–h) Diffraction patterns of $NaCoO_2$, Na_3PX_4, and a mixture of the paired materials at RT (25°C); the tick marks indicate $NaCoO_2$ (purple, top) and Na_3PX_4 (orange for Na_3PSe_4, pink for Na_3PS_4, bottom) peaks. Peak shape changes are observed in (g) at 30° and 46°, indicating that $NaCoO_2$ reacts with Na_3PSe_4 at RT. No bulk reaction is observed between $NaCoO_2$ and Na_3PS_4 after mixing at RT in (h).

Figure E-1 (i–j) Diffraction patterns of $NaNiO_2$, Na_3PX_4, and a mixture of the paired materials at RT (25°C); the tick marks indicate $NaNiO_2$ (purple, top) and Na_3PX_4 (orange for Na_3PSe_4, pink for Na_3PS_4, bottom) peaks. Peak shape changes are observed in (i) at 30°, 39°, and 46°, indicating that $NaNiO_2$ reacts with Na_3PSe_4 at RT. No bulk reaction is observed between $NaNiO_2$ and Na_3PS_4 after mixing at RT in (j).

Figure F-1 The linkage between $Na(H_2O,S)_6$ octahedra and SbS_4 tetrahedra in $Na_3SbS_4 \cdot 8H_2O$ forming corrugated layers parallel to (010).

Figure F-2 Different Na diffusion channels in $Na_3SbS_4 \cdot 8H_2O$. Three channels are identified: Na(1)–Na(3)–Na(3)–Na(1)–…, Na(2)–Na(4)–Na(4)–Na(2)–…, and Na(4)–Na(2)–Na(4)–Na(3)–Na(1)–Na(3)–….

List of tables

TABLE 2-1 COMPARISONS OF THE VARIOUS STABILITY WINDOWS OBTAINED THEORETICALLY AND EXPERIMENTALLY FOR Na_3PX_4

TABLE 2-2 DFT CALCULATIONS FOR THE PRODUCTS OF THE REACTION BETWEEN Na_xMO_2 (x = 0.5 OR 1.0) AND Na_3PX_4.

TABLE 2-3 ONSET TEMPERATURES OF THE REACTIONS BETWEEN $NaMO_2$ AND Na_3PX_4

TABLE 2-4 XPS DATA FITTING RESULTS FOR CR 2P PEAKS

TABLE 3-1 FIRST CYCLE CAPACITY OF LBO-COATED NCM^{523} CYCLED IN DIFFERENT SSB CELLS

TABLE 4-1 CRYSTALLOGRAPHIC DATA FOR $Na_3SbS_4 \cdot 8H_2O$ BASED ON RIETVELD REFINEMENT OF THE SYNCHROTRON XRD DATA.

TABLE B-1 SYNTHESIS CONDITIONS OF $NaMO_2$ CATHODE MATERIALS

TABLE D-1 DFT CALCULATIONS FOR ALL POSSIBLE PRODUCTS OF THE REACTION BETWEEN Na_xMO_2 (x = 0.5 OR 1.0) AND Na_3PX_4

TABLE D-2 REACTIONS BETWEEN CATHODE/SE, CATHODE/COATING, AND COATING/SE WITH THE MAXIMUM DRIVING FORCE

TABLE D-3 DECOMPOSITION PRODUCTS OF Na_3SbS_4 AT VARIOUS NA CHEMICAL POTENTIALS CALCULATED BY DFT

TABLE D-4 DECOMPOSITION PRODUCTS OF $Na_3SbS_4 \cdot 9H_2O$ AT VARIOUS NA CHEMICAL POTENTIALS CALCULATED BY DFT

TABLE D-5 DECOMPOSITION OF NA-CONTAINING HYDRATED COMPOUND IN THE MATERIALS PROJECT DATABASE WITH NA METAL

TABLE D-6 DECOMPOSITION OF LI-CONTAINING HYDRATED COMPOUND IN THE MATERIALS PROJECT DATABASE WITH LI METAL

TABLE F-1 ATOMIC SITE INFORMATION FOR $Na_3SbS_4 \cdot 8H_2O$ BASED ON RIETVELD REFINEMENT OF SYNCHROTRON XRD DATA. THE ATOMIC COORDINATES FOR HYDROGEN ATOMS FROM THE ISOSTRUCTURAL COMPOUND OF $Na_3AsS_4.8D_2O$ WERE ADOPTED AND WERE FIXED DURING THE REFINEMENT.

Chapter 1.

Introduction

1.1. Motivation and application

Li-ion batteries (LIBs), first commercialized by Sony in 1991 (*1*), are transforming people's life in the 21st century. The sustained improvement in performance of LIBs have made them the technology of choice for electrical energy storage (*2*). LIBs are now the only rechargeable battery other than lead-acid batteries produced at > 5 GWh yr^{-1}, with a worldwide manufacturing expansion reaching hundreds of GWh yr^{-1} over the next five years(*3*). The specific energy of LIBs increased from approximately 90 Wh kg^{-1} at the cell level in the 1990s to over 250 Wh kg^{-1} today (*4*), which has enabled their successful application in portable electronics and electric vehicles (EVs). In 2018, the global EV fleet exceeded 5.1 million vehicles, up 2 million from the previous year, with the number of new electric car sales almost doubling (*4–6*). By 2025, Norway aims to have 100% of its cars be either an electric or plug-in hybrid unit, and the Netherlands plans to ban all gasoline and diesel car sales by the same year. By 2030, Germany plans to ban internal combustion engines, and by 2040, France and Great Britain aim to end their gasoline and diesel car sales (*7*).

Over decades of development, the cell architecture and electrode material options for LIBs have been established. Olivines (e.g., $LiFePO_4$, i.e., LFP), layered oxides (e.g., $LiNi_{0.8}Co_{0.15}Al_{0.05}O_2$, i.e., NCA), and spinels (e.g., $LiMn_2O_4$, i.e., LMO) are typically used as the cathodes, which are separated from a graphite anode by a polymer separator(s) immersed in a carbonate-based organic liquid electrolyte (**Figure 1-1**). Both the cathode and the anode are Li intercalation materials, which allows Li to be reversibly incorporated or removed from their host crystal structures. Important design goals for LIBs include high energy and power densities, high cycling stability, good safety and low costs (*5*). While the cost of LIB modules has been significantly reduced from over 1,000 USD kWh^{-1} to lower than 200 USD kWh^{-1} today because of the manufacturing improvements (*7*), the materials-level advancements in LIBs are approaching a fundamental limit (*8*). Today's Li-ion chemistry is maturing with $Li(Ni,Co,Mn)O_2$ (i.e., NCM) compounds dominating the cathode, and graphite still almost exclusively used for the anode. NCM cathodes have evolved from compounds with equal amounts of Ni, Co, Mn "111" to high Ni content materials such as "622", "811" (the numbers specify the relative amount of Ni, Co and Mn). The higher Ni content lowers the charging voltage at the top of charge thereby enabling higher capacity, but the gains from further modifying the cathode are

becoming increasingly limited. In 2017, targets of 350 Wh kg^{-1} and 750 Wh L^{-1} at the cell level for automotive batteries by 2020 were proposed by the U.S. Department of Energy (DOE) and U.S. Advanced Battery Consortium (USABC) (*9–11*). The demands for higher energy density to further extend the driving distance in future EVs and higher power density to satisfy typical driving patterns have triggered the investigation of technologies beyond conventional Li-ion batteries.

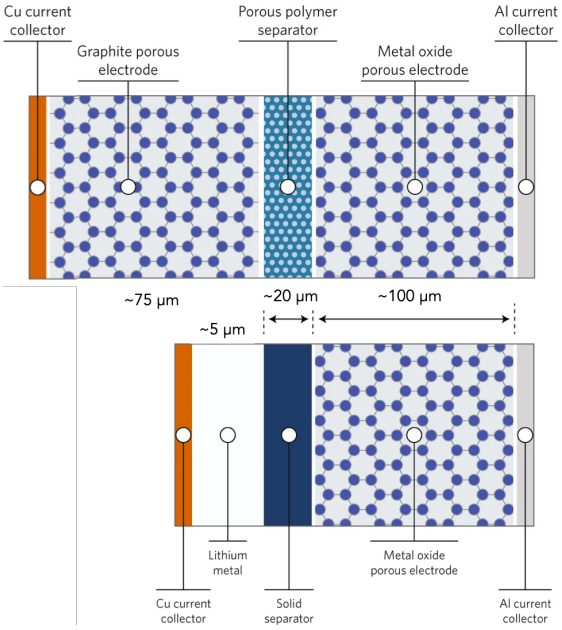


Figure 1-1 A typical LIB cell (top) and one conception of a lithium metal SSB cell (bottom). The SSB cell contains a solid separator and a dense layer of metallic lithium (2).

Replacing the graphite anode with Li metal would provide a path to significantly increase the energy density of today's LIBs. However, the flammability of organic solvent electrolytes and the high tendency of dendrite formation raise serious concern for using Li metal in current LIBs. When thermal runway occurs as a result of electrical or mechanical abuse, the liquid electrolyte undergoes a rapid exothermic decomposition reaction, which can potentially lead to fires or explosions. After several widely publicized safety incidents involving both consumer electronics and EVs (*12*, *13*), the safety of LIBs has received considerable attention from both the battery industry and the public. Solid-electrolyte materials have been proposed as a viable non-flammable to organic electrolytes in lithium batteries, and may also aid in solving the SEI formation problem (*14*). In solid-state batteries (SSBs), an inorganic solid conductor is used as the medium to transport working ions and a separator between the anode and cathode (**Figure 1-1**). The composite cathode is composed of the mixture of active cathode, solid electrolyte and conductive carbon. Compared with current LIBs, SSBs are better suited for utilizing

a Li metal anode because the safety concerns are partially eliminated by using an inorganic solid electrolyte (SE). Because of the reduction in volume and mass associated with the use of a Li metal anode (with a high theoretical specific capacity of 3860 mAh g^{-1}.), SSBs can potentially provide a significantly increased energy density over current LIBs, making them great candidates for future EV batteries. In fact, several major automotive companies have targeted the mid-2020s to begin using SSBs in EVs (*15–18*). **Figure 1-2** compares the specific energy and volumetric energy densities at the cell level of the common cathodes used in a typical LIB and a hypothetical Li-metal SSB. Multiple selected Li-ion cathodes deliver volumetric energy densities larger than 750 Wh L^{-1} at the cell level in the SSB, with a maximum volumetric energy density of 1373.8 Wh L^{-1} reached using the NCA cathode. Although these comparisons do not represent the optimal cell-level energy densities of various SSB systems, these comparisons demonstrate the significant energy density increase that can be achieved using established LIB cathodes in a SSB configuration. SSBs also allow bi-polar electrode stacking cell design, which can reduce the overall current collector thickness as well as the "dead volume" between cells (*19*).

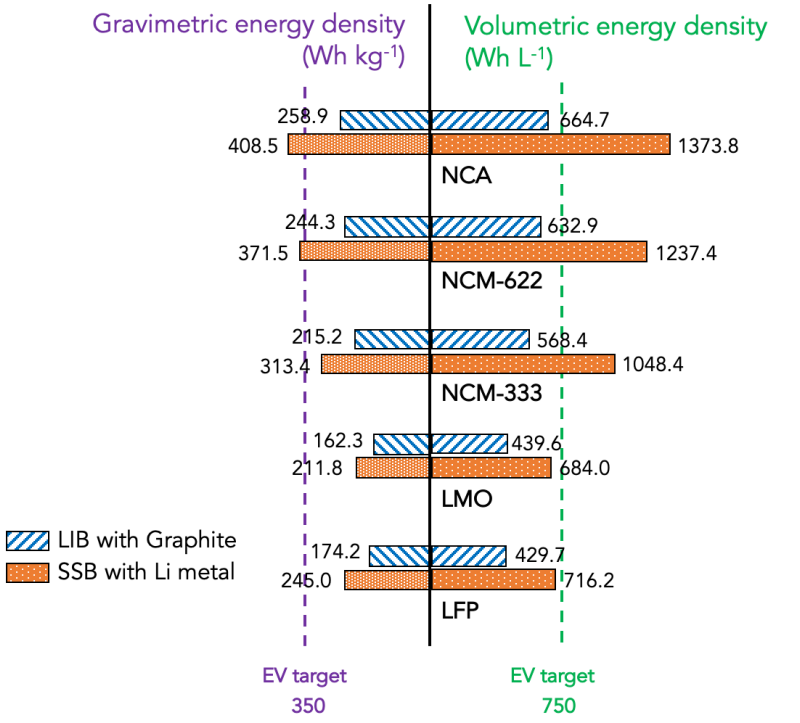


Figure 1-2 Specific energy and energy density calculations of LIBs and conceptual SSBs using selected cathode active materials. [1]

[1] The inputs employ data from the BatPaC model (*20*). Assumptions and detailed calculation method are described in the **Appendix A**.

1.2. Overview of solid electrolytes

Over the past two decades, great strides have been made towards the commercialization of SSBs with the discovery of a wide variety of fast solid ionic conductors (*21*, *22*), which has resulted in many newly discovered conductors with ionic conductivity close to or even surpassing that of liquid electrolyte. A multitude of fast Li-ion conductors have emerged in recent years, as shown in **Figure 1-3**. The ionic conductivities of many of these conductors, such as garnet-type materials, argyrodite-type materials, and LISICON materials, can approach or even surpass those of currently used liquid electrolytes ($\sim 10^{-2}$ S cm^{-1}) (*19*, *23–35*). The intensive development of Li-ion conductors has also led to a renaissance in the search for fast Na-ion conductors (**Figure 1-4**). After reports of several fast Na-ion conductors more than 15 years ago, such as β-Al_2O_3 and NASICON-type materials (*36–39*), there were no additional reports on novel Na-ion conductors until 2012. Recently, researchers have revisited this field, and many new fast Na-ion conductors have been demonstrated(*25*, *40–47*), some of which exhibit very high ionic conductivities up to 70 mS cm^{-1}.

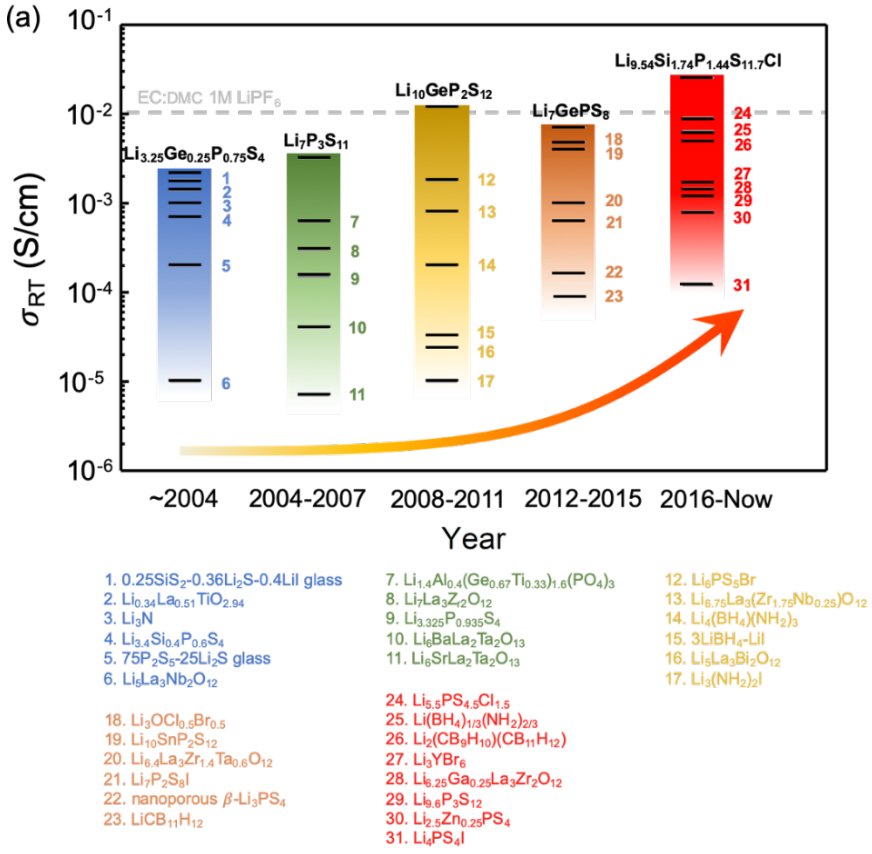


Figure 1-3 Progress in discovery of fast Li-ion solid conductors

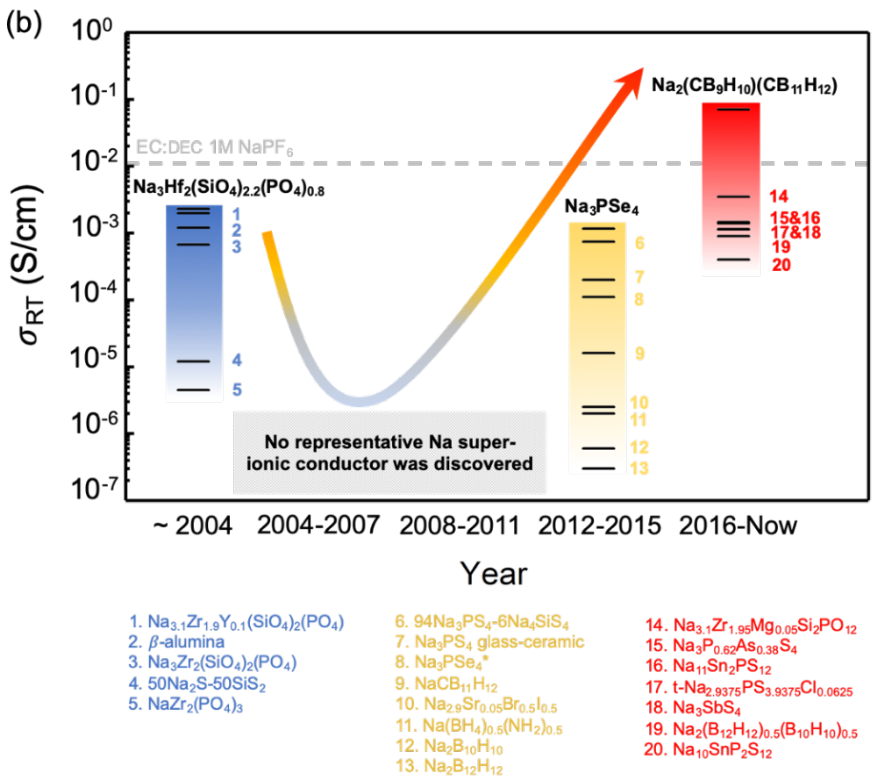


Figure 1-4 Progress in discovery of fast Na-ion solid conductors

With the development of fast ion conductors, growing understandings of the underlying chemical and structural factors that govern the ion mobility have achieved in recent years. The cation mobility generally follows the Arrhenius equation **(1-1)**:

$$\sigma = \frac{A}{T} n_c e^{-\frac{E_A}{RT}} \qquad \textbf{(1-1)}$$

in which A is a constant related to the crystal structure, n_c is the concentration of working ion carriers (e.g., vacancy or interstitial), E_A is the activation energy for ion transport, T is temperature in K, and k_B is the Boltzmann constant.

A low activation energy (i.e., E_A) is critical for achieving high ionic conductivity (i.e., σ). The activation energy is determined by the energy landscape along the working-ion diffusion path. A flat energy landscape, where the displacement of the working ion only causes a small change in structure energy, usually corresponds to a low activation energy. To flatten the energy landscape, the coordination changes along the diffusion path must be minimized. It was demonstrated that a body-centered cubic (bcc)-like anion framework, where Li can directly hop between adjacent tetrahedral sites, can provide a

reduced activation energy compared with other close-packed frameworks, where Li must hop along a tetrahedral-octahedral-tetrahedral path (*48*).

The interaction of the working ion and the other cations also has an impact on the conductivity. Different anion chemistries exhibit different "screening" effects of the non-Li cations, thus also affects the conductivity. In general, S^{2-} can provide a better screening protection than O^{2-} due to the larger ion size. The larger and more polarizable sulfur anions better screen the central cation in the structural framework (such as the P^{5+} in PS_4^{3-}), which reduces the interaction between the central cation and migrating cation. Therefore, for materials with the same structure but different anion species, such as the argyrodite-type materials Li_6PO_5Cl and Li_6PS_5Cl, sulfides usually exhibit higher ionic conductivities than oxides (*35*). Because of the higher degree of freedom of a polyanion, replacing a monatomic anion with a polyanion provides another way to flatten the energy landscape and reduce the activation energy. For example, the ionic conductivity of sodium anti-perovskite Na_3OX (X= Cl, Br, I, etc.) can be increased by four orders of magnitudes by substituting the halide anion with the BH_4^- group (*49*).

In most structures, the working ion diffuses via a vacancy or interstitial diffusion mechanism. Therefore, the cation vacancy and interstitial defect concentration (i.e., n_c) is another critical factor in determining the ionic conductivity of most materials. This defect concentration can usually be tuned by aliovalent doping. For example, Ca doping can be used to create Na vacancies in cubic Na_3PS_4 to obtain a high room-temperature ionic conductivity of ~1 mS cm^{-1} (*50*) and Zr doping has been reported to increase the ionic conductivity of $LiTaSiO_5$ by introducing interstitial Li ions (*51*). In some cases, a large amount of excess migrating ions can push the ions to occupy high-energy sites ("Li-stuffed" materials), which flattens the energy landscape and lowers the activation barrier. For example, the well-known garnet-type ionic conductor $Li_7La_3Zr_2O_{12}$ exhibits a high ionic conductivity of 0.3 mS cm^{-1}, whereas materials with the same garnet-type structure but lower Li concentrations, $Li_5La_3Nb_2O_{12}$ and $Li_3La_3Te_2O_{12}$, exhibit much lower ionic conductivities. It was shown in a garnet-type $Li_xLa_3M_2O_{12}$ (M=Te, Nb, Zr) ionic conductor, as the Li concentration increases from $x = 3$ to $x = 7$, more Li ions are pushed to the high-energy octahedral sites to minimize the interaction between adjacent Li ions (*52*). As a result of the higher Li site energy, the energy barrier along the Li diffusion path is greatly lowered with higher Li content (*52*). In addition, Mo and co-workers argued that the strong mobile-ion interaction resulting from their high concentration can lead to multi-ion correlated migration with a reduced migration energy barrier (*53*). These Li-excess or "Li-stuffed" materials provide a new route for the design of superionic conductors.

1.3. Challenges in solid-state batteries

Despite the rapid development of superionic solid conductors with increasing conductivities, the energy density of SSBs cannot yet surpass conventional Li-ion batteries, in part because of the complex interface structures between solids in SSBs (**Figure 1-5**). The interfacial issues of the interparticle interfaces within composite cathode lead to a low utilization of active materials, capacity fade with limited cycle life, and poor rate performance (*14*, *54–56*). This includes the electrochemical decomposition of solid conductors, chemical reaction and interphase formation between solid conductor and high voltage cathodes. When the cathode expands or contracts over cycling, the periodic structure and/or volume change may also result in mechanical particle-to-particle contact loss because most SEs do not deform easily. The strong reaction and/or poor wetting between solid electrolyte and Li/Na metal anode lead to a severely increased interface impedance. All these interfacial instability issues create a large cell overpotential, resulting in low energy density and severe capacity fade.

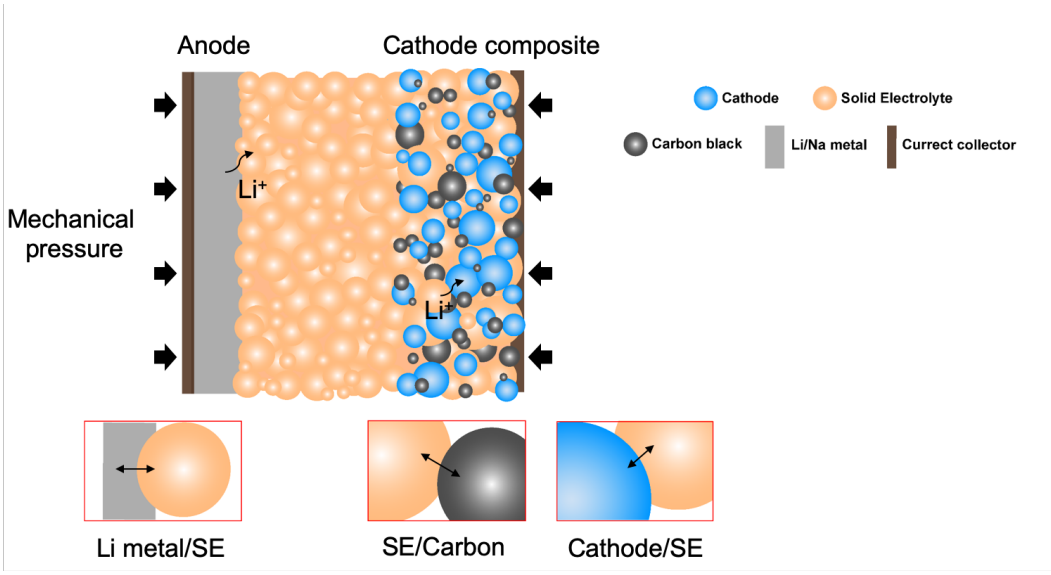


Figure 1-5 Interfaces existing in a Li-metal solid-state battery.[2]

A variety of interfaces exist in a full SSB cell, as illustrated schematically in **Figure 1-5**. The stability of each interface in SSBs falls into one of following three main categories (*58–60*):

[2] Figure adapted from ref. (*57*)

Type A - thermodynamically stable interface, where no reaction occurs.

Type B - reacting to form a mixed conducting interphase (MCI), where both electrons and ions are conductive which allows the reaction to continue and the interphase to grow.

Type C - reacting to form a stable solid-electrolyte interphase (SEI), which limits further reaction by being electronically insulating.

For long-term good battery performance, it is critical that all interfaces are either Type A or Type C. In practice, thermodynamically stable (i.e., interface of Type A) is difficult to achieve(*14*, *61*). Whether or not the type C interface is ionically conductive is critical for battery performance in many systems (*60*). In cathode composite the interface between the active cathode material and the solid electrolyte must allow for fast lithium transfer. However, this is a difficult requirement as many high conductivity electrolytes have narrow stability windows (**Figure 1-6**), which experiences intrinsic instability under high voltages and/or strong reactivity with highly charged active cathode. The interface instability at the anode side, on the other hand, are slightly different, which are always initiated by reduction of the solid electrolyte by the alkali metal anode, leading to a MCI layer (*62*, *63*).

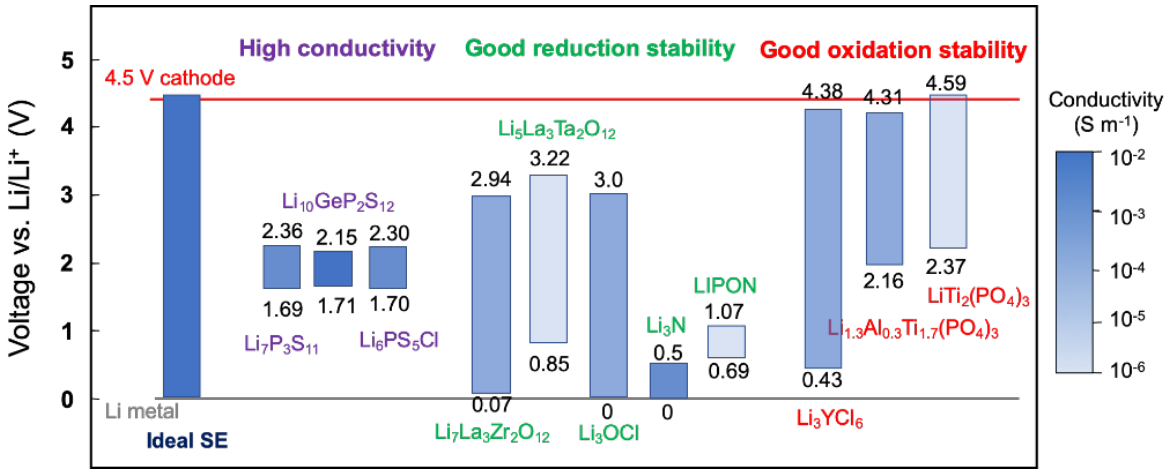


Figure 1-6 Ionic conductivity of selected conductors and the corresponding calculated oxidation and reduction limits. An ideal SE (shown as the bar on the left side) should present ionic conductivity higher than 10^{-2} S m^{-1} (conductivity of typical liquid electrolytes), stability with Li or Na metal anode, and wide stability window that spans the full cycling voltage range.

In addition to the interface problems, Li metal dendrite formation and growth (*64–68*) need be overcome to realize the large-scale production of high-energy-density SSBs with long cycle life. Other practical issues also limit the energy density of current SSBs, such

as contact loss between cathode and electrolyte, thick SE separators and low cathode loading(*39*, *55*, *56*, *69*, *70*). A summary of the major issues in SSB fabrication and cycling are illustrated in **Figure 1-7**.

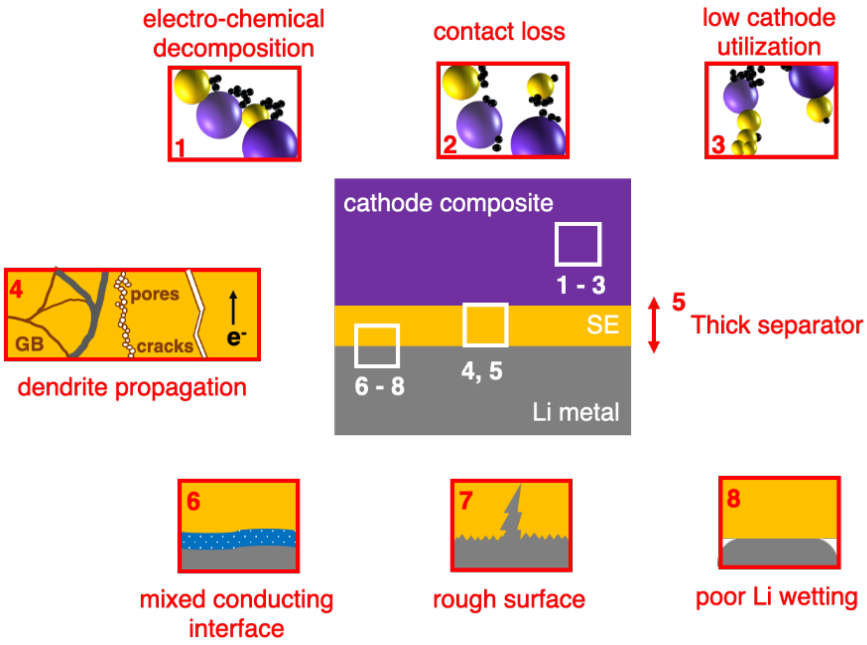


Figure 1-7 Schematic illustration of major issues in SSB fabrication and cycling.

1.4. Organization of this thesis

The work in this thesis was undertaken with the broad goals of 1) investigation and understanding of the interfacial reactions leading to high interfacial resistance at the electrodes, 2) the design and construction of stable electrode/electrolyte interface.

Chapter 2 discusses the intrinsic electrochemical stability of solid electrolyte materials, which is relevant wherever the electrolyte contacts an electron pathway, and the electrochemical reactivity of the cathode/electrolyte pairs. We combine density functional theory calculations and simple experimental techniques such as X-ray diffraction, simultaneous differential scanning calorimetry and thermal gravimetric analysis, and electrochemistry to efficiently screen the compatibility of numerous electrode/electrolyte pairs, and to accurately evaluate the stability window of solid electrolytes. In **Chapter 3**, we observe the interfacial reactions in cathode composite during normal battery operations at a microscopic view. We also identify a new borate cathode coating that exhibits high oxidation stability and chemical stability with both oxide cathode and thiophosphate electrolyte, which protects the cathode/electrolyte

interface, and further allows a detailed analysis of the first-cycle capacity loss in a SSB due to the electrolyte electrochemical instability. In **Chapter 4**, we employ a 'reverse design' strategy to improve the stability of the interface between a solid-state electrolyte and the Li/Na metal anode. A protective hydrate coating is identified to generate a passivating interface between the Na_3SbS_4 and Na metal. The buried interface between the surface-treated solid-state electrolyte and sodium metal is characterized using *post-operando* synchrotron X-ray depth-profiling, providing spatially resolved evidence of the multilayered phase distribution in the Na metal symmetric cell consistent with the theoretical predictions.

Chapter 2.

Compatibility between cathodes and solid electrolytes

Remarkable success has been achieved in the discovery of ceramic alkali superionic conductors as electrolytes in solid-state batteries, but finding a stable interface between electrode and electrolyte is difficult. Detailed characterizations of the complex inter-particle interfaces existing in cathode composite of solid-state batteries are difficult, in part due to the expensive instrumentation requirement and/or special cell designs. Without simple but powerful tools, such compatibility issues cannot be systematically investigated, and thus, hindering the generalization of design rules for the integration of solid-state battery components. In this chapter, we present a methodology combining DFT calculations and simple experimental tests such as XRD, SDT and electrochemistry that can accurately determine the voltage window of solid electrolytes and efficiently screen the compatibility between large numbers of electrode/electrolyte pairs. Employing Na solid state system as an example, we demonstrated the efficiency of the method by finding the most stable cathode/electrolyte pair within a chosen chemical space (more than 20 different combinations of electrodes and electrolytes). Important selection criteria for the cathode and electrolyte in solid state batteries are also derived.

The content of this chapter is based, often verbatim, on two following manuscripts which are published or in preparation for publication. Some results presented in this chapter were obtained by a collaborative effort. Contribution from collaborators are made explicit in relevant results.

[1] Yaosen Tian†, Tan Shi†, William D. Richards, Gerbrand Ceder, et al. "Compatibility issues between electrodes and electrolytes in solid-state batteries." Energy & Environmental Science (2017). († equal contribution)

[2] Yaosen Tian†, Guobo Zeng†, Ann Rutt†, Tan Shi†, Haegyeom Kim†, Gerbrand Ceder, et al. "Promises and challenges of next-generation "beyond Li-ion" batteries for electric vehicles and grid decarbonization." in preparation. († equal contribution)

2.1. Introduction

The main research focus in all-solid-state batteries has been on finding fast ionic conductors, which has resulted in many newly discovered conductors with ionic conductivities close to or even surpassing those of liquid electrolytes. Given that the basic structural and chemical features for high alkali ion conductivity are now reasonably well understood (*48*, *71*), it is likely even better conductors will be developed. In Li-ion systems, some NASICON-, perovskite- and garnet-type oxides exhibit room-

temperature (RT) conductivities of approximately 1 mS cm^{-1} or higher but suffer from poor contact with electrodes because of difficulties in pellet pressing and sintering (*24*, *72–76*). Sulfide-based solid electrolytes such as $Li_{10}GeP_2S_{12}$ (LGPS) and Li_2S-P_2S_5 (LPS) exhibit conductivities greater than 10 mS cm^{-1} (*19*, *43*, *59*, *71*, *77*, *78*), but generally have limited voltage stability windows, which makes electrode selection a difficult task (*14*, *79–81*). In some cases, an electrode coating is applied to mitigate this issue; however, the coating process is often imperfect, which leads to very different effectiveness of interface protection using different coating materials and/or methods (*77*, *82–84*). In parallel to the developments in solid-state lithium conductors, promising fast Na-ion conductors have also been recently discovered and applied in Na-ion batteries (NIBs) (*47*, *85*, *86*). However, it is similarly challenging to find a Na conductor with all the desired properties for all-solid-state battery applications, namely high conductivity, compatibility with both anodes and cathodes, processability, and good mechanical properties.

The bottleneck of all-solid-state battery development has shifted toward the integration of the solid electrolyte and electrodes. This challenge of cell integration is largely associated with maintaining chemical and mechanical stability between the electrodes and electrolytes during battery operation, both of which are a major obstacle for solid-state battery development. The compatibility of electrodes and electrolytes is largely determined by the properties of the electrode/electrolyte interface. A good interface between a solid electrolyte and electrode requires fast ion transport, maximum contact area, and chemical stability during cycling. Indeed, in detailed studies, previously claimed stable electrolyte/electrode pairs have often found to degrade through chemical or electrochemical reactions (*71*, *76*, *77*, *87–90*).

In this chapter, we focus on the chemical aspect of the cell integration challenge, and present a methodology that combines computational predictions with fast, simple experimental tests that can efficiently screen the compatibility of numerous electrode/electrolyte pairs. We use layered Na transition metal oxide cathodes ($NaMO_2$, M = Cr, Mn, Fe, Co, Ni) and two recently reported solid electrolytes with high ionic conductivities (Na_3PS_4 (*43*, *91*) and Na_3PSe_4 (*58*, *88*, *89*)) as examples to demonstrate our methodology. The Na ion system was selected for several reasons. First, NIBs have attracted significant attention because of the lower cost and greater abundance of their materials compared with those used in LIBs (*58*, *92*, *93*). Second, the Na system provides a wider chemical space to explore for cathode materials, enabling synthesis and cycling of many electrode materials for which the Li analogues are electrochemically inactive (*58*, *93*, *94*). Finally, compatibility issues have not been systematically studied in the Na solid-state system, which provides us with an opportunity to demonstrate the efficiency of our screening method when applied to unknown systems.

2.2. Methodology

There are two relevant interfaces existing in a cathode composite:

1) interface between the solid electrolyte and electron sources (e.g., current collector, conductive carbon additive, electron conductive cathode particles);

2) interface between the electrolyte and the active cathode.

The methodology to evaluate the interfacial stability are described separately in this section.

2.2.1. Voltage window of the solid electrolyte

The voltage window of the electrolyte determines the cycling range and selection of both electrodes and should thus be considered and determined first. Prior experimental insights regarding the electrochemical stability of solid-state electrolytes require reinterpretation. Determination of the stable electrochemical window of a solid electrolyte has been traditionally performed using conventional cyclic voltammetry (CV) (*29*, *43*, *95*, *96*). In this method, the solid electrolyte is pressed into pellets and cycled with Li or Na metal on one side and an inert metal (such as stainless steel, Au, or Pt) on the other side. However, such CV measurements often overestimate the electrochemical stability limits of electrolytes. The bulk electrolyte is likely not in equilibrium during a CV scan because of the fast scanning rate and/or imperfect contact with the metal electrodes. Furthermore, because of the poor electronic conductivity of solid electrolytes, the overall decomposition reaction is often slow or limited to a thin region at the interface, thereby limiting the degradation current that can be observed in a CV scan. The situation is very different in a real cell configuration, where the electrolyte is mixed with carbon and the cathode material, providing a facile electron transfer pathway that promotes electrolyte redox reactions. Finally, the relatively small decomposition current detected by the CV method (sometimes less than 1 μA) is difficult to notice compared with the large current created by metal deposition/stripping at low voltage and is often ignored in the CV method. However, this small current could have a catastrophic effect on the long-term cycling of the full cell. Indeed, solid electrolytes previously claimed to be stable based on CV scans (*93*) were later upon more detailed investigation, found to be reactive at typical anode and cathode voltages (*97*), in agreement with theoretical predictions (*79*, *98*, *99*). Other electrochemical techniques, such as polarization experiments, should be complemented with CV methods to determine the stability window of the solid electrolyte more accurately. In such experiment, the electrolyte is made into electrode and polarized to a given potential or with a constant current. The electrolyte is considered stable at such potential if the capacity delivered below (or

above) this potential is close to zero during a galvanostatic or potentiostatic charge (or discharge).

In this chapter, the stability windows of selected electrolytes (Na_3PS_4 and Na_3PSe_4) were first computed using density functional theory (DFT) calculations. Details of the computation method is described in **Appendix C**. The results were then compared with experimental results obtained from galvanostatic charging/discharging. The synthesized solid electrolytes were ground into fine powders and then mixed with carbon and polymer binders to form film-type working electrodes, which were assembled in Swagelok cells with a liquid electrolyte against Na metal. By slowly cycling this cell, the voltage experienced by the electrolyte materials to be tested is much better represented by the cell voltage, and a more accurate estimation of the stability window of the materials can be provided. The corresponding charge (or discharge) capacities also indicate whether the electrolyte decomposition is self-limiting. A self-limiting decomposition reaction can be beneficial in widening the electrochemical stability of the electrolyte depending on the physical properties (e.g., ionic and electronic conductivities) of the decomposition products. The experiment methods about material synthesis, electrochemical measurement and characterization are described in detail in **Appendix B**.

2.2.2. Possible reaction between cathode and solid electrolyte

Absolute stability between the cathode and electrolyte is difficult to achieve, and the products of the reaction between the cathode and solid electrolyte can form an interfacial layer between the two. Depending on its properties, this interfacial layer can be detrimental or beneficial to the ionic transport between the two components. A good interface between the electrode and electrolyte must be self-passivating while still being permeable to the working ions. Based on this information, we tested the compatibility of electrodes and electrolytes by mixing the electrolyte and electrode powders at room temperature. Any bulk change detectable by X-ray diffraction (XRD) indicates that the selected electrolyte and electrode materials are incompatible. The possible reactions between electrodes and electrolytes at elevated temperatures were also evaluated using simultaneous differential scanning calorimetry and thermal gravimetric analysis (SDT) and XRD to determine the onset temperature of reaction and corresponding reaction products. Comparison of these results with the DFT-computed thermodynamic reaction products enabled us to assess the role of kinetics in the electrode/electrolyte reactions, providing additional mechanistic insights. Besides testing the reaction of the electrolyte with the as-synthesized cathode, compatibility with the charged cathode at high voltages is also important. At higher potential the strong oxidative power of the charged cathode will likely promote the electrolyte decomposition for chalcogenide systems. This

chemical compatibility, however, has not yet been systematically investigated. To investigate the aforementioned issue, partially charged cathodes were prepared through chemical oxidation with highly concentrated iodine in acetonitrile (CH_3CN), resulting in cathode powders equivalent to being charged to approximately 3.7 V against Na metal (*100*, *101*). The reactions between the charged cathodes and electrolytes were then studied in a similar manner as discussed above.

2.3. Electrochemical stability of solid electrolyte

The calculated voltage stability window and decomposition products of Na_3PS_4 and Na_3PSe_4 are shown in **Figure 2-1** and **2-2**, respectively[3]. These figures indicate which products the conductor converts into when Na is supplied and extracted at a given potential. The *x*-axis represents the capacity generated when these decomposition reactions occur per gram of conductor consumed. The results in **Figure 2-1** indicate that Na_3PS_4 is electrochemically only stable from 1.55 to 2.25 V against Na metal. Below 1.55 V, Na_3PS_4 can be reduced and converted into Na_2S and other Na-P compounds. Above 2.25 V, in contrast, Na is extracted from Na_3PS_4, leading to decomposition into Na-deficient phases such as P_2S_7 and S. Similarly, according to **Figure 2-2**, Na_3PSe_4 is stable from 1.80 to 2.15 V against Na metal and decomposes into Na_2Se and other Na-P compounds below 1.80 V and Na-deficient phases such as PSe and Se above 2.15 V. Of note is that our calculated stability window is much narrower than experimental values claimed from CV measurements, but in agreement with other theory work (*59*, *102*). This discrepancy results either from reaction kinetics, which would delay the onset of decomposition, or intrinsic limitations of the CV measurements. Based on our experimental results, as will be discussed below, the latter is more likely.

These calculated voltages assume that diffusion kinetics are not limiting, and thus provide a lower bound of the Na extraction voltage. To investigate the upper limiting case, the voltage for topotactic desodiation of the conductors was calculated. The calculated results indicate that Na_3PS_4 and Na_3PSe_4 lose Na at 3.05 V and 2.75 V, respectively. We found furthermore that the voltage for subsequent extraction of Na is lower. Note that these two values indeed provide absolute upper bound for the Na_3PX_4 stability window, as the Na-ion and electron extraction are unlikely to be kinetically limited due to the faster Na-ion mobility in these materials.

[3] DFT calculations were performed with collaborator Dr. William Richards (MIT, Ceder Group 2017 Graduate).

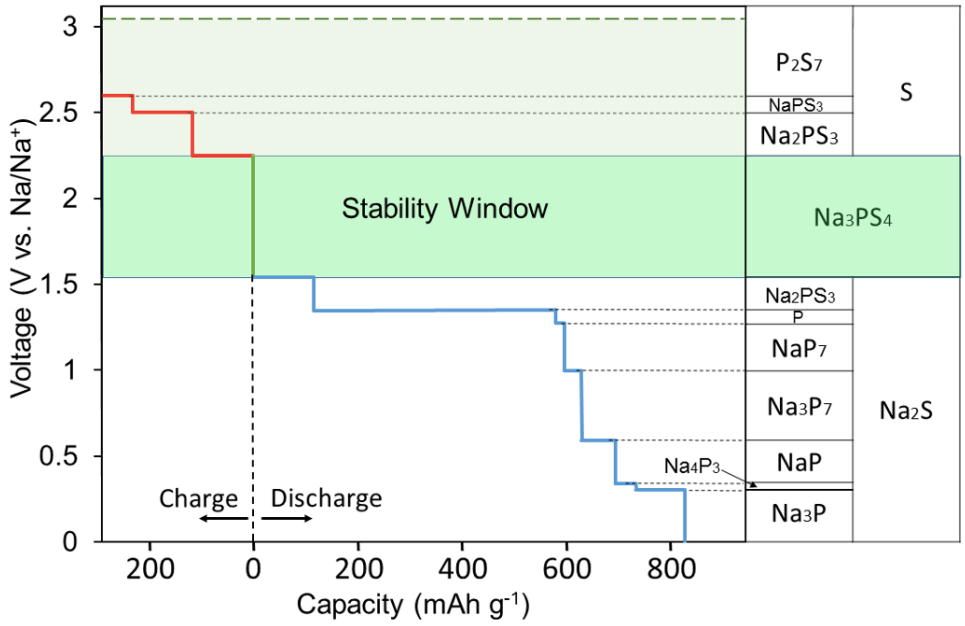


Figure 2-1 Calculated stability window and decomposition products for Na_3PS_4.

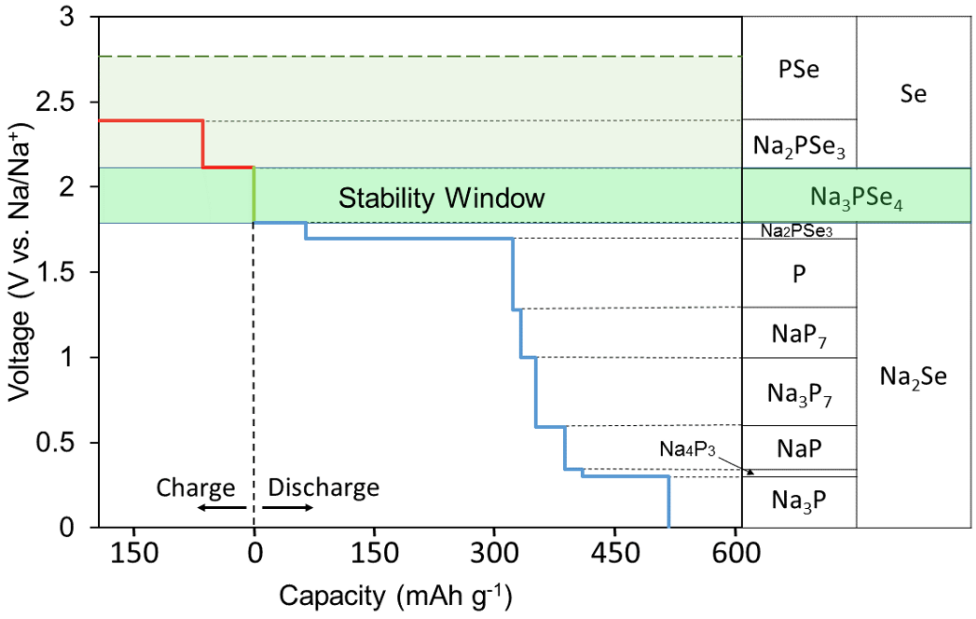


Figure 2-2 Calculated stability window and decomposition products for Na_3PSe_4.

To experimentally determine the electrochemical stability window of the electrolyte materials, Na_3PX_4 (X = S, Se) cathodes were "charged" (oxidized) or "discharged" (reduced) at constant current between 0.5 V to 4.0 V. Upon charging, Na_3PS_4 exhibited

negligible capacity at the beginning of charging (**Figure 2-3a**). However, as the voltage increased above ~2.65 V, a voltage dip followed by a substantial capacity delivered at approximately 2.7 V was observed. The initial voltage rise is likely due to a nucleation or other activation process, needed to generate the decomposition products of Na_3PS_4. Therefore, we can assume that the voltage dip at approximately 2.5 V is the onset decomposition voltage of Na_3PS_4. Approximately 2.5 Na per formula unit (f.u.) can be extracted from Na_3PS_4 until the cut-off voltage of 4.0 V is reached. The "fully charged" Na_3PS_4 cathode composite turns completely amorphous as observed in XRD (**Figure 2-4a**).

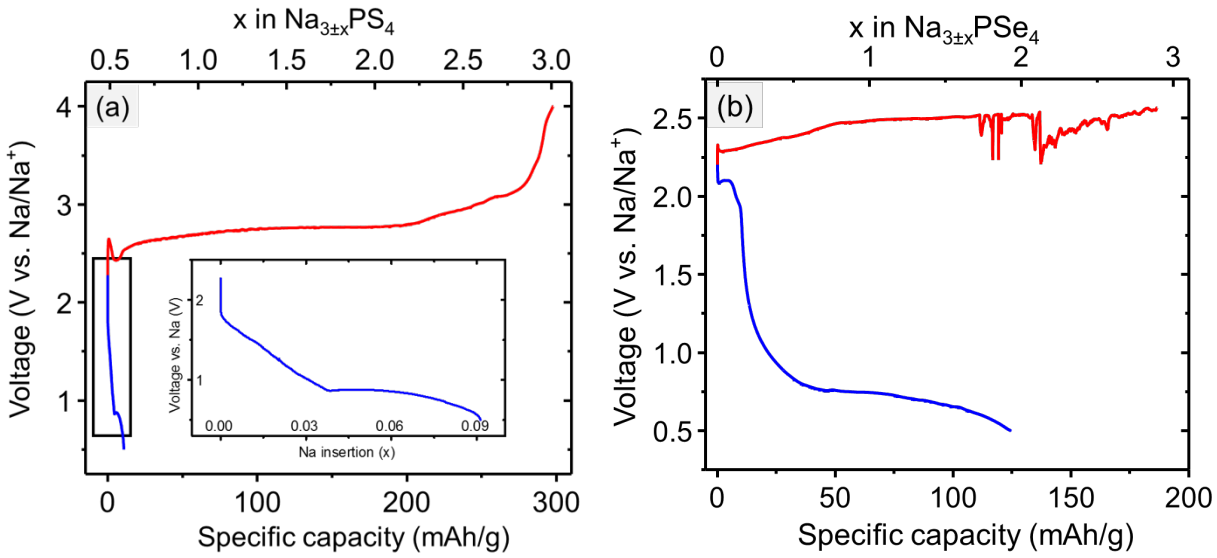


Figure 2-3 Electrochemical cycling of the Na_3PX_4 (mixed with carbon) cathode composite at constant current, showing the stability window of (a) Na_3PS_4 and (b) Na_3PSe_4.

During the discharging process, a sloping voltage region is first observed at approximately 1.8 V, followed by a redox reaction at approximately 0.9 V, suggesting that Na_3PS_4 is likely electrochemically unstable below this voltage. The sloping voltage region (1.8-0.9 V) is likely a result of the presence of a small amount of sulfur in the as-prepared Na_3PS_4 sample. The reduction of sulfur occurs at approximately 2 V. Interestingly, fully discharging to the cut-off voltage of 0.5 V only results in a very low capacity (i.e., 0.08 Na intercalation per formula), and the "fully discharged" Na_3PS_4 shows almost no structural change compared with the pristine cathode composite (**Figure 2-4a**). One possible reason is that Na_3PS_4 might be passivated by the decomposition products upon discharging. This passivating process may prevent further decomposition

of Na_3PS_4 and widens the apparent reduction limit of Na_3PS_4. Based on the discussion above, we conclude that the electrochemical stability window of Na_3PS_4 lies within the range 0.9-2.5 V, which is in much better agreement with the DFT predictions than reported CV measurements, further underscoring the limited reliability of CV techniques to determine the stability limits of solid electrolytes.

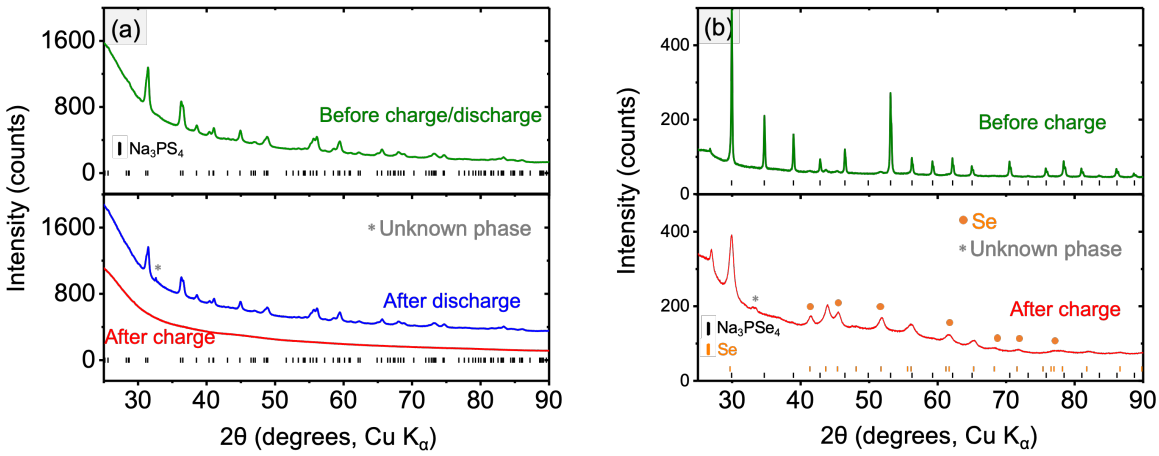


Figure 2-4 Diffraction patterns of the Na_3PX_4 cathode composite before and after being fully charged/discharged. (a) Na_3PS_4 and (b) Na_3PSe_4

Similarly, the stability window of Na_3PSe_4 was experimentally determined by charging and discharging the Na_3PSe_4 (mixed with carbon) cathode composite. During the charging process shown in **Figure 2-3b**, the decomposition of Na_3PSe_4 starts at approximately 2.33 V, where a substantial capacity of 110 mAh/g or 1.5 Na per formula was delivered in the sloping voltage region of 2.33-2.50 V. Based on DFT calculations, this decomposition process is most likely associated with the production of Se and Na_2PSe_3. The decomposition products of the "fully charged" Na_3PSe_4 was experimentally determined by XRD presented in **Figure 2-4b**, in which new Se peaks are observed after the Na_3PSe_4 cathode composite is "fully charged", which is in almost perfect agreement with the DFT calculations. The prolonged voltage plateau at approximately 2.50 V might be a result of the redox shuttle effect caused by dissolved poly-selenide molecules (*103*, *104*), and the voltage fluctuation could be related to the reaction of the Na metal with the dissolved decomposition products. When the cell was opened after the charging process, the separators and Na metal had both become brown, indirectly supporting the above explanation of the voltage fluctuation. During the discharge process, a noticeable redox reaction occurs at approximately 2.10 V. Similarly, this is likely due to the presence of a small amount of the selenium in the as-prepared Na_3PSe_4 sample, which is reduced

at approximately 2 V (*103*). Since only a small capacity is delivered in the voltage sloping region (2.10-1.25 V), it is unlikely to arise from the bulk reduction of Na_3PSe_4. Thus we tentatively assigned 1.25 V as the cathodic stability limit of Na_3PSe_4. Based on DFT calculations, this process is associated with the production of Na_2Se and Na_2PSe_3. Overall, the stability window of Na_3PSe_4 was determined to be 1.25-2.35 V, which is again closer to our theoretical predictions than to the CV measurement. The various stability windows obtained theoretically and experimentally for Na_3PX_4 are summarized in **Table 2-1**.

Table 2-1 Comparisons of the various stability windows obtained theoretically and experimentally for Na_3PX_4

	Thermodynamic window (V)	Kinetic upper limit (V)	Experimental (liquid cell charging) upper limit (V)	Experimental (CV measurement) upper limit (V)
Na_3PS_4	1.55 - 2.25	3.05	2.50	> 5 V (*102*)
Na_3PSe_4	1.80 - 2.15	2.75	2.33	2.6 V (*104*)

2.4. Compatibility between cathode and solid electrolyte

2.4.1. *DFT-predicted products of cathode/electrolyte reactions*

To obtain an estimate of the chemical stability of each interface, we used DFT calculations to calculate the maximum mixing energy of the cathode/electrolyte compositions using the methods described in **Appendix C**. The maximum mixing energies and their corresponding reaction products were calculated for all combinations of the cathodes ($NaMO_2$, M = Cr, Mn, Fe, Co, Ni) and electrolytes (Na_3PX_4, X = S, Se)[4]. To show the compatibility at different status of charge, this procedure was repeated for partially desodiated cathodes $Na_{0.5}MO_2$. The calculation results, summarized in **Table 2-2**, indicate that none of the oxide and chalcogenide pairs are chemically absolutely stable. Because there are many possible reactions that result in similar mixing energies, and because which one actually forms depends on both thermodynamic and kinetic factors, a full list of the reaction products along the entire tie line is summarized **Table D-1** in **Appendix D**. Because these reactions require significant bulk diffusion, they can be expected to localize to a small interfacial region unless aided by high temperatures.

[4] DFT calculations were performed with collaborator Dr. William Richards (MIT, Ceder Group 2017 Graduate).

Table 2-2 DFT calculations for the products of the reaction between Na_xMO_2 (x = 0.5 or 1.0) and Na_3PX_4.[5]

		$NaCrO_2$	**$NaMnO_2$**	**$NaFeO_2$**	**$NaCoO_2$**	**$NaNiO_2$**
Na_3PS_4	Reaction products	Na_3PO_4 $NaCrS_2$	Na_3PO_4 $NaMnS_2^*$	Na_3PO_4 $Na_{3/2}(FeS_2)$ FeS_2	Na_3PO_4 $NaCoS_2$	Na_3PO_4 Na_2S Na_2SO_4 $Na_2Ni_3S_4^*$
	Reaction energy (eV/atom)	-0.0970	-0.2649	-0.2652	-0.3516	-0.4394
Na_3PSe_4	Reaction products	Na_3PO_4 $NaCrSe_2$	Na_3PO_4 $NaMnSe_2^*$	Na_3PO_4 Na_2Se $FeSe_2$ $FeSe$	Na_3PO_4 Na_2Se Co_9Se_8 $Co_5Se_8^*$	Na_3PO_4 Na_2Se $Ni_5Se_8^*$ Ni_3Se_4
	Reaction energy (eV/atom)	-0.1325	-0.2138	-0.2615	-0.3695	-0.4541
		$Na_{0.5}CrO_2$	$Na_{0.5}MnO_2$	$Na_{0.5}FeO_2$	$Na_{0.5}CoO_2$	$Na_{0.5}NiO_2$
Na_3PS_4	Reaction products	Na_3PO_4 $NaCrS_2$ S Cr_2O_3	Na_3PO_4 Na_2SO_4 MnS $Na_4Mn_3S_5^*$	Na_3PO_4 $Na_{3/2}(FeS_2)$ FeS_2	Na_3PO_4 Na_2S Na_2SO_4 Co_9S_8	Na_3PO_4 Na_2SO_4 Ni_9S_8 Ni_3S_2
	Reaction energy (eV/atom)	-0.1429	-0.3156	-0.3514	-0.4376	-0.5580
Na_3PSe_4	Reaction products	Na_3PO_4 $Na_{1/3}(CrSe_2)$ $Na_{2/3}(CrSe_2)$	Na_3PO_4 $Na_{1/3}(MnSe_2)$ Na_6MnSe_4 MnO	Na_3PO_4 Na_2Se $FeSe_2$ $FeSe$	Na_3PO_4 Na_2Se $Co_5Se_8^*$ $CoSe_2$	Na_3PO_4 Na_2Se $Ni_5Se_8^*$ $NiSe_2$
	Reaction energy (eV/atom)	-0.1985	-0.2848	-0.3730	-0.4558	-0.5463

The reactions between the Na_xMO_2 (x = 1.0 pristine or x = 0.5 desodiated) cathode and Na_3PX_4 electrolyte can be broadly categorized into two classes (often occurring together):

1) Anion exchange reactions. For instance, mixing $NaCrO_2$ and Na_3PX_4 (X = S, Se) can produce $NaCrX_2$ (X = S, Se) and Na_3PO_4. The exchange of some oxygen from the cathode

[5] * denotes compounds which are created through chemical substitution of compounds which are present in the Inorganic Crystal Structure Database (ICSD).

with the chalcogenide from the electrolyte to form Na_3PO_4 and metal-chalcogenides is favorable for all the systems we investigated.

2) Complex redox reactions involving multiple phases with significant structural rearrangements. For example, mixing $NaNiO_2$ and Na_3PX_4 (X = S, Se) leads to the production of more than three decomposition products and involves transition metal reduction.

2.4.2. *Experimental verification of the reactions between the pristine cathode and electrolyte*

The compatibility of the pristine cathode and electrolyte was first investigated at room temperature. Diffraction patterns before and after mixing the selected electrode and electrolyte materials at room temperature are shown in **Figure E-1 in Appendix E**. **Figure E-1 (a-d)** shows that the diffraction patterns of $NaCrO_2$ and $NaMnO_2$ mixed with Na_3PS_4 or Na_3PSe_4 are almost the same as the sum the patterns of the individual components, suggesting that no bulk reaction occurs in these paired materials after mixing at room temperature. In contrast, peak shifts and/or peak shape changes are observed after mixing $NaFeO_2$, $NaCoO_2$, or $NaNiO_2$ with Na_3PSe_4 (**Figure E-1 e-j**)[6], indicating a change in lattice dimension and/or symmetry. The majority of peaks that show noticeable differences are associated with Na_3PSe_4, which we believe is caused by either an anion exchange process creating intermediate $Na_3PO_xSe_{4-x}$ phases or topotactic Na extraction from Na_3PSe_4 accompanied by Se^{2-} oxidation. Through this simple test, our experiments already indicate that $NaFeO_2$, $NaCoO_2$, and $NaNiO_2$ cathodes are likely incompatible with Na_3PSe_4. The compatibility between the selected cathode and electrolyte materials at elevated temperatures were tested by SDT, and the onset temperatures of the reactions of the cathode/electrolyte pairs are summarized in **Table 2-3**. It is noted that the SDT results show that $NaCoO_2$ and $NaNiO_2$ are not compatible with Na_3PS_4 at very low temperatures, close to RT (47°C and 30°C, respectively), even though no peak change in XRD can be observed after mixing them at RT (**Figure E-1 f and h**). Unless other strategies such as protective barrier coatings are utilized to improve the compatibility of these electrodes (i.e. $NaFeO_2$, $NaCoO_2$, or $NaNiO_2$) with Na_3PX_4 electrolytes, alternative pairs should be sought.

[6] The compatibility measurements between $NaFeO_2$, $NaCoO_2$, or $NaNiO_2$ with Na_3PX_4 were performed by collaborator Mr. Tan Shi (UC Berkeley, Ceder Group Graduate Student).

Table 2-3 Onset temperatures of the reactions between NaMO$_2$ and Na$_3$PX_4 [7]

	$NaCrO_2$	$NaMnO_2$	$NaFeO_2$	$NaCoO_2$	$NaNiO_2$
Na_3PS_4	500°C	330°C	270°C	47°C	30°C
Na_3PSe_4	380°C	220°C	25°C*	25°C*	25°C*

According to the onset temperature of each reaction between NaMO$_2$ and Na$_3$PX_4 listed in **Table 2-3**, two reaction trends are observed:

1) From $NaCrO_2$ to $NaNiO_2$, the onset temperature decreases, indicating a reduction of the kinetic barrier, which may be related to an increase of the driving force of each reaction (**Table 2-2**).

2) From Na_3PS_4 to Na_3PSe_4, the onset temperature also decreases.

The cathode-electrolyte pairs for which no bulk reactions were observed close to RT (i.e., $NaCrO_2$ and $NaMnO_2$ with Na$_3$PX_4) were subjected to combined SDT and XRD characterization. These simple tests were quite informative, as they provided insight into the intriguing interplay between thermodynamics and kinetics in the decomposition reactions. Taking $NaCrO_2$ and Na$_3$PX_4 as an example, when these mixtures were heated to below approximately 300°C, no bulk reaction was observed in the XRD results (**Figure 2-5**). This finding suggests that $NaCrO_2$ and Na_3PX_4 should be a relatively stable pair that could be used in solid-state batteries at RT. When the reaction temperature was raised to 500°C, $NaCrSe_2$ (along with excess $NaCrO_2$) was observed in the final products of the reaction between $NaCrO_2$ and Na_3PSe_4 (green line in **Figure 2-5b**), which partially agrees with the DFT calculation result in **Table 2-2**. No other P-containing phases were observed in the XRD result. Because no substantial mass loss (<0.6%) was observed upon heating to 500°C (**Figure 2-6b**), P-containing phases should still be present in the mixture but in amorphous form. Taken together with the DFT prediction (**Table 2-2**), we suspect that amorphous Na_3PO_4 is present in the heated mixture. However, when the conductor was changed to Na_3PS_4, the calculated reaction products between $NaCrO_2$ and Na_3PS_4 with the highest driving force (i.e. $NaCrS_2$ and Na_3PO_4) were not observed after heating to 500°C. Instead, Na_3PS_3O (together with both precursors $NaCrO_2$ and Na_3PS_4) was observed (green line in **Figure 2-5a**). It is not until 700°C that the predicted product $NaCrS_2$ (together with excess $NaCrO_2$) starts to appear with the disappearance of Na_3PS_3O (orange line in **Figure 2-5a**). Although the predicted $NaCrS_2$ might be

[7] * indicates when a bulk change was observed after mixing paired materials at RT, we tentatively assigned 25°C as the onset temperature of the reaction.

present in the heated mixture in amorphous form, the presence of Na_3PS_3O in lieu of the predicted product Na_3PO_4 may indicate a preference for intermediate reaction products over the stable thermodynamic states unless the temperature is very high. We also note from **Table 2-2** that the reaction energy between $NaCrO_2$ and the selenide conductor is substantially higher than with the sulfide conductor.

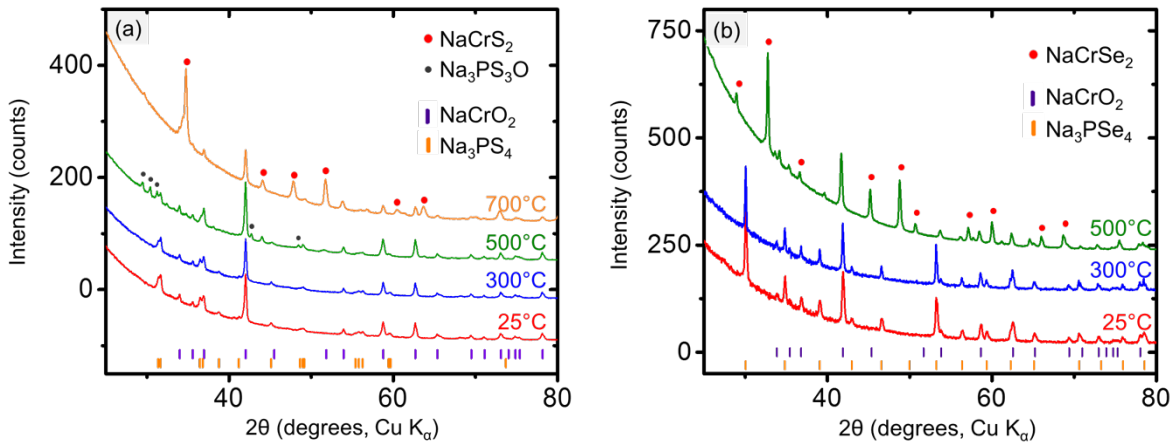


Figure 2-5 XRD patterns of the reaction products of (a) $NaCrO_2$ and Na_3PS_4 at RT, 300°C, 500°C, and 700°C, and (b) $NaCrO_2$ and Na_3PSe_4 at RT (25°C), 300°C, and 500°C. The tick marks indicate the peaks for the reactants $NaCrO_2$ and Na_3PX_4.

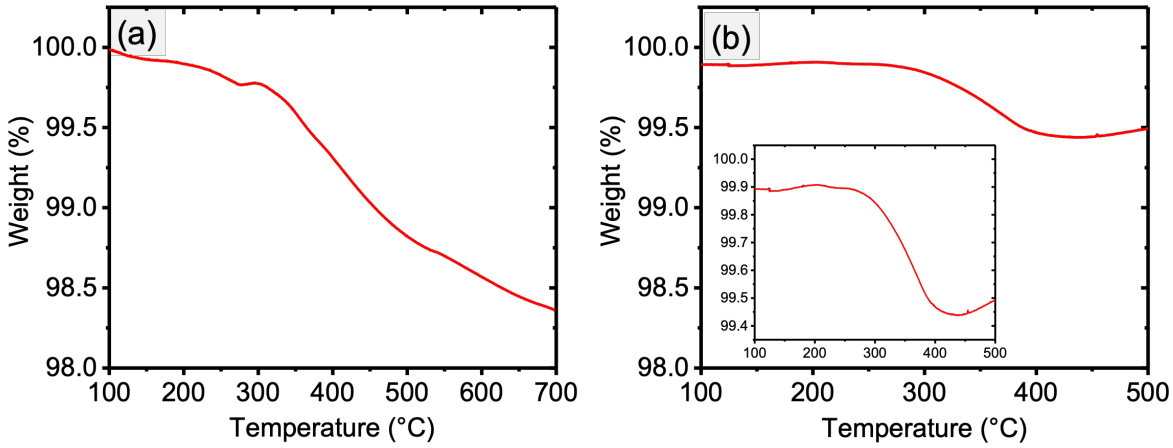


Figure 2-6 TGA measurements (total weight) of the reactions between (a) $NaCrO_2$ and Na_3PS_4 and (b) $NaCrO_2$ and Na_3PSe_4.The weight axis is shown in the same scale to emphasize the higher reactivity of S-based compound.

2.4.3. *Chemical reactions between desodiated cathode and electrolyte*

The compatibility between the partially desodiated cathode Na_xMO_2 ($x < 1.0$) and electrolyte Na_3PX_4 is equally important for the stable cycling of all-solid-state batteries and was also investigated. We first prepared the chemically desodiated $NaCrO_2$, $NaCoO_2$, $NaFeO_2$, and $NaNiO_2$ samples using a highly-concentrated iodine solution in acetonitrile, which is equivalent to oxidation at ~3.7 V (*105*). The same process always yields amorphous desodiated $NaMnO_2$, likely due to Mn dissolution into the acetonitrile solvent (*106*). Desodiated $NaMnO_2$ was therefore excluded in our study. The diffraction patterns for desodiated $NaCrO_2$, $NaCoO_2$, $NaFeO_2$, and $NaNiO_2$ are presented in **Figure 2-7**. The products after chemical desodiation were $Na_{0.5}CrO_2$, $Na_{0.5}FeO_2$ + β-$NaFeO_2$, $Na_{0.5}CoO_2$, and $Na_{0.5}NiO_2$ + $Na_{0.4}NiO_2$, respectively. The Na compositions of Na_xMO_2 compounds were estimated based on comparisons of the refined lattice parameters and electrochemical capacity with previous literature.

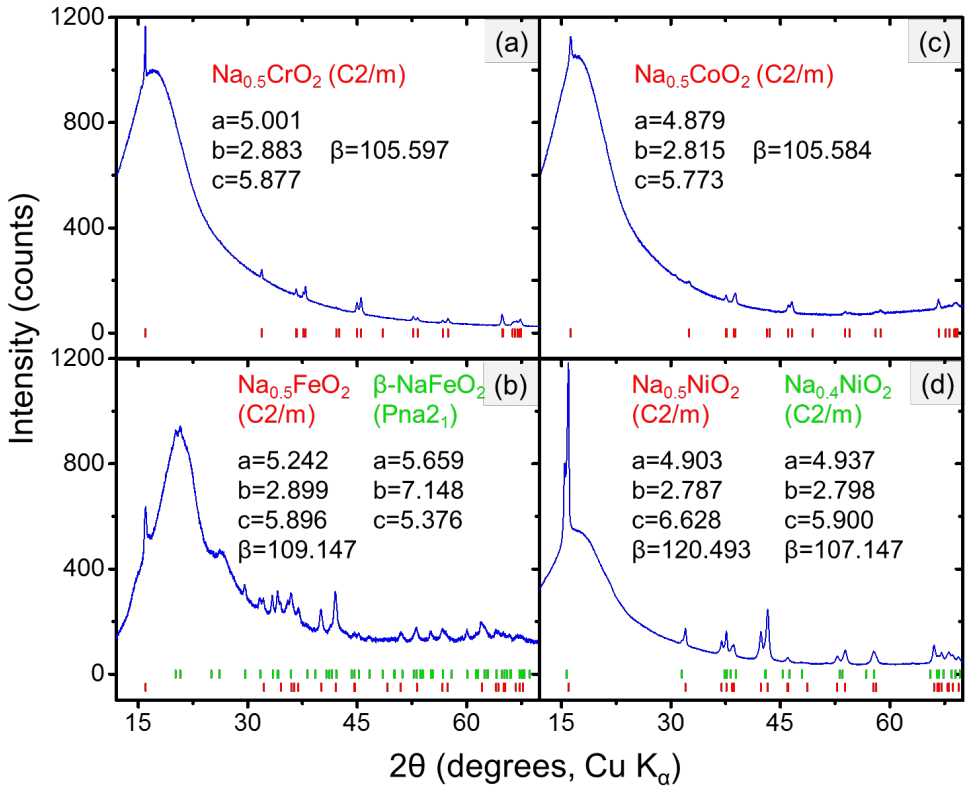


Figure 2-7 Diffraction patterns of desodiated compound(s) of (a) $NaCrO_2$, (b) $NaFeO_2$, (c) $NaCoO_2$, and (d) $NaNiO_2$. The peak positions and refined structure data are also displayed.[8]

[8] The bump at ~15° in all four figures originates from the Kapton sample holder.

When the partially desodiated samples were mixed with Na_3PX_4, only $Na_{0.5}CrO_2$ was observed to be compatible with Na_3PX_4 at RT (i.e., no bulk reaction was observed in the XRD results, see **Figure 2-8**). All of the other partially desodiated samples reacted with the electrolyte, and some of the reactions were rather violent. For example, when partially desodiated $NaNiO_2$ was mixed with Na_3PX_4 in an Ar glove box, sparks were immediately generated and the powder color changed to dark red.

Because $Na_{0.5}CrO_2$ is the only compound compatible with Na_3PX_4 at RT among our observations, further studies with XRD and SDT at elevated temperatures were performed. In the XRD of mixed $Na_{0.5}CrO_2$ and Na_3PX_4, we observed that fully sodiated $NaCrO_2$ was regenerated after heating the mixture to 300°C in reactions with both Na_3PSe_4 (**Figure 2-8a**) and Na_3PS_4 (**Figure 2-8b**), suggesting that Na is extracted from the Na_3PX_4 electrolyte and inserted into $Na_{0.5}CrO_2$, consistent with the thermodynamic anodic potentials predicted for the Na_3PX_4 electrolytes (2.25 V for Na_3PS_4 and 2.15 V for Na_3PSe_4), which are well below the $Na_{0.5}CrO_2$ voltage (~3.7 V vs. Na/Na^+).

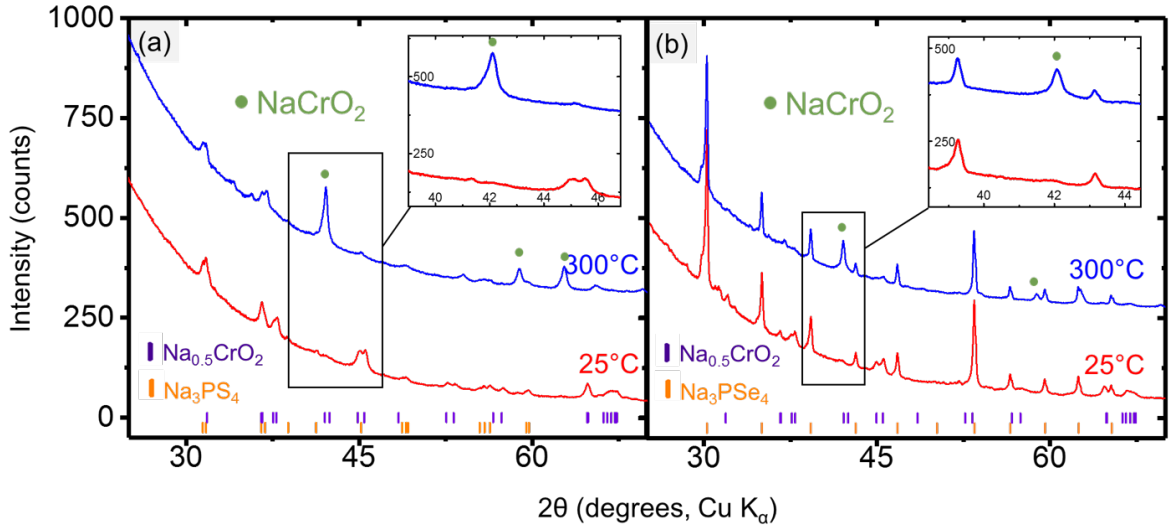


Figure 2-8 XRD results for reaction between (a) $Na_{0.5}CrO_2$ and Na_3PS_4 and (b) $Na_{0.5}CrO_2$ and Na_3PSe_4 at RT (25°C) and 300°C.

This Na insertion to $Na_{0.5}CrO_2$ is similar to a self-discharge reaction, as often observed in rechargeable batteries, leading to decomposition of the electrolyte (i.e. Na_3PX_4). As shown in **Figure 2-1** and **Figure 2-2**, S or Se is likely generated in the decomposition products by oxidizing Na_3PX_4. In the reaction between $Na_{0.5}CrO_2$ and Na_3PSe_4, the generation of Se can indeed be observed in our differential scanning calorimetry (DSC)

measurements (**Figure 2-9a**), where an endothermal peak is observed at approximately 220°C, corresponding to the melting point of Se (220.8°C). The following exothermal peak is attributed to the heat generation of the bulk reaction. In contrast, the generation of S cannot be observed in the reaction between $Na_{0.5}CrO_2$ and Na_3PS_4. In the DSC result for the reaction between $Na_{0.5}CrO_2$ and Na_3PS_4 in **Figure 2-9b**, only one exothermal peak is observed at approximately 260°C reflecting the heat generation of the reaction.

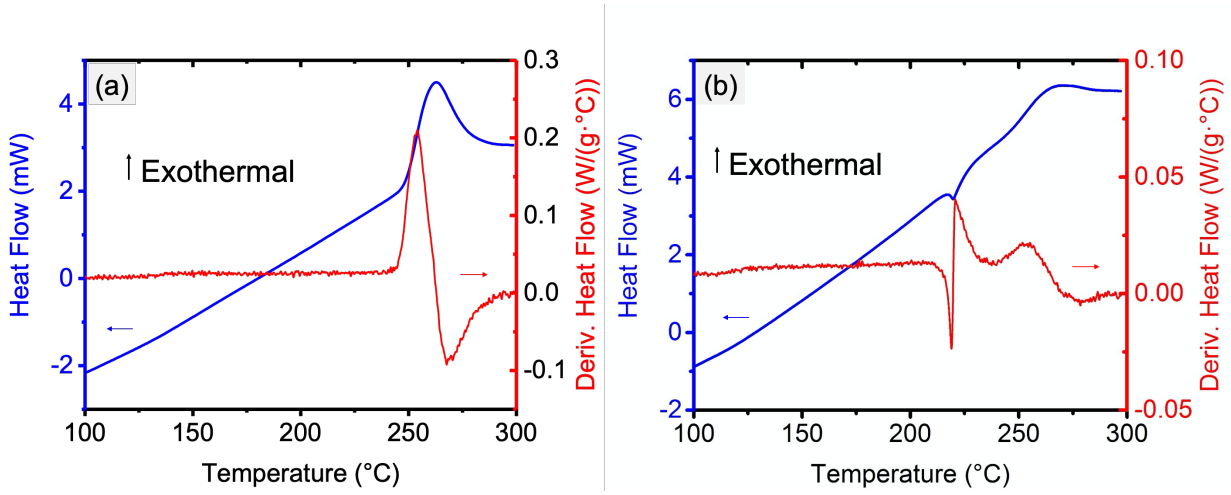


Figure 2-9 DSC results for reaction between (a) $Na_{0.5}CrO_2$ and Na_3PS_4 and (b) $Na_{0.5}CrO_2$ and Na_3PSe_4.

The surface reaction at RT between $Na_{0.5}CrO_2$ and Na_3PX_4 was investigated by X-ray photoelectron spectroscopy (XPS)[9]. After mixing $Na_{0.5}CrO_2$ and Na_3PX_4 at RT, XPS measurements were performed on the Cr 2p peaks of the mixture. The Cr 2p reference peak positions in Cr^{3+} and Cr^{4+} were obtained by fitting the Cr $2p_{1/2}$ and $2p_{3/2}$ peaks in $NaCrO_2$ (Cr^{3+} only) and $Na_{0.5}CrO_2$ (Cr^{3+}: Cr^{4+} = 1:1), respectively (**Figure 2-10**). The XPS spectrum of the Cr 2p peaks in the mixture of $Na_{0.5}CrO_2$ and Na_3PSe_4 is presented in Figure 7b, and the fitting result indicates that the Cr^{3+}/Cr^{4+} ratio changed from approximately 1.0 in $Na_{0.5}CrO_2$ to 2.423 in the mixed material (**Table 2-4**). The reduction of Cr^{4+} indicates an insertion of Na to $Na_{0.5}CrO_2$. This surface reaction between $Na_{0.5}CrO_2$ and Na_3PSe_4 at RT cannot be detected in XRD (**Figure 2-8a**), reflecting a slow kinetics and/or a self-passivation reaction mechanism. It is likely that the reaction products form a passivation layer and prevent further reaction, which explains why no bulk reaction is observed at RT in XRD. Based on the above discussion, the surface reaction is likely associated with the production of Se. As the temperature increases to

[9] XPS measurements were performed by collaborator Mr. Tan Shi (UC Berkeley, Ceder Group Graduate Student).

the melting point of Se, the passivation layer becomes unstable and further reaction is activated, which is in good agreement with our observation in DSC (Figure 6c). When $Na_{0.5}CrO_2$ was mixed with Na_3PS_4, a lower Cr^{3+}/Cr^{4+} ratio increase (i.e. less Cr^{4+} reduction) was observed (Table 3), indicating that less Na was extracted from Na_3PS_4 in the reaction between $Na_{0.5}CrO_2$ and Na_3PS_4. This observation is likely due to the slightly lower reactivity of Na_3PS_4, which is in line with the onset temperatures of the reaction between $NaMO_2$ and Na_3PX_4 (**Table 2-3**).

Table 2-4 XPS data fitting results for Cr 2p peaks

Sample	Component	Peak Position (eV)		Area (a.u.)		Cr^{3+}/Cr^{4+} Ratio
		$2p_{3/2}$	$2p_{1/2}$	$2p_{3/2}$	$2p_{1/2}$	
$Na_{0.5}CrO_2/Na_3PS_4$ RT Mixture	Cr^{3+}	577.03	586.52	299	149	1.869
	Cr^{4+}	579.09	588.52	160	80	
$Na_{0.5}CrO_2/Na_3PSe_4$ RT Mixture	Cr^{3+}	577.03	586.52	344	172	2.423
	Cr^{4+}	579.09	588.52	142	71	
$Na_{0.5}CrO_2$	Cr^{3+}	577.03	586.52	470	234	0.997
	Cr^{4+}	579.09	588.52	484	242	
$NaCrO_2$	Cr^{3+}	577.03	586.52	661	331	/

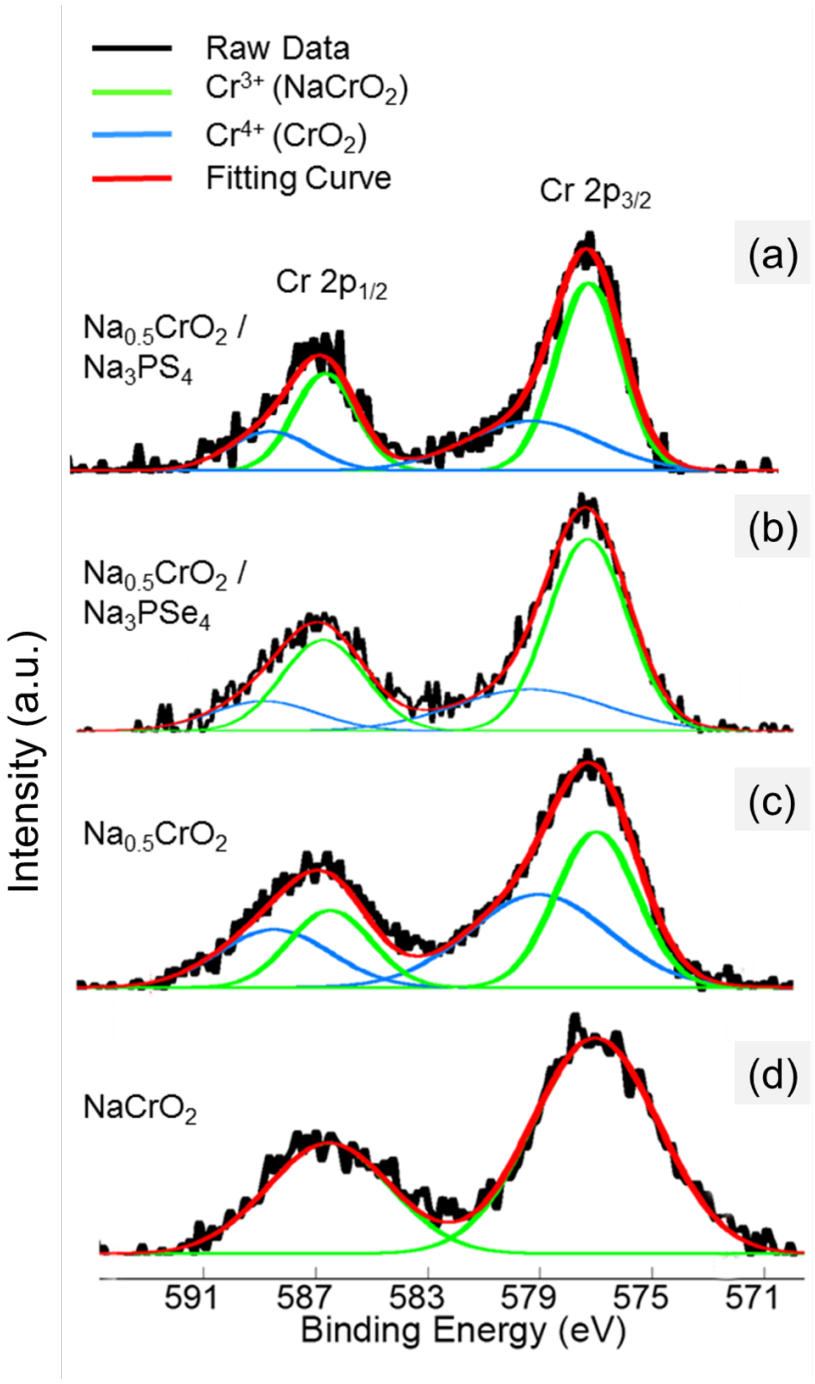


Figure 2-10 XPS spectra of Cr 2p from the surfaces of (a) mixture of $Na_{0.5}CrO_2$ and Na_3PS_4 at RT (25°C), (b) mixture of $Na_{0.5}CrO_2$ and Na_3PSe_4 at RT (25°C), (c) $Na_{0.5}CrO_2$, and (d) $NaCrO_2$.

2.5. Discussion and outlook

In this chapter, we distinguish the pure electrochemical stability of the solid-state electrolyte at various Na chemical potentials (and in contact with Na reservoir) from the chemically-enhanced instability when solid-state electrolyte and cathode chemically interact. The pure electrochemical stability is relevant wherever the solid electrolyte is in contact with the electron reservoir. Hence this occurs at the cathode/electrolyte interface, at a direct contact with the current collector, or through the carbon network present in the electrode. Since Na^+ is highly mobile in the solid-state electrolyte, the conductor experiences the full chemical potential of Na applied at these electron contact interfaces. Computationally, we calculate the stability of the conductor in this condition by evaluating the thermodynamic grand potential of the compound under various applied Na chemical potentials, as described in prior work (*106*). This analysis requires the availability of thermochemical information on a number of competing phases in the phase diagram of the conductor. Such information can for example be found in online resources such as the Materials Project (*107*). This thermodynamic analysis for the electrochemical stability of the conductor provides a "safe" voltage window, in which there is no driving force at all for decomposition of the conductor. Because the thermodynamic decomposition of the conductor may sometimes require complete bond breaking in the material to form multiple other phases, it may be kinetically inhibited at the operating temperature of the battery. Hence, we also provide a kinetic anodic stability limit by evaluating at which potential, Na^+ can simply be extracted topotactically from the conductor together with the oxidation of the anion (S^{2-} or Se^{2-} in our case). Because the material is by definition a fast Na-ion conductor, and anion oxidation is easy, one expects there to be no kinetic barrier for this process. Hence, this topotactic Na extraction voltage can be considered an absolute upper bound for the voltage at which the conductor can operate. To test these computed stability limits we evaluated the conductor as an electrode in an electrochemical cell using liquid electrolyte so that contact problems, often present in full solid state devices, will not mask instabilities. The computational and experimental results summarized in **Table 2-1** clearly indicate that the measured upper voltage limit lies between the thermodynamic upper voltage and the topotactic Na extraction limit, in agreement with our understanding. Table 4 also clearly shows that CV is a poor tool to measure electrochemical stability of solid-state conductors. The poor reliability of CV measurements has led for example to claims that some sulfide conductors have 5V or even 10V stability (*107*), which is counterintuitive, given that a sulfide ion can general be oxidized between 2-3V.

In contact with the cathode, the conductor (i.e., solid-state electrolyte) can also undergo chemical reactivity. To determine this reactivity, we used a combination of XRD, SDT and XPS to evaluate the reaction products in mixed cathode/electrolyte powders.

Through the study of more than 20 cathode/electrolyte reactions between layered Na transition metal oxides ($NaMO_2$, M=Cr, Mn, Fe, Co, Ni) and two solid electrolytes (Na_3PX_4, X=S, Se), we were able to determine trends and understand the mechanisms behind these reactions. We first determine the thermodynamic driving forces and end-products of the cathode/electrolyte reaction, and then discuss what may happen under more kinetically constrained conditions. There are some common trends that can be understood from **Table 2-2**:

(1) On the cathode/conductor interface P strongly prefers bonding to O, resulting in the exchange of O and S/Se between the cathode and conductor, and the formation of PO_4 groups. As a result, Na_3PO_4 is produced for all reactions listed in **Table 2-2**.

(2) Some transition metals, even in the discharged redox state can oxidize the chalcogenide anion leading to reaction products that are metallic, have per-sulfide or per-selenide ions, or even sulfate ions. This is the case for the $NaFeO_2$ and $NaNiO_2$ cathodes against both conductors and for the $NaCoO_2$ cathode against the selenide conductor. The fact that the $NaCoO_2$ seems redox stable with the sulfide but not with the selenide is likely due to the fact that the Se^{2-} ion is easier to oxidize than S^{2-}.

Once the cathodes are charged (bottom part of **Table 2-2**) oxidation of the anion by reduction of the transition metal is favorable for all cathode/conductor couples, and only local passivation with an electron-insulating layer will protect the conductor. The reaction products that form at the interface are however dependent chemistry of each cathode. In some cases, elemental S is predicted to occur (e.g. $Na_{0.5}CrO_2$ with Na_3PS_4) while for other cathode/conductor couples reduced metal sulfides are usually predicted (MnS, FeS_2, etc.). The reaction products for the Co and Ni cathode deserve particular attention. Compounds such as Ni_9S_8 and Co_9Se_8 are in the pentlandite family and have a structure containing an excess of metal atoms and short metal-metal distance (*108*). Similar metal-metal bonding also exists in other metal-rich chalcogenides such as Ni_3S_2 (*109*, *110*). These compounds are metallic and hence will not provide any passivation protection.

Though it is useful to understand the thermodynamic endpoints of the cathode/conductor reaction as shown in **Table 2-2**, comparison with the experimentally observed products clearly indicates that these phases do not always form, as would be expected under conditions where kinetics may be limited.

First, when the electrode and electrolyte are in contact, arbitrary amounts of these phases can react, forming an interface layer of decomposition products that can take on, in principle any average composition between the cathode and electrolyte composition depending on the ratio in which they react. This renders many possible reaction

pathways plausible. In our previous modeling approach, a mixing parameter x ($0 < x < 1$) between the electrode and electrolyte was introduced in our calculations (*109*, *110*). By scanning a range of x from 0 to 1, we calculated the reaction enthalpies for all possible reactions and determined the mostly likely reaction as the one with the largest thermodynamic driving force. This approach was largely successful in predicting the decomposition products between electrodes and electrolytes, and indeed, many of the predictions have recently been verified by experiments (*63*, *89*, *90*, *110*). However, it is important to keep in mind that in principle all reactions with positive driving force can take place spontaneously, and which ones occur first depends on their kinetics. To make a broader comparison with future experiments possible we have listed in **Table D-1** in **Appendix D** possible reaction products that can be formed for each cathode/electrolyte couple. Given these constraints, it is remarkable that many of the experimentally observed products are the ones predicted in the thermodynamic calculations (*83*, *84*, *111*). This finding may result from the very thin interface layer (nanometer scale) formed, requiring only very short diffusion lengths.

Several of the experimental products we observed can be explained by adding at least a qualitative layer of kinetic constraints on top of the predictions. For example, in the reaction between $NaCrO_2$ and Na_3PS_4, the theoretically predicted product (Na_3PO_4) was not observed at temperatures below 700°C. Instead, the intermediate Na_3PS_3O was formed at lower temperatures, which may be thought of as an intermediate towards the exchange of S and O in the conductor.

One reaction that however cannot be kinetically limited is the exchange of Na ions between the electrolyte and cathode. As a result, cathodes that are charged above the anodic voltage limit of the conductor will always extract Na from the solid-state electrolyte, at which point the electrolyte will degrade and decompose. This concept rationalizes our experimental observation when $Na_{0.5}CrO_2$ and Na_3PSe_4 come in contact. The results in **Table 2-2**, assuming diffusion is not limited, predicted the formation of $Na_{1/3}(CrSe_2)$, $Na_{2/3}(CrSe_2)$, and Na_3PO_4 decomposition products. However, experimentally a more limited reaction is observed whereby Na is extracted from the electrolyte, causing electrolyte decomposition, and producing fully sodiated $NaCrO_2$.

In the two cases discussed above, instead of taking the reaction pathway with the largest thermodynamic driving force, which involves diffusion and rearrangement of elements, a reaction via anion and Na exchange processes is observed. This finding is not surprising as reactions involving well-known mobile species (e.g., Na^+) are fast and kinetically favored. Overall, in the analysis of electrode/electrolyte reactions, our results suggest that in addition to the ones with the largest driving forces, other reactions with similar

thermodynamic driving forces but faster kinetics (e.g., topotactic Na extraction/insertion) should also be considered in electrode/electrolyte reactions.

With the driving forces that may degrade the cathode/electrolyte interface better understood, one can develop strategies to alleviate these. The anion-exchange reaction is mainly driven by the tendency to form the stable phosphate group. Therefore, this type of reaction may be prevented by fully or partially replacing P in the solid electrolytes with other suitable elements that do not exhibit strong bonding preference with O, such as Sb, Ge, Sn, or As. Interestingly, recent studies suggest that a $NaCrO_2$ cathode can be cycled reversibly using a Na_3SbS_4 solid-state electrolyte, indicating that replacing P with Sb in the sulfide electrolyte resulted in improved compatibility with the oxide cathode (*83*, *84*, *112*). We expect that a similar effect will be observed for Na_4SnS_4, Li_4SnS_4, Li_4GeS_4, Li_3AsS_4, and similar materials. Another possible strategy to prevent the anion exchange is to use polyanion cathodes with stable anion groups such as PO_4. Since the O is already in a stable configuration, it is unlikely to participate in the anion exchange reaction. Changing from an oxide-based cathode to a sulfide-based cathode will also mitigate the interface issue, although sulfide-based cathodes will operate at a lower voltage than their oxide counterparts, thus reducing the overall energy density of the batteries. The redox degradation pathway requires transition metal reduction in the cathode. While this seems inevitable in a charged cathode, it may be preventable in the discharged cathode by selecting transition metals that are difficult to reduce (e.g., Cr^{3+} Mo^{3+}, V^{3+}, Nb^{3+} and Ti^{3+}). The thermodynamic stability requirement between the conductor and discharged cathode is often more stringent as processing of a solid-state battery may bring this system to elevated temperature. This is not the case for the charged cathode which is usually only exposed to the conductor during room temperature operation.

Finally, one always has the option to coat the electrode to protect it chemically from the electrolyte (*81*, *112*). Because the coating is a thin layer, it has less stringent requirements for ionic conductivity than for the bulk electrolyte. This allows many more materials choices than for bulk electrolytes, making the selection of a chemically and electrochemically stable coating material more likely (*81*, *113*). The coating materials and their effectiveness will be discussed in the next Chapter. However, we believe that passivating solid-state electrolytes is equally important and should be explored in future studies. Coating only the cathode still exposes the electrolyte to electronic pathways created by carbon in the cathode. According to our electrolyte stability testing results, it is clear that electronic pathways promote the decomposition of the electrolyte via the extraction of Na^+ and oxidation of the anion in the conductor. Therefore, the electrode coating method only solves the cathode/electrolyte interface problem and cannot prevent electrolyte decomposition at voltages beyond its stability window. The breakdown of

solid electrolyte at interfaces at which electrons are available and its effect on cell performance will also be discussed in the next Chapter.

Chapter 3.

Development of borate cathode coating and analysis of first cycle capacity loss in solid-state batteries

The instability of the interface between a thiophosphate solid electrolyte and oxide cathodes results in rapid capacity fade and poor rate performance and has driven the need for protective cathode coatings. In this chapter, we first compare the stability, evolution, and performance of uncoated, Li_2ZrO_3 (LZrO)-coated, and (LBO)-coated $LiNi_{0.5}Co_{0.2}Mn_{0.3}O_2$ (NCM^{523}) cathodes. LBO is identified as a superior coating material that exhibits high oxidation stability, excellent chemical stability with both thiophosphate electrolytes and oxide cathodes, leading to a full-cell performance that is substantially improved over cells with LZrO-coated or uncoated NCM cathodes. The chemical and structural origin of the different performance is interpreted using different modes of electron microscopy techniques which enable the direct observation of the phase decomposition and morphological change of the LZrO coating.

While the application of a LBO coating protects the interface between NCM cathode and LPS electrolyte in cathode composite, the intrinsic electrochemical instability of the sulfide electrolyte is relevant wherever the solid electrolyte is in contact with the electron reservoir. Therefore, the capacity loss in a solid-state battery, in particular during the first cycle, is related to the decomposition of the sulfide conductor under high voltages. Later in this chapter, the following scientific question is answered by detailed lattice parameter analysis: what is "capacity" contribution caused by the decomposition of solid electrolyte under high voltage in the first cycle?

The content of this chapter is based, often verbatim, on the following manuscripts which are published or in preparation for publication. Some results presented in this chapter were obtained by a collaborative effort. Contribution from collaborators are made explicit in relevant results.

[1] Yaqian Zhang†, Yaosen Tian†, Yihan Xiao, Lincoln J. Miara, Gerbrand Ceder, et al. "Direct visualization of the interfacial degradation of cathode coatings in solid state batteries: a combined experimental and computational study." *Submitted*. († equal contribution)

3.1. Introduction

It has been demonstrated in the previous chapters that thiophosphate SEs and commonly used oxide cathode materials are not stable in contact with each other. This interfacial instability leads to increased resistance during cycling (*51*, *89*, *113*, *114*), resulting in

capacity fade and poor rate performance, indicating the need for interface engineering in SSBs. To suppress the reaction between the cathode and thiophosphate SEs, various cathode coating materials have been developed to serve as a buffer layer and prevent direct contact between the cathode and SE (*81*, *115*). Most investigations on cathode coatings in thiophosphate-based SSBs have focused on exploring ternary metal oxides (*115*) such as $LiNbO_3$ (*114*, *116*, *117*), $LiTaO_3$ (*116*, *117*), and Li_2ZrO_3 (LZrO) (*118*, *119*). However, such coating materials do not completely solve the interfacial issue between the cathode and SE. For example, despite the reduced interfacial resistance and enhanced capacity retention achieved in SSBs using $LiNb_xTa_{1-x}O_3$ coatings, Co diffusion from the LiCoO2 cathode to the thin film coating is still observed (*116*). First-principles computation also indicates that the high binding energy of a PO_4 group creates a driving force for S/O exchange between $LiNbO_3$, $LiTaO_3$, and LZrO coatings and thiophosphate SEs (*117*). In addition, the relatively low oxidation limit of these ternary-metal-oxide coatings raises concern for their stability at high voltages(*14*, *118*).

An ideal coating material, therefore, requires a wide stability window that spans the cathode operating voltage and has low reactivity with both cathode and SE. Recently, with the aid of first-principles computations, lithium borates have been identified as a promising class of cathode coating materials with low reactivity with oxide cathodes and thiophosphate SEs as well as good oxidation stability (*113*). Although computational screening has provided an efficient way to identify ideal compositions with targeted properties, experimental validation and direct observations of how different coatings behave in a certain (electro-)chemical environments is crucial for the development of new coatings. Various methods have been established to investigate interfaces in liquid-electrolyte battery systems; however, obstacles remain in studying the interface behavior in SSBs, in part because of the difficulty of isolating an intact solid/solid interface in SSBs (*118*). The characterization of the complex interparticle interfaces is further hindered by the nano-sized length scale, air sensitivity, and amorphous nature of some decomposition products (*14*, *120*). Advanced (scanning) transmission electron microscopy ((S)TEM) analysis with air-free sample preparation and transfer enables accurate probing of the chemical/structure evolution of the solid-state interfaces in SSBs (*89*, *113*). In this paper, we combine different microscopy techniques (imaging, diffraction, and spectroscopy) to probe the chemical composition and microstructure of cathode composite interfaces with nanoscale resolution.

In this chapter, we select the lithium borate $Li_3B_{11}O_8$ (LBO) for detailed investigation because of its high oxidation stability limit and good chemical compatibility with both layered oxide cathode $LiNi_{0.5}Co_{0.2}Mn_{0.3}O_2$ (NCM^{523}) and glassy Li_3PS_4 (LPS) thiophosphate SE. Electrochemical methods were used to test the coating's effect on the discharge capacity and cycle-life of the SSB full cells. LZrO, which is predicted to be

unstable at high voltage, was also characterized for comparison purposes to help identify the factors contributing to the coating stability. Compared with the uncoated and LZrO-coated NCM^{523}, the LBO-coated NCM^{523} exhibits a greatly improved discharge capacity and capacity retention. The chemical and structural origin of the differences observed in the electrochemical behavior are interpreted using (S)TEM to observe the coatings and interfaces present in the cathode composite.

While the borate coating protects the interface between NCM^{523} and LPS, the intrinsic instability of LPS is relevant to the LPS/electron interfaces, which is likely the reason of the large first-cycle capacity loss often observed in SSBs. Later in this chapter, we will employ *in situ* synchrotron XRD to study the contribution from LPS electrochemical decomposition to the overall first-cycle capacity loss. During the cycling of the SSB cell, X-ray will be collected to monitor the change of the cathode composite. With the accurate lattice parameter information gained from the structure analysis of NCM^{523}, the real capacity from cycling NCM^{523} will be obtained. Therefore, the "capacity" from the decomposition of LPS can be distinguished from the total observed charge count.

3.2. DFT computation of coating stability

The electrochemical stability window of LPS, LZrO, and LBO and the decomposition products at a given Li chemical potential are predicted using a first-principles methodology described in **Appendix C.** Detailed results are summarized in **Figure 3-1a**[10]. The blue-filled area in **Figure 3-1a** represents the thermodynamic stability window, and the window indicated by the dashed lines represents the maximal extended kinetic oxidation limit. As observed in **Figure 3-1a**, the stability windows of both LZrO and LBO overlap with that of LPS. However, the two coatings have divergent stabilities at ~4.3 V vs. Li/Li$^+$. LZrO is predicted to become thermodynamically unstable at 3.42 V. Although the stability window can be kinetically expanded, LZrO will likely undergo decomposition within the common operating voltage window of NCM^{523} cathode (*e.g.*, 2.5 - 4.3 V). When charged to 4.3 V or higher, LZrO is likely oxidized by Li extraction *via* the predicted decomposition reaction expressed in **(3-1)**. In contrast, LBO exhibits a higher thermodynamic oxidation limit of 4.45 V due to the strong hybridization between boron and oxygen, indicating that the LBO coating over the entire battery cycling voltage range of 2.5 - 4.3 V.

$$Li_2ZrO_3 \rightarrow 2\,Li + ZrO_2 + 0.5\,O_2 \qquad \textbf{(3-1)}$$

[10] DFT computations were performed by collaborator Mr. Yihan Xiao (UC Berkeley, Ceder Group Graduate Student).

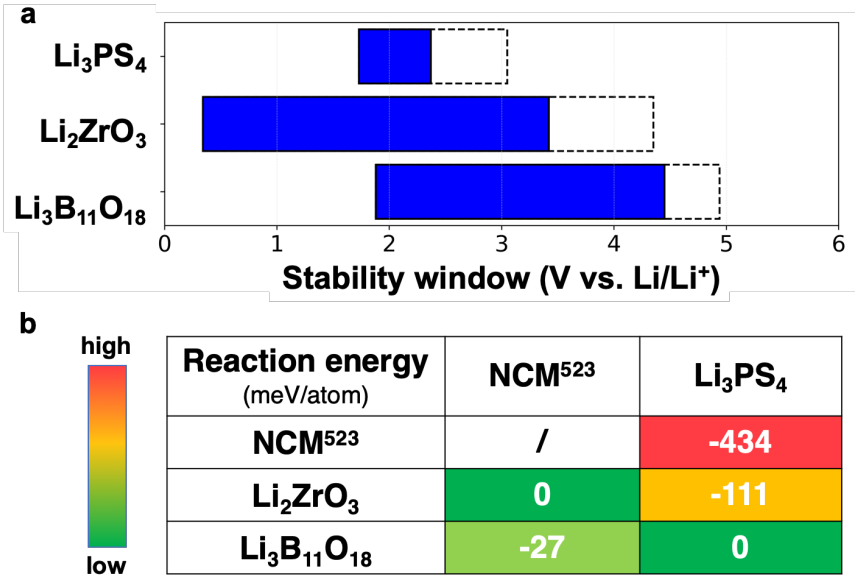


Figure 3-1 DFT computation of stability of Li_2ZrO_3 (LZrO) and $Li_3B_{11}O_{18}$ (LBO) coatings. (a) Stability window of LPS, LZrO and LBO. (b) Chemical reactivity energies (in meV/atom) of reaction pairs among NCM^{523}, LPS, LZrO, and LBO.

We also considered the chemical stability at the cathode/SE, cathode/coating, and coating/SE interfaces (**Figure 3-1b**). Negative values indicate a driving force for reaction. With no buffer layer, a high reactivity of -434 meV/atom is predicted between discharged NCM^{523} and LPS, indicating a highly unstable interface upon direct contact. Both LZrO and LBO coatings exhibit significantly reduced reaction driving forces with NCM^{523} (0 meV/atom for LZrO and -27 meV/atom for LBO). For the LPS/coating interface, a non-negligible driving force exists between the LZrO coating and LPS (-111 meV/atom) to form Li_3PO_4, whereas LBO is thermodynamically stable in contact with LPS. Therefore, NCM^{523}/LPS interface than LZrO, and provides a wide stability window spanning the voltage range of typical NCM^{523} cathodes. A full list of the computed reactivities and the predicted reactions of all the reaction pairs is provided in **Table D-2** in **Appendix D**.

3.3. Effectiveness of LZrO and LBO coatings

To experimentally investigate the stability and effectiveness of the two coatings, both LBO-coated and LZrO-coated NCM^{523} were prepared using sol-gel coating methods as shown in **Figure 3-2** (described in detail in the **Appendix B-1**). Electron microscopy images of the uncoated/coated NCM^{523} particles are presented in **Figure 3-3**. As observed in the scanning electron microscopy (SEM) images in the top three panels of **Figure 3-3**, the morphology of the NCM^{523} secondary particles is preserved after the coating process. TEM and high-resolution transmission electron microscopy (HRTEM) images indicate that the uncoated NCM^{523} particle has a clean surface with lattice fringes extending to the particle edge (**Figure 3-3b** and **3-3c**)[11]. As observed in the TEM and HRTEM images in **Figure 3-3e-f** (for the LZrO-coated NCM^{523}) and **Figure 3-3h-i** (for the LBO-coated NCM^{523}), a thin and uniform coating layer ranging from a few nanometers to approximately 10 nm in thickness is observed on the surface of the NCM^{523} particles. The HRTEM images in **Figure 3-3f** and **3-3i** reveal amorphous features for both the LZrO and LBO coatings.

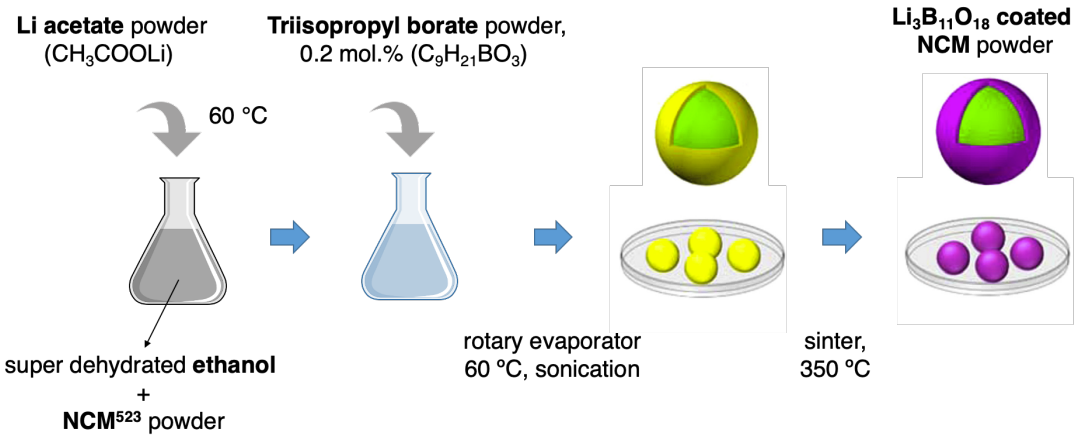


Figure 3-2 Coating procedure using a sol-gel method. The precursors of the LBO coating are shown in the figure.

[11] TEM and HRTEM experiments were performed by collaborator Dr. Yaqian Zhang (UC Berkeley).

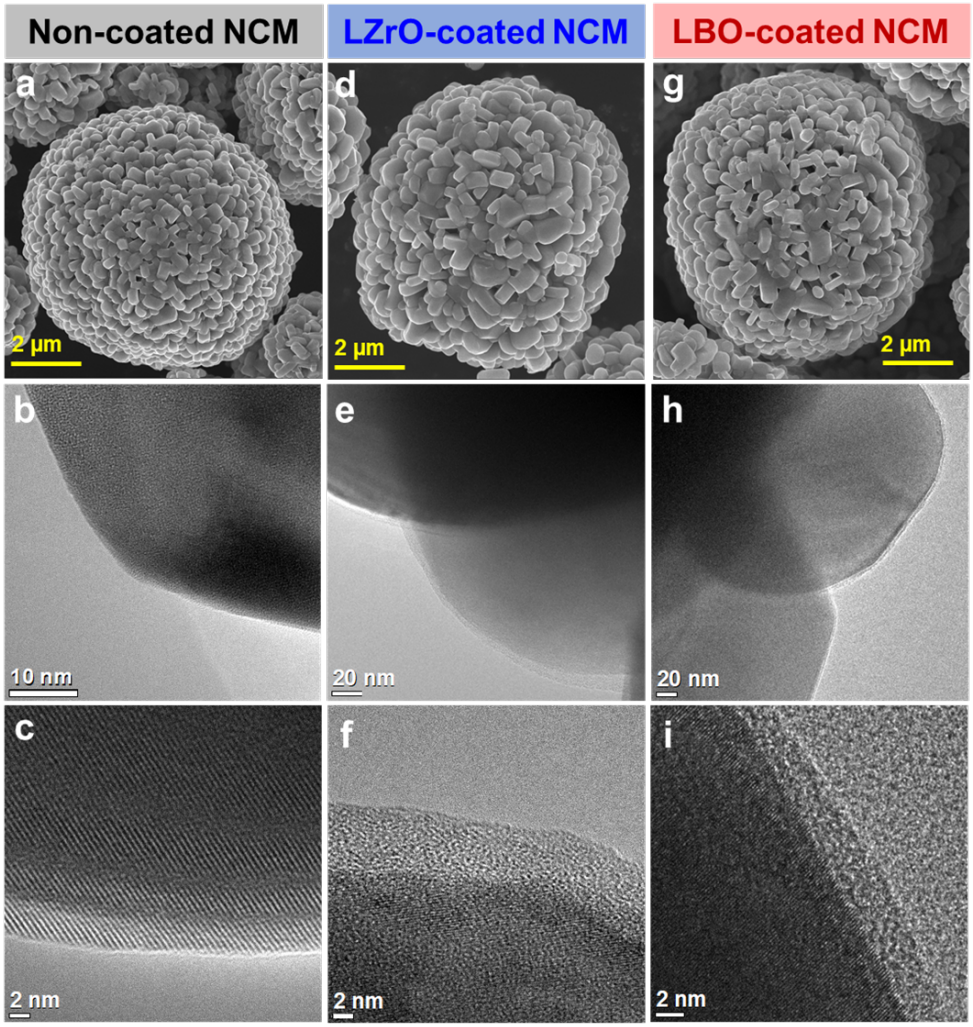


Figure 3-3 SEM, TEM, and HRTEM images of the morphology of uncoated/coated NCM^{523} particles: (a-c) uncoated NCM^{523}, (d-f) LZrO-coated NCM^{523}, and (g-i) LBO-coated NCM^{523}. The scale bars are presented individually.

Full-cell SSBs using the uncoated/coated NCM^{523} cathodes were constructed and cycled at a constant current (0.05 mA cm^{-2}) between 2.5 and 4.3 V vs. Li/Li^+ to evaluate the effectiveness of the LBO and LZrO coatings. The cells were assembled in an Ar atmosphere using identical procedures; LPS powder from the same batch was used to maximize consistency. **Figure 3-4** presents the discharge capacity and capacity retention of the cells for the first 100 cycles. Among all the cells constructed, the uncoated NCM^{523} cathode exhibits the lowest discharge capacity (107.1 mAh g^{-1} in the 1^{st} cycle) and the worst capacity retention (42.7% after 100 cycles). The corresponding electrochemical cycling curves are presented in **Figure 3-5, 3-6** and **3-7**. Both coatings improve the full-cell performance, providing larger capacity and higher retention. Compared with the

LZrO coating, the LBO coating yields a significantly enhanced discharge capacity (146.5 mAh g^{-1} in the 1st cycle) and superior cycling stability (78.0% capacity retention after 100 cycles), suggesting a more effective protection of the NCM^{523}/LPS interface. This observation is consistent with our DFT computation, in which LBO is predicted to exhibit excellent chemical compatibility and electrochemical stability at a high cut-off voltage of 4.3 V.

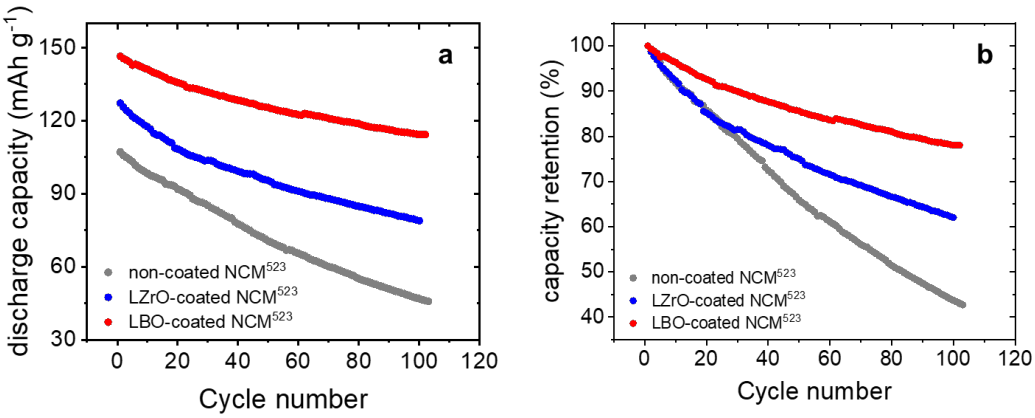


Figure 3-4 Electrochemical cycling of full cells using uncoated (grey), LZrO-coated (blue), and LBO-coated (red) NCM^{523} cathodes: discharge capacity (a) and capacity retention (b).

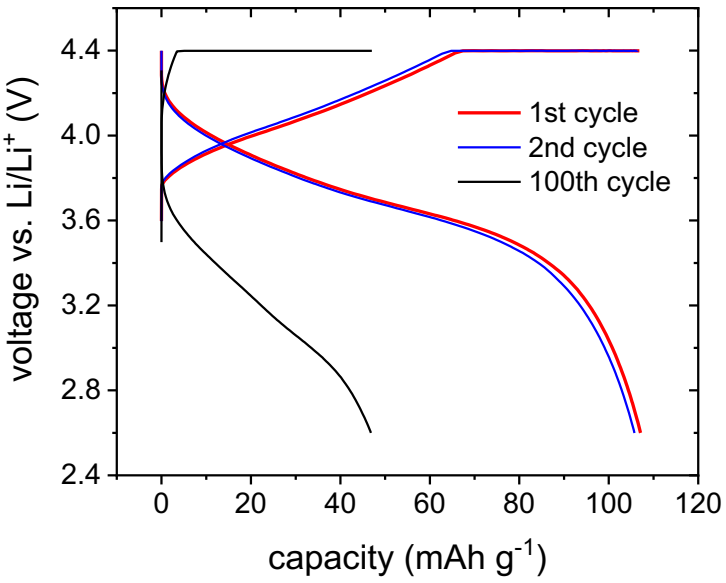


Figure 3-5 Electrochemical cycling of full cells using uncoated NCM^{523} cathodes.

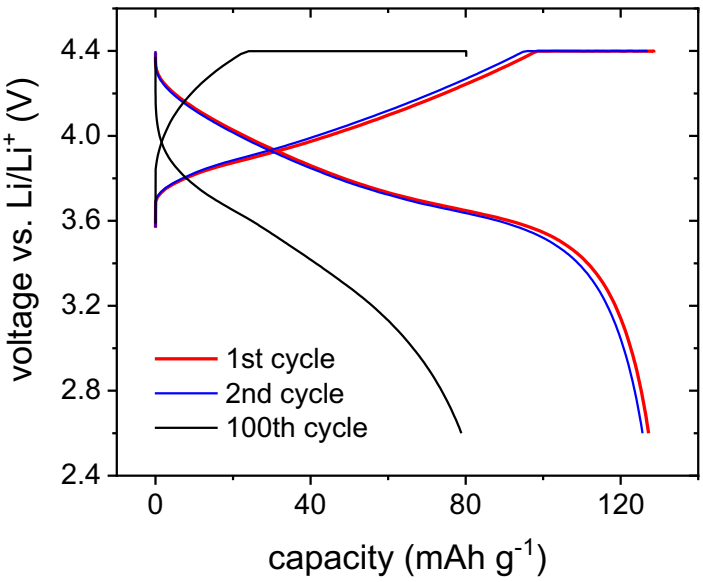


Figure 3-6 Electrochemical cycling of full cells using LZrO-coated NCM^{523} cathodes.

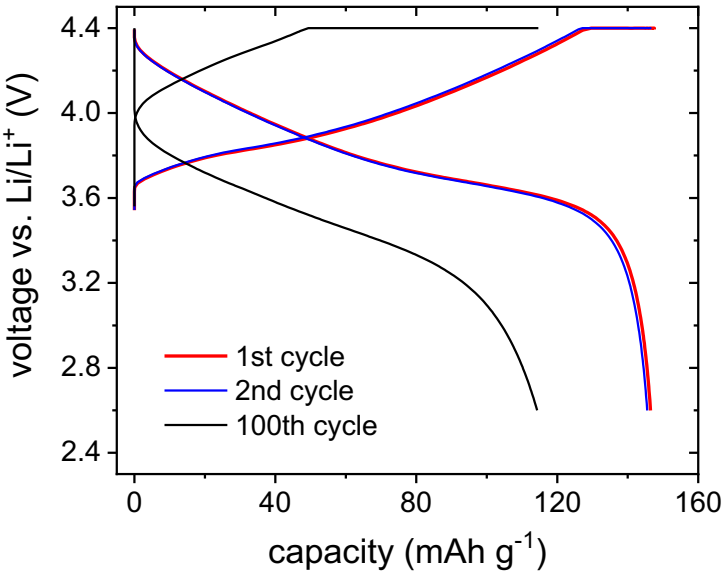


Figure 3-7 Electrochemical cycling of full cells using LBO-coated NCM^{523} cathodes.

To better understand the electrochemical behavior of NCM^{523} with different cathode coatings, (S)TEM was used to investigate the coating integrity and interphase formation during cycling. HRTEM images of the LBO-coated and LZrO-coated NCM^{523} in composite cathodes before any electrochemical cycling are presented in **Figure 3-8a** and **3-8c**, respectively[12]. Both the LBO and LZrO coatings are amorphous and intact after mixing with LPS and carbon nanofibers (CNFs). The morphology and amorphous nature of LBO coating remain unchanged after the 1st cycle (**Figure 3-8b**). In contrast, after the 1st cycle, the LZrO coating transformed from an amorphous layer into nanocrystalline phases with non-homogeneous coverage on the surface of the NCM^{523} particles, as observed in **Figure 3-8d**. As shown in the fast Fourier transform (FFT) image inserted in **Figure 3-8d**, the observed nanocrystalline phase can be indexed to the cubic ZrO_2 structure (space group $Fm\bar{3}m$, ICSD No. 53998). This phase transformation is likely the result of the Li extraction from LZrO under high voltage, consistent with the theoretical prediction expressed by **Reaction (3-1)**. The high-angle annular dark-field scanning transmission electron microscopy (HAADF-STEM) image and energy-dispersive X-ray spectroscopy (EDX) mapping in **Figure 3-8e-f** reveals the elemental distribution of Zr and Mn in the LZrO coated NCM^{523} after the 1st cycle. In contrast to the homogenous coating of 5-nm thickness observed for the sample before cycling in **Figure 3-8c**, the decomposition of LZrO resulted in the formation of an aggregated region of approximately 70-nm thickness (**Figure 3-8e-f**).

[12] (S)TEM characterization of the NCM^{523}-LPS cathode composite samples was performed by collaborator Dr. Yaqian Zhang (UC Berkeley).

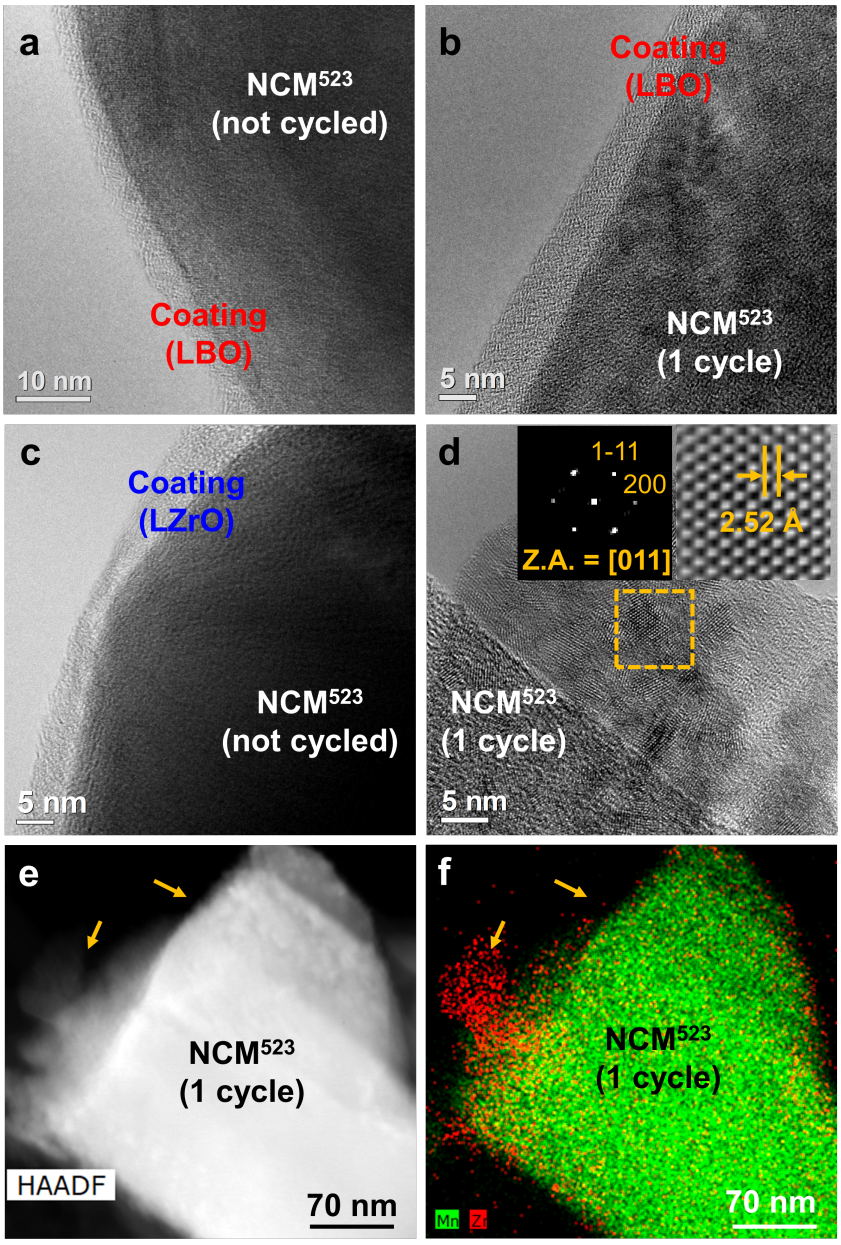


Figure 3-8 Comparison of LZrO- and LBO- coated NCM^{523} cathode composite prior to electrochemical cycling and after 1st cycle. (a) HRTEM image of LBO-coated NCM^{523} (mixed with LPS and CNF, prior to electrochemical cycling); (b) HRTEM image of LBO coated NCM^{523}/LPS/CNF after 1st cycle. (c) HRTEM image of LZrO-coated NCM^{523} (mixed with LPS and CNF, prior to electrochemical cycling); (d) HRTEM image of LZrO-coated NCM^{523}/LPS/CNF after 1st cycle (showing the decomposition product of ZrO_2); (e) HAADF-STEM image and (f) elemental mapping of LZrO coated sample after 1st cycle, showing the aggregation of the decomposition product.

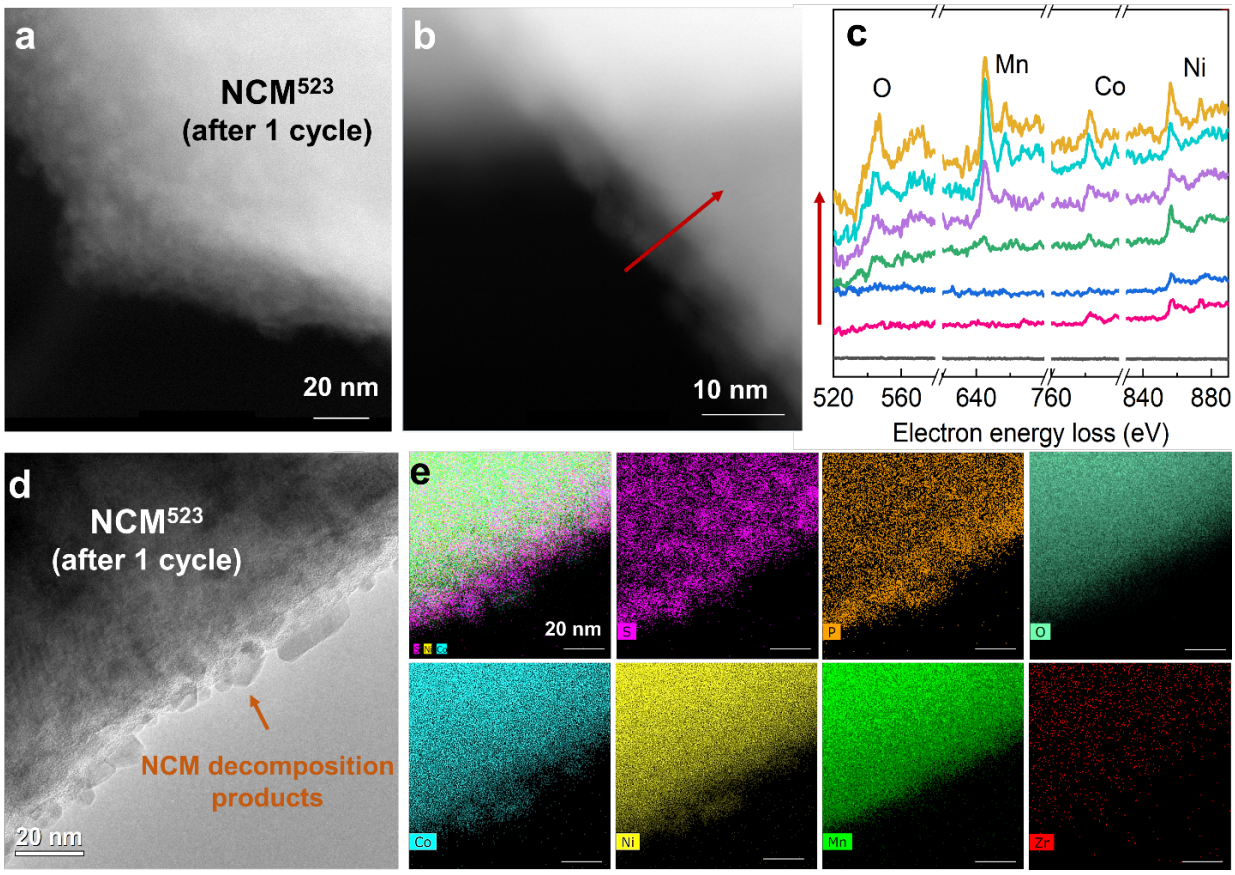


Figure 3-9 LZrO-coated NCM^{523} cathode composite after 1st cycle. HAADF-STEM images of LZrO coated NCM^{523} after 1 cycle (a-b), corresponding EELS line scan spectrum (c), TEM image (d) and EDX elemental mappings (e).

After the LZrO coating breaks down, NCM^{523} is likely to be subjected to direct contact with LPS, leading to the formation of a highly unstable interface. The HAADF-STEM image in **Figure 3-9a** shows the morphology of the LZrO-coated NCM^{523} after the 1st cycle; the surface of NCM^{523} is rough and mostly covered by island-like nanocrystals. As observed in the scanning transmission electron microscopy - electron energy loss spectroscopy (STEM-EELS) line scan spectra in **Figure 3-9b-c**, inhomogeneous distributions of Ni, Mn, and Co can be observed from the edge to the bulk region. Notably, although signals from Ni and Co are observed in the first few EELS line spectra in **Figure 3-9c** (corresponding to the edge of the NCM^{523} particle), the signal from oxygen can barely be detected. This result suggests that Ni and Co no longer exist in the oxide form at the very surface and the elemental inhomogeneity is not due to the typical surface segregation and densification observed in layered lithium transition metal oxide

cathodes in liquid-electrolyte battery systems.[,] Overlap of Ni, Co, and S is observed in the EDX mappings in **Figure 3-9e**, suggesting the possible presence of transition metal sulfides in the decomposition products.

In contrast to the phase decomposition and aggregation observed in the LZrO-coated sample, the LBO coating remains amorphous and intact even after extended cycling in an SSB. As observed in **Figure 3-10a**, the morphology and amorphous nature of the LBO coating are well preserved after 10 cycles. A uniform distribution of the LBO coating on the NCM^{523} particle after 10 cycles is observed in the EDX mappings in **Figure 3-10b-c**. The HAADF-STEM image of the LBO-coated NCM^{523} after 10 cycles is presented in **Figure 3-10d**, with a clean surface of the coated NCM^{523} particle observed in the interface region in contact with the LPS particle. With the protection of the intact LBO coating, no interfacial reaction between LPS and NCM^{523} is detected in the LBO-coated samples. Homogeneous distributions of different elements are also found in the corresponding EELS line spectra of the LBO-coated NCM^{523} sample in **Figure 3-10d-e**, indicating the chemical integrity of the NCM^{523} particle. The atomic-resolution HAADF-STEM image in **Figure 3-10f** shows the crystalline structure of the LBO-coated NCM^{523} after 10 cycles, in which the bright and dark columns correspond to atomic columns of transition metal cations and Li-ions, respectively. Interestingly, the Z-contrast difference decreases in the edge region of the NCM^{523} crystal compared with that in the bulk region (**Figure 3-10f**). The FFT image of the edge area reveals a rock-salt structure (inset of **Figure 3-10f**), indicating that the surface structure of NCM^{523} changed from a layered structure ($R\bar{3}m$) to a rock-salt structure ($Fm\bar{3}m$), similar to the surface densification reported in liquid-electrolyte battery systems. While this may contribute to the observed capacity fade, the LBO coating remains stable with long-term operation as shown by the electron microscopy images of the well-preserved LBO coating after 50 cycles (**Figure 3-12** and **3-13**).

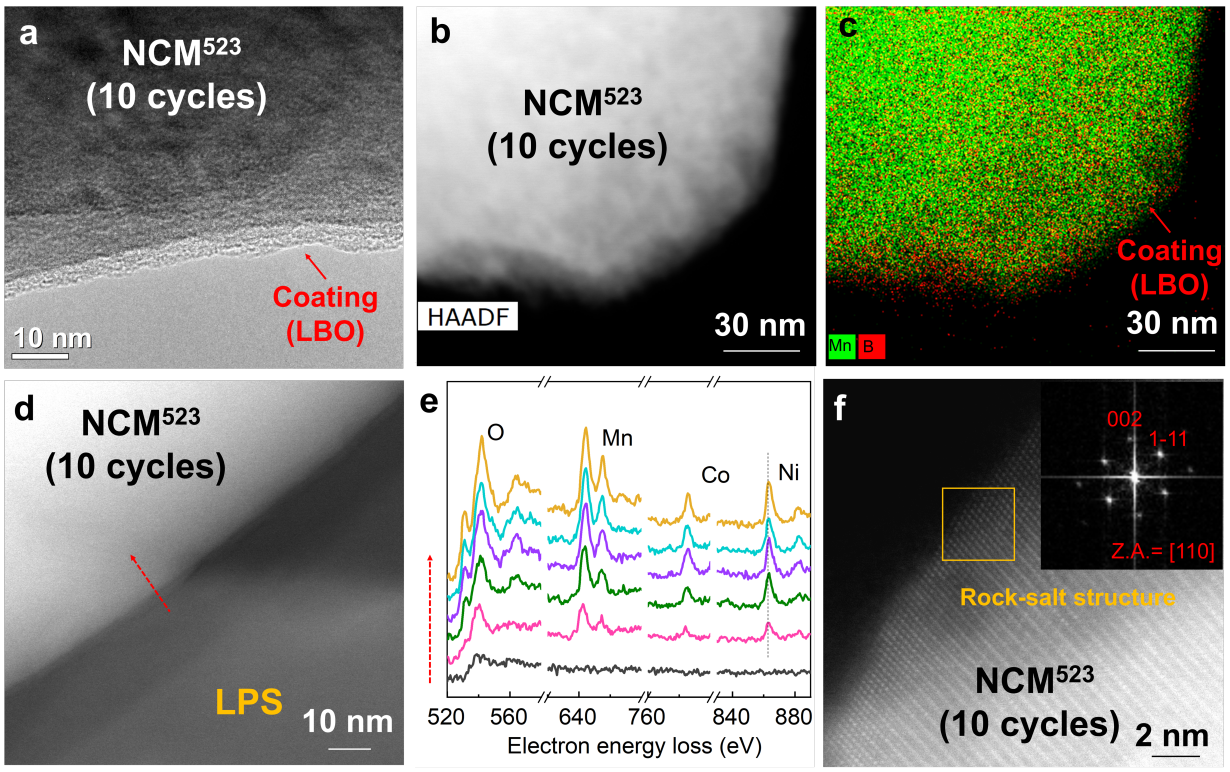


Figure 3-10 LBO-coated NCM^{523} cathode composite after 10 cycles. HRTEM image (a), HAADF-STEM image (b) and elemental mapping (c) of LBO-coated NCM^{523}; (d) HAADF-STEM image of LBO-coated NCM^{523} with LPS interface with corresponding (e) line scan EELS spectrum from surface of LBO-coated NCM^{523} to the bulk after 10 cycles shown in (d). (f) HR-STEM image of LBO coated NCM^{523}after 10 cycles.

3.4. Interfacial reaction(s) between NCM and LPS

To further investigate the NCM^{523}/LPS interparticle interface and decomposition products after breakdown of the LZrO coating, HAADF-STEM and EDX analysis of the LZrO-coated sample after long-term cycling was performed. **Figure 3-11** presents the STEM-EDX analysis of the NCM^{523}/LPS particles after 50 cycles. The reaction between NCM^{523} and LPS led to the formation of an extended interface region, as observed in **Figure 3-11a**. According to the elemental mapping in Figure 7c, the distributions of Ni and Co are well overlapping in the decomposition region, but spatially separated from the distribution of Mn (**Figure 3-11b**, overlay map of Ni/Mn). This finding is consistent with the computational prediction expressed by **Reaction (3-2)**, where MnS_2 and $CoNi_2S_4$ compounds are predicted to be products of the reaction between NCM^{523} and LPS. Notably, some of the decomposition products, such as $Co(NiS_2)_2$, are likely to be electronically conductive. Thus, the electrochemical decomposition of LPS may not be

passivated by the chemical reaction between NCM^{523} and LPS, leading to a progressive degradation with long-term cycling and significant capacity fade.

$$0.332\ Li_3PS_4 + 0.668\ LiMn_{0.3}Co_{0.2}Ni_{0.5}O_2 \rightarrow 0.007\ Ni_9S_8 + 0.2\ MnS_2 + 0.332\ Li_2S + 0.134\ Co(NiS_2)_2 + 0.332\ Li_3PO_4 + 0.002\ Li_2SO_4 \quad \textbf{(3-2)}$$

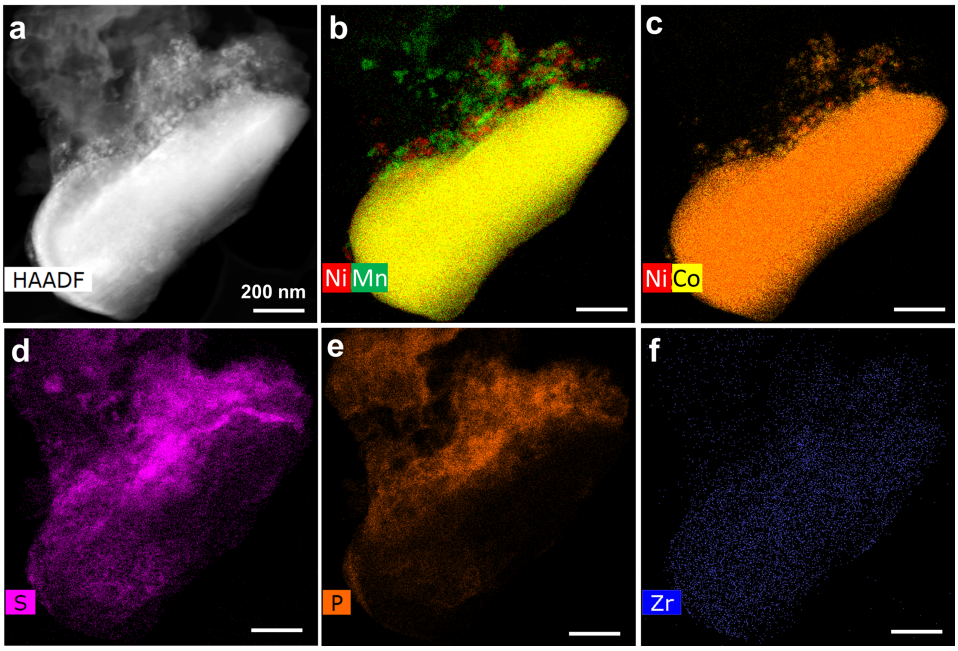


Figure 3-11 LZrO-coated NCM^{523} cathode composite after 50 cycles. HAADF-STEM image (a) and EDX elemental mappings (b-f)

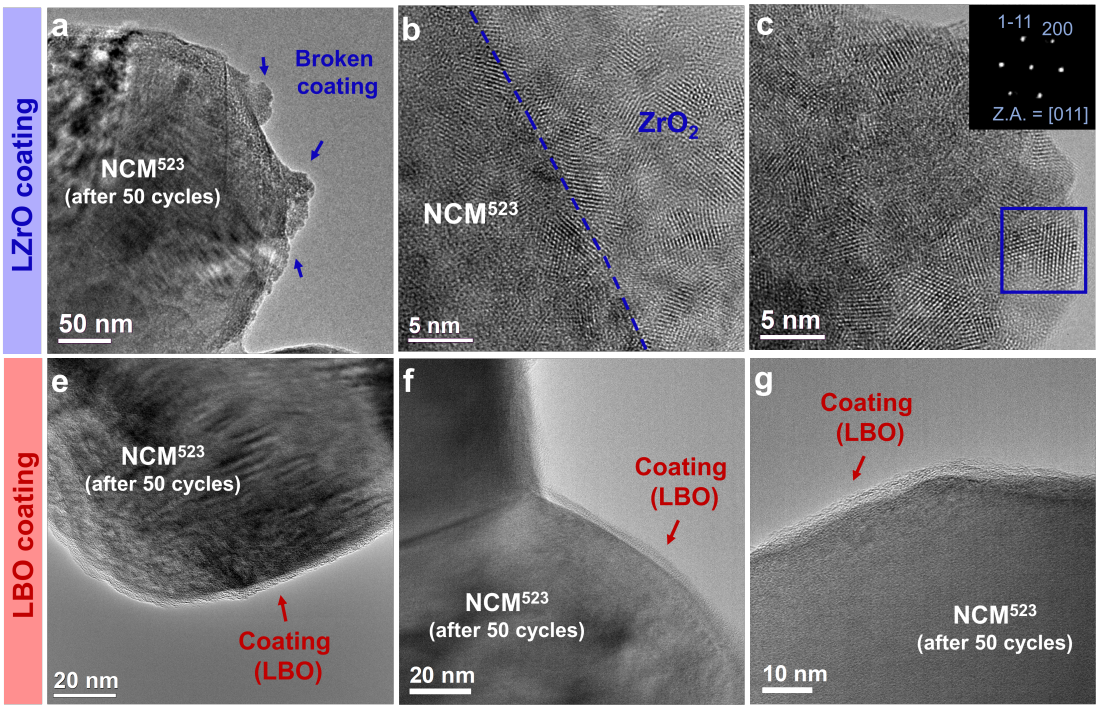


Figure 3-12 LZrO/LBO coated NCM^{523} cathode composite after 50 cycles. TEM and HRTEM images of the LZrO-coated sample (a-c), showing the morphology change and phase decomposition of the LZrO coating; TEM images of the LBO-coated NCM^{523} sample (e-f).

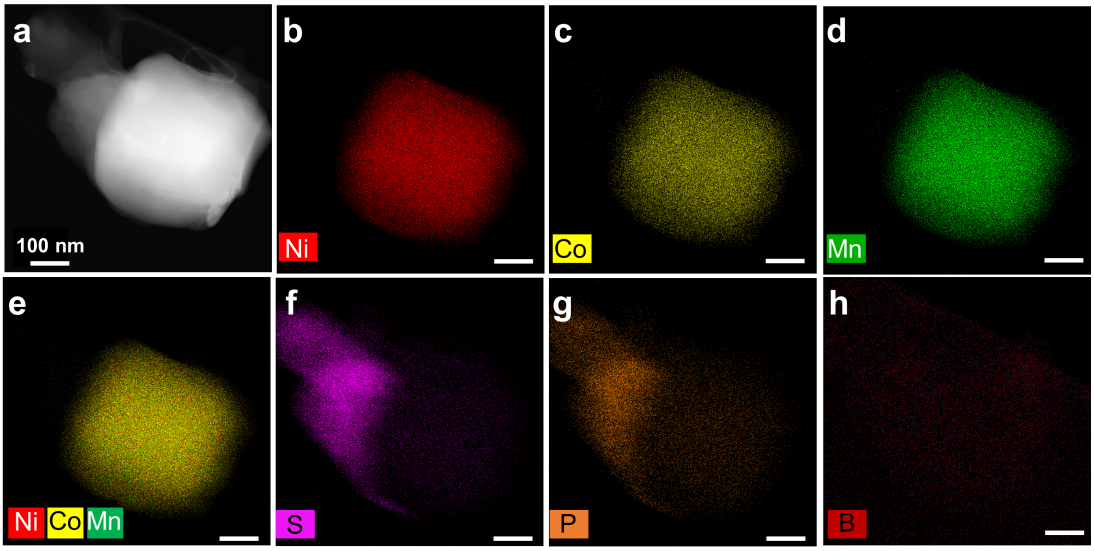


Figure 3-13 HAADF-STEM image and EDX mappings of LBO coated NCM^{523} after 50 cycles.

3.5. Instability of LPS and first-cycle capacity loss in SSBs

As shown in the last section, the LBO coating protects the interface between NCM^{523} and LPS. However, the LPS electrolyte is still exposed to conductive additives, therefore is subjected to decomposition beyond its stability voltage range. Such intrinsic instability is relevant on the electrolyte/electron interfaces, which is likely associated with the large first-cycle capacity loss in SSBs compared with LIBs observed in **Figure 3-7**.

The lattice parameters of NCM during electrochemical cycling were obtained by *in situ* synchrotron XRD experiments. We design a solid-state battery that allows precise pressure control during cycling based on the previous Radially Accessible Tubular In-situ X-ray (RATIX) cell (*121*) (Figure **3-13**). The cell was oriented vertically, with the X-ray beam transmitted through the cell horizontally (inset of **Figure 3-13**) on the plane parallel to the cell. The precise pressure control allows the solid-state battery to be cycled under the same condition as in the regular cell. The first cycle cycling performance of the LBO-coated NCM^{523} using different cell set-up are presented in **Table 3-1**, in which full-cell SSBs using different cell designs deliver similar capacity under same current density.

The *in situ* SXRD patterns of NCM and corresponding cycling curve of the first two cycles are presented in **Figure 3-14**. Unit cell volume of NCM lattice corresponding to each XRD pattern was obtained by Rietveld refinement (**Figure 3-15**). In the beginning of the first cycle (~5 mAh g^{-1}, labelled as region 1 in **Figure 3-15**), a small plateau is observed in **Figure 3-15a**, and the unit cell volume of NCM remains same, indicating the capacity observed is not a result of Li extraction of the NCM structure. Given the voltage is higher than the stability limit of LPS, the plateau is likely correlated to Li extraction of LPS. At the end of the discharge process of the first cycle, unit cell volume of NCM is smaller than the one of the pristine NCM as shown in **Figure 3-15b**. The corresponding capacity loss (~20 mAh g^{-1}, labelled as region 2 in **Figure 3-15b**) is therefore correlated to NCM not being fully discharged. This is likely because of the contact loss between charged (shrunk) NCM particles and LPS particles in cathode composite (*121*). Region 3 in **Figure 3-15b** presents irreversible capacity from NCM of the same unit cell volume (i.e., same state of charge). It is likely a result of Li extraction of LPS under higher voltage after the decomposition plateau (Region 1) in the charging process.

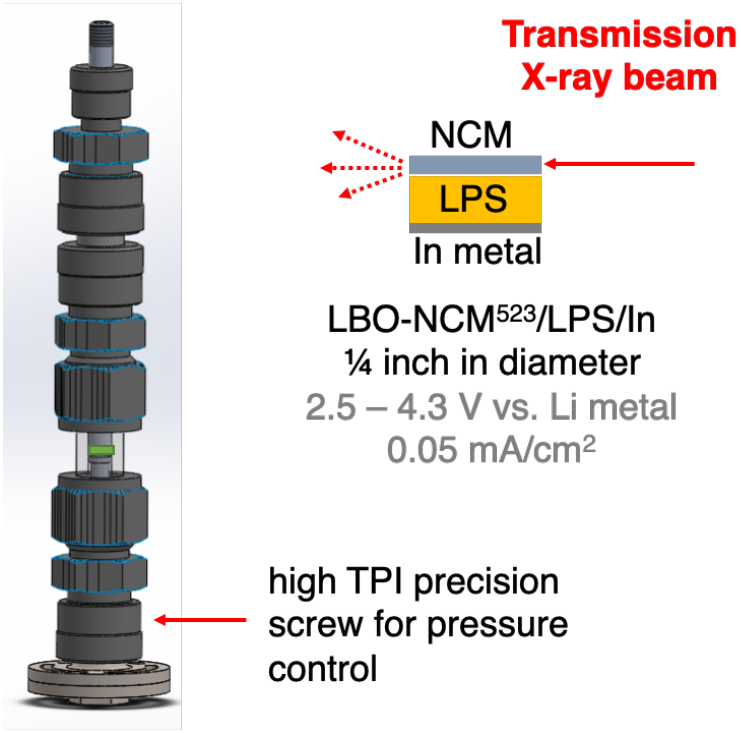


Figure 3-13 SSB cell for *in situ* synchrotron XRD measurement. The cell was oriented vertically and cycled at a constant current (0.05 mA cm^{-2}), with the X-ray beam transmitted through the cell horizontally. The size of the beam was reduced to 20 μm in the vertical direction along the cell.

Table 3-1 First cycle capacity of LBO-coated NCM^{523} cycled in different SSB cells under 0.05 mA cm^{-2}

0.05 mA cm^{-2}	**Regular design**	***In situ* design**
1st Charge	>190 mAh/g	193 mAh/g
1st Discharge	>150 mAh/g	153 mAh/g

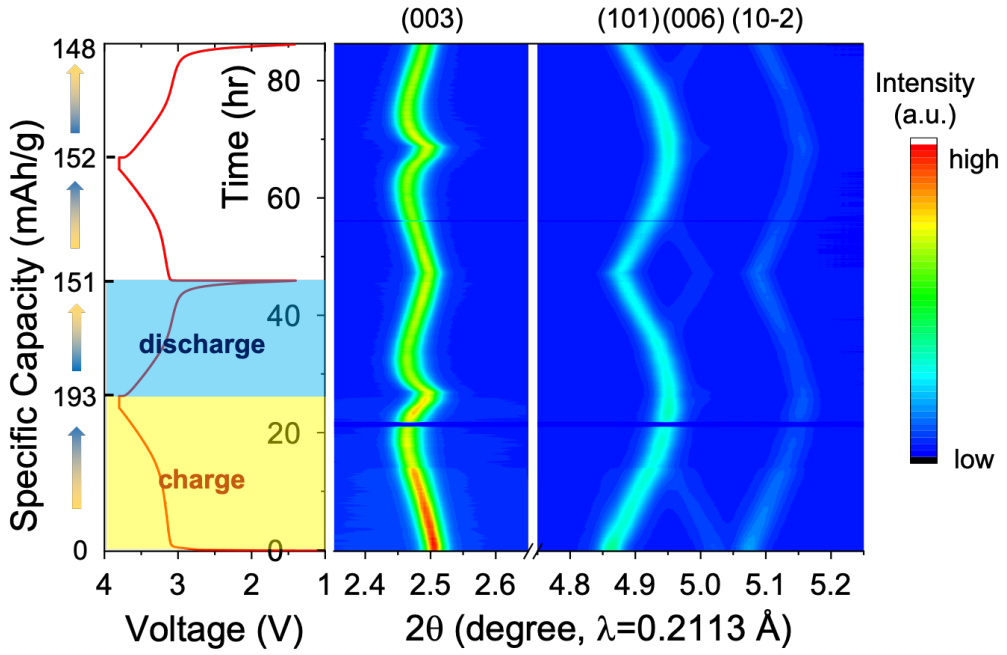


Figure 3-14 *In situ* XRD and electrochemical cycling of full-cell SSB using LBO-coated NCM^{523} active cathode. The high intensity contour in the XRD map corresponds peaks from NCM. Lattice parameter change of NCM during electrochemical cycling can be observed by peak shifting.

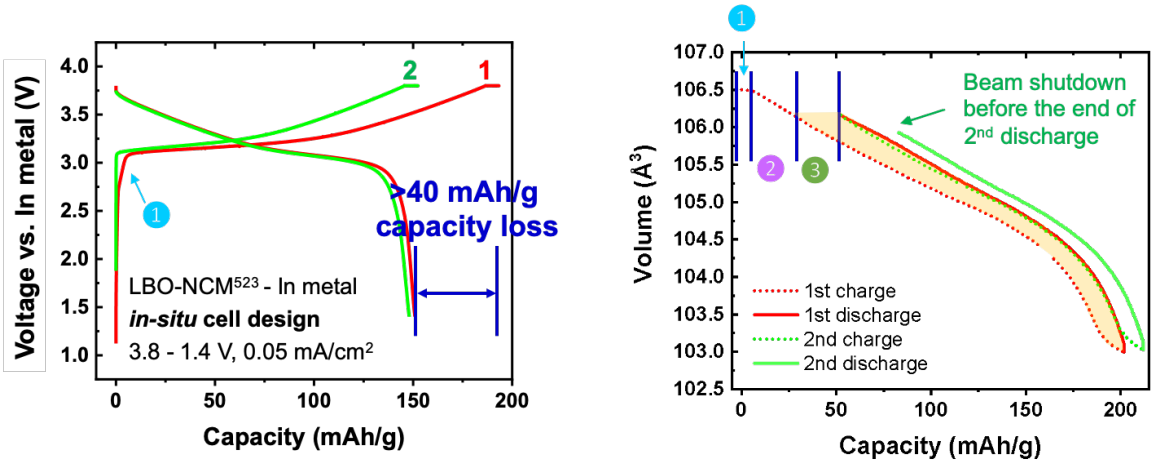


Figure 3-15 Lattice parameters of NCM^{523} during electrochemical cycling. (a) Electrochemical cycling of NCM^{523} cathode in the in situ SSB cell, and (b) unit cell volume of NCM^{523} during cycling obtained from Rietveld refinement of the SXRD measurements.

3.6. Discussion and outlook

While many cathode coating materials have been proposed and tested in SSBs, their effectiveness varies. While a lack of coating stability will influence battery capacity, it is difficult to identify specific mechanisms and severity of degradation from capacity loss with cycling. For this reason we performed a detailed microscopy study and correlated it with predictions that can be made from first principles calculations. The remarkable breakdown of the LZrO coating and the integrity of the LBO coating at high voltages provide strong experimental confirmation of previous theory results, and are fully consistent with the idea that the high voltage limit of coating materials is determined by the extent of hybridization of the oxygen anion (*56*, *122*): The strong covalent bonding in the BO_3 and BO_4 groups in $Li_3B_{11}O_{18}$ push the oxygen states down in energy, thereby protecting them from oxidation to a much larger extent than in LZrO.

The agreement between *ab initio* computations based on a thermodynamic framework and the experimental observations indicates that even at room temperature near equilibration occurs on a very small scale. In fact, the segregation of Mn was also observed in a charged NMC-LPS composite after being heated above 300 °C. In that study, M. Tatsumisago et al. identified crystalline transition metal sulfides, such as MnS and $CoNi_2S_4$, as well as Li_3PO_4 using synchrotron X-ray diffraction (*122*). Our study in this Chapter shows that even at room temperature during normal battery operation the precursors of those crystalline degradation products already form. The oxidation of S^{2-} in thiophosphate electrolytes has also been observed in previous X-ray photoelectron spectroscopy (XPS) studies (*56*, *123*).

It should be pointed out that while the key findings presented in this Chapter are based on a SSB system, the electrochemical stability of a coating material is relevant in liquid electrolytes as well. LZrO will be prone to Li extraction under high voltage in both liquid and solid electrolyte. However, a significant difference is that in a solid-state battery the oxygen released from the LZrO decomposition can in turn exchange with the S^{2-} in the LPS surroundings, resulting in a decreased local oxygen partial pressure. Whether this low oxygen partial pressure is transmitted through the thin amorphous coating and leads to reductive instability of NCM^{523} in a solid-state battery similar to densification in a liquid cell is unclear, but our result that even when the LBO coating remains intact the NCM^{523} surface undergoes disordering similar to what is seen in liquid electrolytes, is suggestive. Understanding oxygen transport through cathode coatings should therefore be a topic of investigation.

The results in this Chapter highlight the importance of both electrochemical and chemical stability of coating materials in practical applications. An effective coating is

important to protect NCM^{523} particles from decomposition driven by its reactivity with the solid-state electrolyte. In addition to the (electro-)chemical stability and a reasonably good ionic conductivity, an effective coating should also exhibit good deformability to maintain its morphological integrity for a good contact and homogenous coverage throughout the entire cycle life. As shown in **Figure 3-12**, the amorphous LBO coating remains intact on the NCM^{523} particles after 50 cycles, allowing an effective protection of the interparticle interface. The soft nature of the lithium borate glass is expected to provide better mechanical "viscosity" on the NCM^{523} particles than a mechanically stiff and brittle coating such as $LiNbO_3$ to accommodate the anisotropic volume expansion and contraction of NCM^{523} during lithiation and delithiation (*115*, *124*). The presence of a coating also brings new considerations into the cell assembly process and the full-cell fabrication. Ball-milling and/or aggressive grinding during mixing of the coated NCM^{523} and LPS tend to break the coated secondary NCM^{523} particles. **Figure 3-17** shows a comparison of the LBO-coated NCM^{523} cathode composite after aggressive and gentle grinding. The secondary NCM^{523} particles remained undamaged after the gentle hand grinding, whereas aggressive grinding caused the secondary NCM^{523} particles to break into pieces. Given that LBO is coated on secondary particles, the broken secondary particles generate new unprotected interfaces, leading to worse electrochemical performance (**Figure 3-18**).

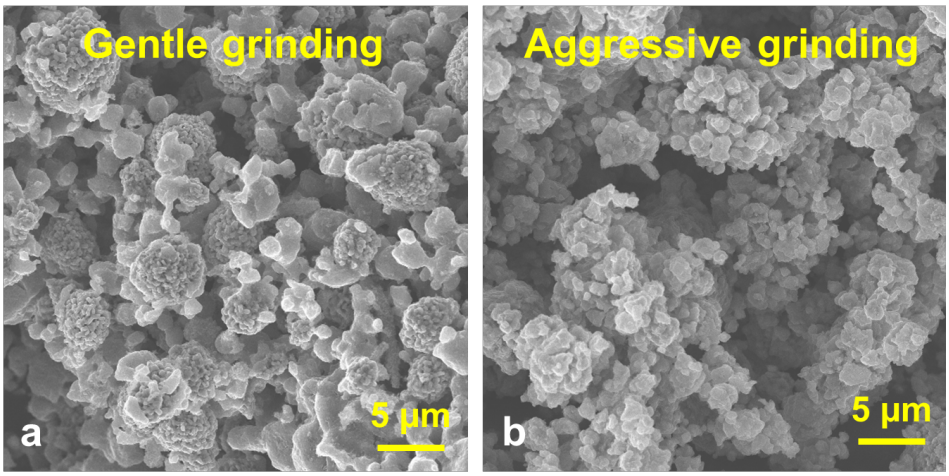


Figure 3-17 SEM images of cathode composite of LBO-coated NCM^{523}, LPS, and CNF ground using different forces. The secondary NCM^{523} particles remain intact after gentle grinding whereas aggressive grinding caused the secondary NCM^{523} particles to break into small pieces.

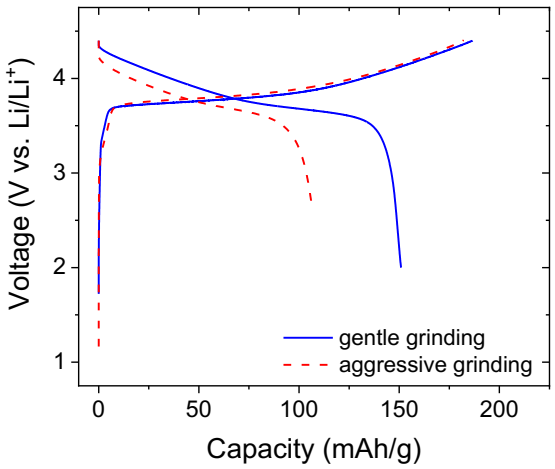


Figure 3-18 Electrochemical cycling of cathode composite of LBO-coated NCM^{523}, LPS, and CNF ground using different forces.

Although direct observations from electron microscopy have provided valuable information on the composition, nano-sized crystalline structure, and surface/interface morphology of the interfaces, isolating an intact solid interface and characterizing the spatial degradation of the amorphous electrolyte still remains challenging in SSBs. For example, although decomposition appears in a region of ~200 nm in thickness in **Figure 3-11**, the diffusion distance cannot be accurately determined as the spatial distribution of particles cannot be preserved during the sonication process of the sample preparation. Precise cutting of the buried cathode/interface cross-section is needed for better sample preparation. Combing varies microscopy technique, such as scanning transmission X-ray microscopy (STXM), together with analytical electron microscopy is also desired in future studies to probe how the electronic and chemical structure of the solid electrolyte interface evolve in dynamic electrochemical process (*125*).

Chapter 4.

Passivating interface design and construction between Na_3SbS_4 and Na metal

It is now generally accepted that for solid-state batteries to surpass traditional Li-ion cells in energy density, they will have to use metallic lithium/sodium anodes [21]. However, most solid-state electrolytes react with alkali metals, causing a continuous increase of the cell impedance. In this chapter, we employ a 'reverse design' strategy to improve the stability of the interface between a Na_3SbS_4 solid-state electrolyte and sodium metal anode. This is achieved through formation of a hydrated layer on the surface of Na_3SbS_4. Hydration forms a novel phase ($Na_3SbS_4 \cdot 8H_2O$) with reasonable sodium-ion conductivity on the surface of Na_3SbS_4. This hydrated phase partially reacts with Na metal forming NaH and Na_2O as passivating products which limit further decomposition of the solid-state electrolyte and reduce impedance growth upon cycling. *Post-operando* synchrotron X-ray depth profiling (SXDP), a to probe the interface, was used to confirm NaH and Na_2O as products of $Na_3SbS_4 \cdot 8H_2O$ in contact with metallic Na after the Na plating/stripping processes.

To further investigate the potential of this approach we evaluated the decomposition products of all the lithium and sodium hydrate compounds present in the Materials Project [33] database against lithium/sodium metal, identifying hydrates as a promising class of materials for electrolyte protection. In addition, we further extend the strategy of interface reverse design and discuss the possible pretreatment of solid-state electrolytes using other chemicals besides water.

The content of this chapter is based, often verbatim, on the following manuscripts which are published or in preparation for publication. Some results presented in this chapter were obtained by a collaborative effort. Contribution from collaborators are made explicit in relevant results.

[1] Yaosen Tian, Yingzhi Sun, Daniel C. Hannah, Gerbrand Ceder, et al. "Reactivity-Guided Interface Design in Na Metal Solid-State Batteries." Joule (2019).

4.1. Introduction

Most solid-state electrolytes are reduced by alkali metals and form reaction layers which degrade rate capability and reduce capacity over time (*60–62*, *97*, *126*). For instance, the cathodic decomposition of $Li_{10}GeP_2S_{12}$ (LGPS) is initiated by the reduction of Ge^{4+} and P^{5+} below 1.7 V vs. Li/Li^+, forming $Li_{15}Ge_4$, Li_3P, and Li_2S (*127*). The reduction of P^{5+} in Na_3PS_4 forms Na_3P and Na_2S (*126*, *127*). Any reduction of metals in the conductor can

create electronically conducting pathways which lead to further growth of the decomposition layer. Only a few conductors are thermodynamically stable against lithium metal (e.g., Li_3N, Li_3OCl) (*128*, *129*), and their limited ionic conductivity and/or poor oxidation stability limit their use in real batteries. While various coating and deposition methods have been developed to improve the wetting and/or chemical stability between garnet oxide electrolyte and Li metal (*127*, *128*), the high cost of these deposition methods make it difficult to extend these methods to a wider range of solid-state electrolytes. Such barrier layer options are also less reliable for a strongly reacting interface, for example, a Na metal/sulfide conductor interface, due to the large and inhomogeneous displacement of the electrode/electrolyte interface during cycling which will jeopardize the mechanical integrity of the barrier layer. What is required is the formation of a passivating layer formed by the reaction of the conductor with the alkali metal anode which, unlike extrinsic barrier layers, can reform whenever the passivation layer is damaged or new metal interface is formed in contact with the conductor. This passivation mechanism would be able to protect the new interface that inevitably forms when an alkali metal deposits back on the anode in the charge cycle of the battery.

A passivating interface can be engineered by introducing selected elements/compounds that react beneficially with Li/Na metals, forming electronically insulating but ionically permeable decomposition products (*129*, *130*). Similar concepts of extending the electrochemical stability window of solid-state electrolytes by forming passivating phases have been discussed in recent computational work (*107*, *131*, *132*). Once the set of insulating solids that are stable against the alkali are identified, using for example high-throughput first-principles computational tools, a solid-state conductor should be designed to decompose to these solids when in contact with the metal, leading to intrinsic passivation.

4.2. Reverse design and stability of Na/Na_3SbS_4 interface

Using first-principles methodology developed previously (described in **Appendix C**), the decomposition products of Na_3SbS_4 is predicted under different Li/Na chemical potentials[13]. The most thermodynamically favorable reactions (if any) occurring between Na_3SbS_4 and Na metal reservoir is calculated to be **Reaction (4-1)**. The predicted decomposition products of Na_3SbS_4 over the full range of Na chemical potentials are listed in **Table D-3 in Appendix D**. The large fraction of metallic Na_3Sb in **Reaction (4-1)** in the decomposition products indicates the likely formation of a percolating electronic conduction path at the interface. Therefore, continuous decomposition of bulk

[13] DFT computation of the stability of Na_3SbS_4 was performed by collaborator Dr. Daniel Hannah (LBNL, Ceder Group Postdoc).

Na_3SbS_4 is expected to occur until complete consumption of either the Na metal or Na_3SbS_4 solid-state electrolyte.

$$8\,Na + Na_3SbS_4 \rightarrow 4\,Na_2S + Na_3Sb \qquad \textbf{(4-1)}$$

The synthesis and characterization of Na_3SbS_4 are described in the **Appendix B**. **Figure 4-1** presents the SXRD pattern of the Na_3SbS_4, in which all the peaks match those of tetragonal Na_3SbS_4 (PDF 00-030-1154), indicating a pure phase of Na_3SbS_4. The structure of Na_3SbS_4 and the lattice constants obtained from Rietveld refinement shown in the inset. **Figure 4-2** presents the EIS data of Na_3SbS_4 switched by electrodes at temperatures ranging from 25 °C to 80 °C. The summarized Nyquist plots consist of semicircles corresponding to the resistance of Na_3SbS_4 and a connected vertical low-frequency tail corresponding to the capacitive behavior of the Na-ion-blocking tantalum electrodes. The conductivity of Na_3SbS_4 increased with increasing temperature. The observed Na-ion conductivity was approximately 0.4 mS/cm at 25 °C. The Arrhenius plot for total Na-ion conductivity obtained from EIS analysis is shown in **Figure 4-3**. The activation energy was determined to be 0.18 eV.

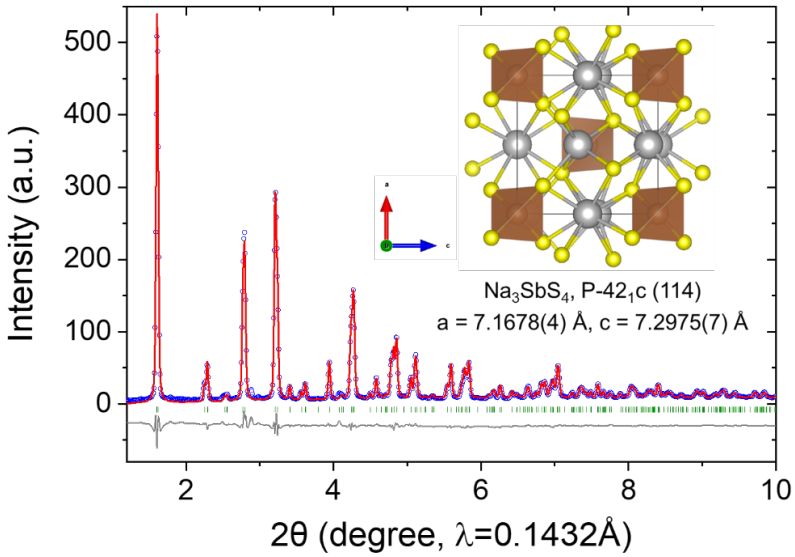


Figure 4-1 Synchrotron X-ray diffraction pattern and Rietveld refinement of the Na_3SbS_4. The diffraction peaks corresponding to Na_3SbS_4 are marked with green tick marks. The blue dots represent the observed intensities, and the red and dark grey curves represent the calculated intensities and intensity difference between the observation and the refinement fitting, respectively.

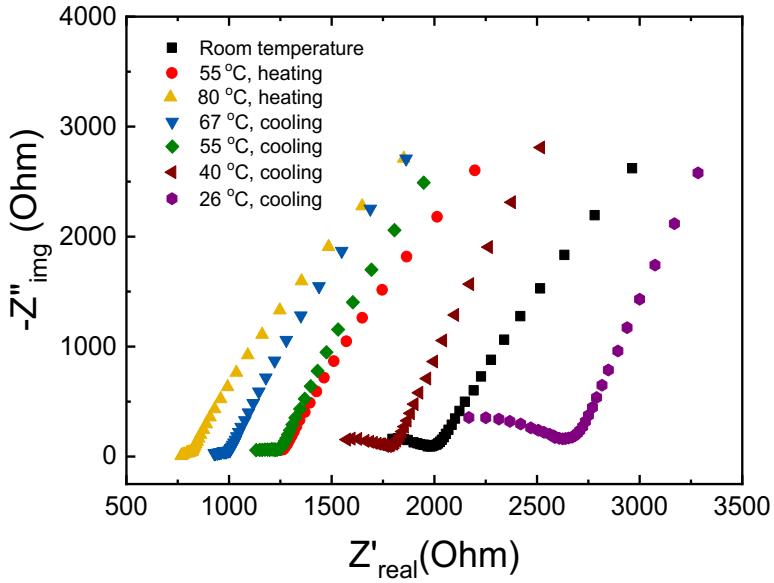


Figure 4-2 EIS data of Na_3SbS_4 switched by electrodes at temperatures ranging from 25 °C to 80 °C (including both the heating and the cooling processes)

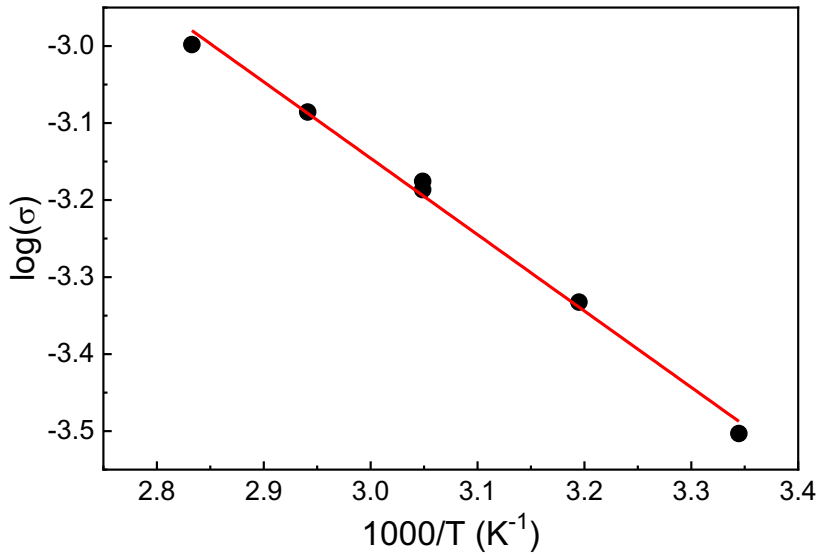


Figure 4-3 Arrhenius plot for total Na-ion conductivity obtained from EIS analysis. The activation energy was determined to be 0.18 eV

To evaluate the compatibility between Na_3SbS_4 and Na metal experimentally, a symmetric $Na/Na_3SbS_4/Na$ cell was cycled at a constant current (0.1 mA cm^{-2}). The

results are fully consistent with the theoretical predictions discussed above. As shown in **Figure 4-4**, the Na plating/striping voltage continuously increases from an initial value of 0.13 V to 0.67 V after 25 h of cycling, suggesting increasing polarization due to the unstable Na/Na_3SbS_4 interface. Na_2S could be identified as one of the decomposition products after cycling of the symmetric cell using synchrotron X-ray diffraction (SXRD) performed at beam line 11-ID-B at the Advanced Photon Source (APS) at Argonne National Laboratory (**Figure 4-5**), consistent with the theoretical prediction of **Reaction (4-1)**. The same products as those predicted in **Reaction (4-1)** were also identified using X-ray photoelectron spectroscopy in a recent work (*131*). A digital photograph and scanning electron microscopy (SEM) images of the Na/Na_3SbS_4 interface after 25 cycles are presented in **Figure 4-6.**

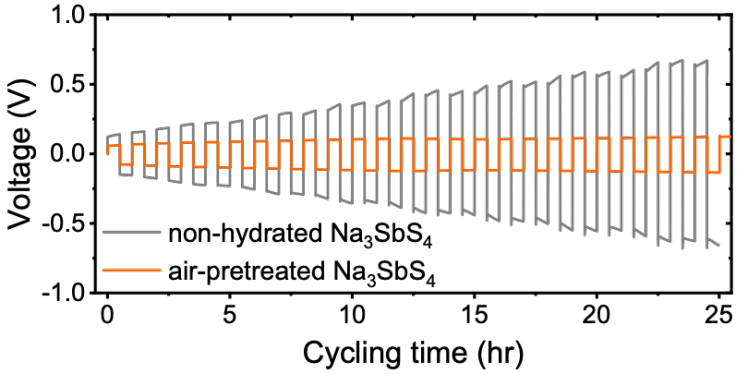


Figure 4-4 Galvanostatic cycling of Na/Na_3SbS_4/Na symmetric cells with (orange) and without (grey) surface hydration pretreatment at a current density of 0.1 mA cm^{-2}

Based on our previous first-principles screening results on the stability window of most Na-containing compounds, NaH and Na_2O are predicted to be thermodynamically stable upon contact with Na metal. Both compounds have been reported to exhibit high ionic conductivity and electronic resistivity (*107*, *132*, *133*), making them desirable for interface passivation. To bring in the H and O needed to form NaH and Na_2O at the interface, Na_3SbS_4 was partially hydrated. As reported in the literature (*42*, *134*), Na_3SbS_4 is stable in a dry air atmosphere, whereas a fully hydrated phase, $Na_3SbS_4 \cdot 9H_2O$, can be generated in the presence of moisture. The reactivity of $Na_3SbS_4 \cdot 9H_2O$ in contact with the Na reservoir was evaluated for the full range of Na chemical potentials, and the results are summarized in **Table D-4** in **Appendix D**. The most favorable reaction at 0 V vs. Na/Na^+ is determined to be:

$$44\,Na + Na_3SbS_4 \cdot 9H_2O \rightarrow 4\,Na_2S + Na_3Sb + 18\,NaH + 9\,Na_2O \qquad \textbf{(4-2)}$$

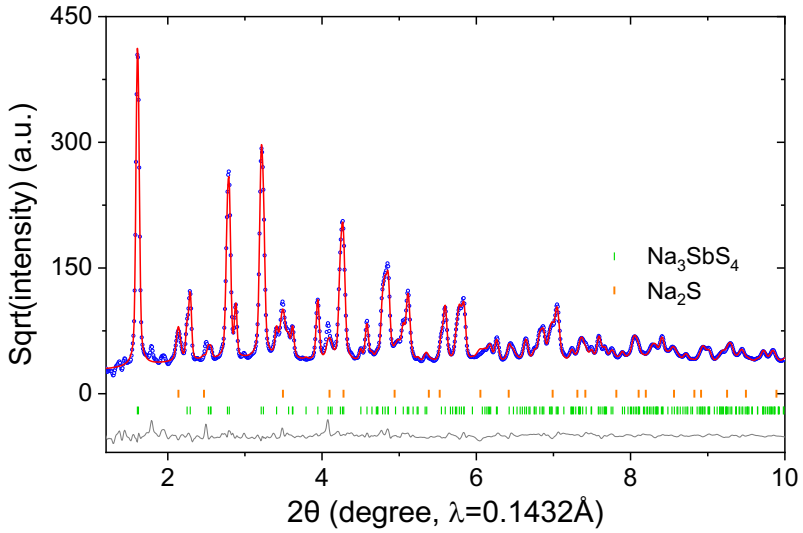


Figure 4-5 SXRD pattern and Rietveld refinement of Na_3SbS_4/Na interface products. The blue dots represent the observed intensities, and the red and dark grey curves represent the calculated intensities and intensity difference between the observation and refinement fitting, respectively. The tick marks indicate the peak positions for Na_3SbS_4 (green) and Na_2S (orange).

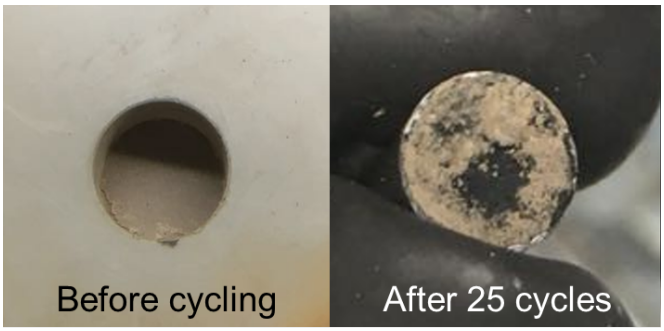


Figure 4-6 Comparison of surface of solid-state electrolyte pellet before and after contact with Na metal and electrochemistry cycling. The left photograph displays the Na_3SbS_4 pellet before being attached to Na metal. The right photograph displays the Na_3SbS_4/Na interface after 25 cycles; the black interfacial products can be observed.

As shown in **Reaction (4-2)**, Na_2O and NaH will be generated when $Na_3SbS_4 \cdot 9H_2O$ is in contact with Na metal. As opposed to the large fraction of Na_3Sb generated in **Reaction (4-1)**, the fraction of the electron conducting phase is greatly decreased to 3 mol.% in **Reaction (4-2)**, which can result in substantially improved interface stability.

A symmetric cell using a surface-hydrated Na_3SbS_4 pellet as the solid-state electrolyte was constructed to experimentally examine the effect of electrolyte hydration on the stability of the Na/Na_3SbS_4 interface. The as-prepared Na_3SbS_4 pellet was exposed to ambient air at a humidity of approximately 68% for 5 min before being sandwiched by metallic Na foils. The cells were assembled using otherwise identical procedures, and Na_3SbS_4 from the same batch was used to maximize consistency. The changes in the surface morphology of the Na_3SbS_4 pellet during the hydration process can be observed in the SEM images presented in **Figure 4-7**. **Figure 4-8** presents schematic illustrations of the Na metal/Na_3SbS_4 interface with and without the hydrated layer. As observed in **Figure 4-4**, a substantially smaller voltage increase occurred after cycling for the surface-hydrated Na_3SbS_4 than for its non-hydrated counterpart, which indicates improved interfacial stability and effective protection provided by the hydrate protective layer.

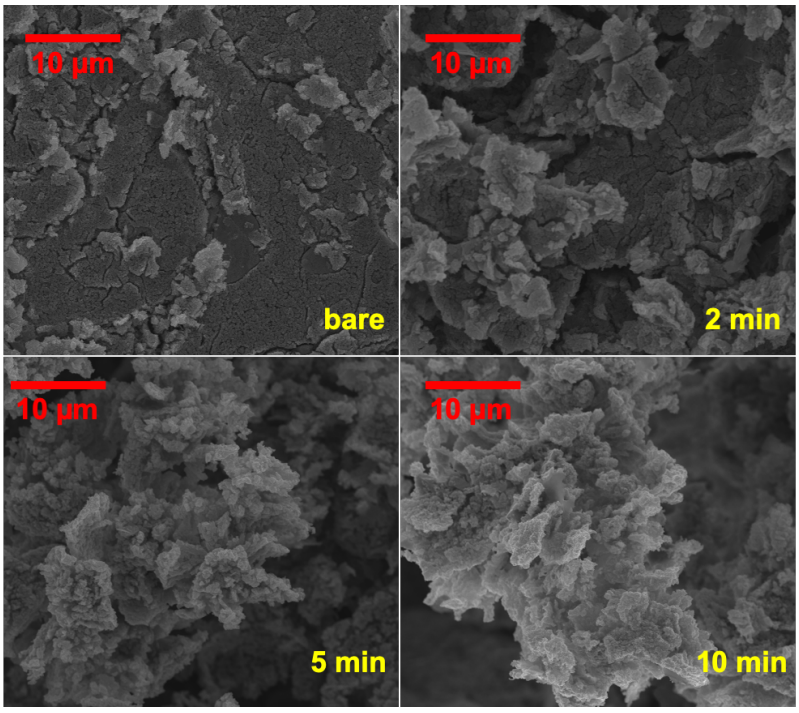


Figure 4-7 SEM images of the surface of Na_3SbS_4 pellet after air exposure for different durations.

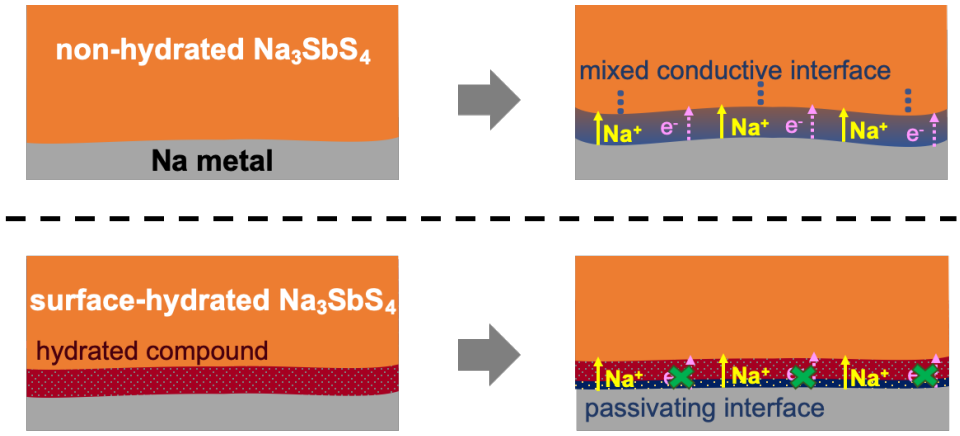


Figure 4-8 Schematic illustration of solid electrolyte/Na metal interface before (left) and after (right) electrochemical cycling. A mixed conductive interface layer grew upon cycling of the non-hydrated Na_3SbS_4 (top), whereas a passivating interface was formed on the hydrated compound of the surface-hydrated Na_3SbS_4 (bottom).

4.3. Electrolyte hydration process and discovery of $Na_3SbS_4 \cdot 8H_2O$

A strong correlation was observed between the (electro)chemical properties of the surface-hydrated Na_3SbS_4 and the air exposure time, with an optimal exposure time of 10 min (**Figure 4-9**). For the cells using Na_3SbS_4 exposed to air for longer than 10 min, the voltage before cycling increased (shown as the grey dash line), suggesting an increase in the overall cell impedance. The voltage growth after 25 cycles (shown as the grid-pattern-filled area) in these cells was similar to that observed in the cell with 10 min of air exposure, indicating similar stability against Na metal. This finding motivated us to determine whether different phases were produced during the air exposure or whether this correlation between exposure time and electrochemical performance was simply due to the expected change in the interface morphology against exposure time (e.g., increase of thickness).

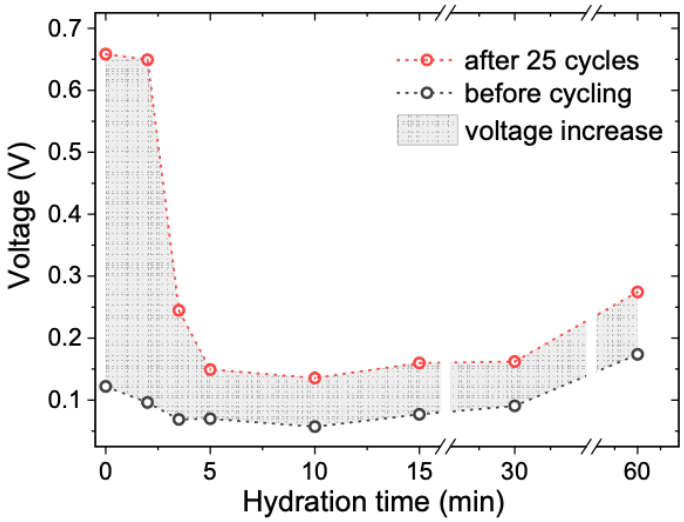


Figure 4-9 Voltage of Na/Na_3SbS_4/Na symmetric cells after different surface hydration pretreatment durations before (grey) and after (red) 25 cycles (0 min of surface pretreatment indicates the use of bare Na_3SbS_4 as the solid electrolyte). The grid-pattern-filled area represents the voltage increase of each symmetric cell upon cycling.

To monitor the phase transformation of Na_3SbS_4 during the hydration process in ambient air, SXRD patterns were collected from a Na_3SbS_4 powder sample over 120 min of air exposure (**Figure 4-10**). A new phase (the visible peaks marked by the red-colored dots) appears after 2 min of air exposure, together with Na_3SbS_4 (allowed peaks marked with blue-colored tick marks). Unexpectedly, the newly produced peaks do not correspond to those for the phase. The fully hydrated phase $Na_3SbS_4 \cdot 9H_2O$ does not appear until approximately 30 min of air exposure. Because the hydration and dehydration of Na_3SbS_4 have been reported to be reversible (*42*, *134*), the new phase formed during the hydration of Na_3SbS_4 is likely an intermediate hydrate phase containing less crystal water. The formation time of the intermediate hydrate phase corresponds to the optimal pretreatment time of the solid-state electrolyte, indicating that the improved cathodic stability of the surface-treated Na_3SbS_4 is due to the formation of this intermediate hydrate phase rather than the fully hydrated one.

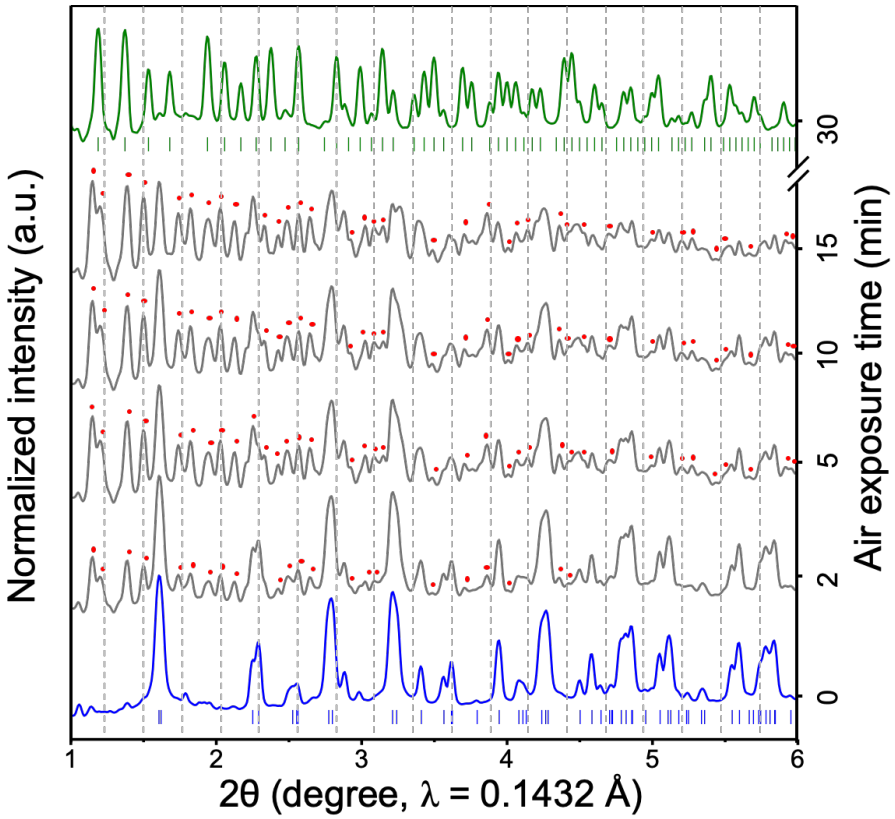


Figure 4-10 SXRD patterns of Na_3SbS_4 after different durations of air exposure, with the tick marks indicating the peak positions for Na_3SbS_4 (blue) and $Na_3SbS_4{\cdot}9H_2O$ (green). The visible peaks corresponding to $Na_3SbS_4{\cdot}8H_2O$ are marked by dots.

We attempted to determine the composition and structure of this intermediate hydrate phase. *Ab initio* structure determination from powder diffraction data is challenging, which was further complicated by the presence of more than two phases and no prior knowledge of the phase composition, making the commonly employed structural solution approaches (e.g., simulated annealing, direct method) infeasible. Instead, we proposed structures by substituting atoms in all hydrated compounds associated with Na_3AX_4 (A = P, As, Sb; X = S, Se) in the Inorganic Crystal Structure Database (ICSD), and these structures were then tested against the diffraction data using Rietveld refinements. The intermediate hydrate compound (**Figure 4-11a**) was identified as $Na_3SbS_4{\cdot}8H_2O$, which was obtained by substituting As for Sb and D for H in $Na_3AsS_4{\cdot}8D_2O$ (*135*, *136*) as shown in **Figure 4-11b**. The structural parameters of the as-prepared $Na_3SbS_4{\cdot}8H_2O$ determined from the Rietveld refinement of the SXRD data are listed in **Tables 4-1**. A detailed structural description is provided in **Appendix F**. Using density functional theory (DFT) calculations, the energy of the monoclinic ($P2_1/c$, No. 14) $Na_3SbS_4{\cdot}8H_2O$ structure was calculated to be only 11 meV/atom above the compositional convex hull. This is well below most synthesizable low-energy metastable

compounds (*137*), indicates that the structure is likely stabilized by entropy at room temperature. However, our efforts to isolate $Na_3SbS_4 \cdot 8H_2O$ as a single phase were unsuccessful, which may suggest that this phase is only stable within a very narrow range of H_2O partial pressure.

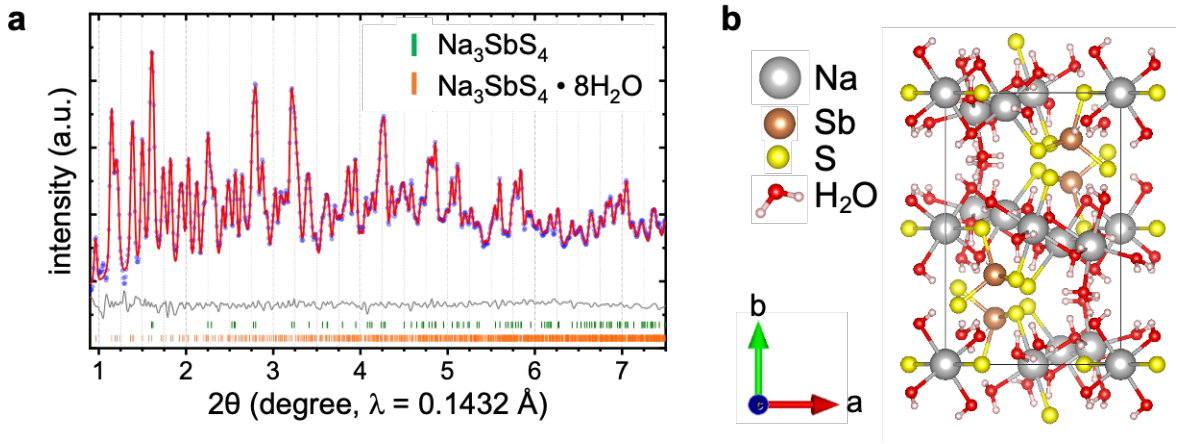


Figure 4-11 (a) SXRD pattern and Rietveld refinement of Na_3SbS_4 after 10 min of air exposure. The blue dots represent the observed intensities, and the red and dark grey curves represent the calculated intensities and intensity difference between the observation and refinement fitting, respectively. The tick marks indicate the peak positions for Na_3SbS_4 (green) and $Na_3SbS_4 \cdot 8H_2O$ (orange). **(b)** Crystal structure viewed along the [001] direction of $Na_3SbS_4 \cdot 8H_2O$.

Table 4-1 Crystallographic data for $Na_3SbS_4 \cdot 8H_2O$ based on Rietveld refinement of the synchrotron XRD data.

Crystal system	*Monoclinic*
Space group	$P12_1/c1$ (#14)
Lattice parameters	a = 8.7460(9) Å b= 13.1683(1) Å c= 13.9058(1) Å β= 103.283(9)°
Cell volume	1558.7(3) $Å^3$
Calc. density	1.97333 g/cm^3

To understand the Na-ion transport mechanisms in $Na_3SbS_4 \cdot 8H_2O$ and $Na_3SbS_4 \cdot 9H_2O$, we performed nudged elastic band (NEB) calculations of Na-vacancy migration barriers of both structures[14]. The vacancy migration barrier of $Na_3SbS_4 \cdot 8H_2O$ is calculated to be 502 meV (**Figure 4-12a)** along the [100] direction, as shown in **Figure 4-12b**. This migration barrier is comparable to that of LIPON reported in previous studies (*138*, *139*), suggesting reasonable Na-ion conductivity of $Na_3SbS_4 \cdot 8H_2O$. Detailed descriptions of the Na-ion diffusion channels and transport mechanisms are presented in **Appendix F**. Similarly, the vacancy migration barrier of $Na_3SbS_4 \cdot 9H_2O$ is calculated to be 920 meV (**Figure 4-12a)** along the [010] direction, as shown in **Figure 4-12c**, which is consistent with previous reports of the low Na-ion conductivity of the structure (*123*, *138*). The much higher migration barrier in $Na_3SbS_4 \cdot 9H_2O$ precludes any substantial Na mobility through it and indicates the importance of a relatively short hydration process to reach the $Na_3SbS_4 \cdot 8H_2O$ but not the $Na_3SbS_4 \cdot 9H_2O$ phase.

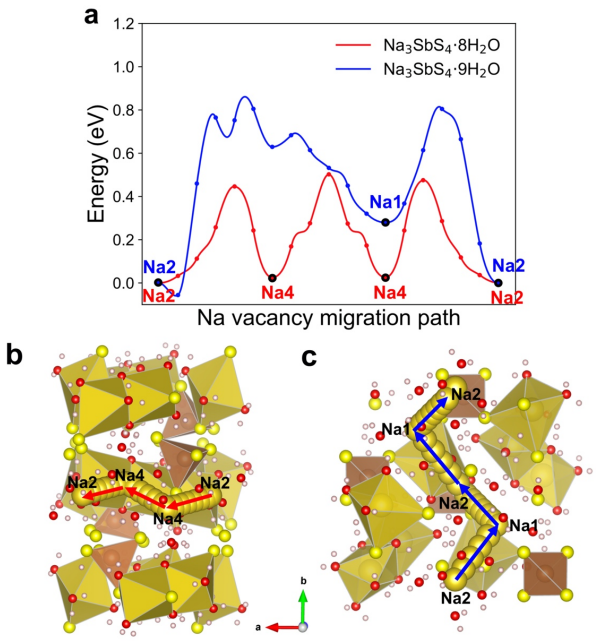


Figure 4-12 Na vacancy migration barriers and transport mechanism in $Na_3SbS_4 \cdot 8H_2O$ and $Na_3SbS_4 \cdot 9H_2O$. **(a)** Na vacancy migration energy along the minimal energy pathway. **(b-c)** Na vacancy migration pathway with minimal percolation barrier in $Na_3SbS_4 \cdot 8H_2O$ along the [100] direction **(b)** and in$Na_3SbS_4 \cdot 9H_2O$ along the [010] direction **(c)**. $Na(H_2O,S)_6$ octahedra and SbS_4 tetrahedra are colored in yellow and brown, respectively. The Na transport channel is represented by the hopping Na atoms (labeled consistently with **Appendix F**) and the red or blue arrows.

[14] NEB computations of the Na-ion mobility in $Na_3SbS_4 \cdot 8H_2O$ and $Na_3SbS_4 \cdot 9H_2O$ were performed by collaborator Mr. Yihan Xiao (UC Berkeley, Ceder Group Graduate Student).

4.4. Interface stabilization mechanism and characterization of interface products

Based on the findings discussed above, we can rationalize the complex interface chemistry by which the surface-hydrated Na_3SbS_4 improves the interfacial stability against Na metal. Upon air exposure for an optimal duration, $Na_3SbS_4 \cdot 8H_2O$ is formed instead of the fully hydrated phase on the surface of Na_3SbS_4. The reaction between $Na_3SbS_4 \cdot 8H_2O$ and Na metal can be evaluated using DFT and is found to be similar to that of the fully hydrated phase, leading to the formation of the following interface:

$$40\,Na + Na_3SbS_4 \cdot 8H_2O \rightarrow 4\,Na_2S + Na_3Sb + 16\,NaH + 8\,Na_2O \qquad \textbf{(4-3)}$$

The interfacial decomposition products were experimentally determined using a spatially resolved *post-operando* SXDP experiment. The experiment was performed on a symmetric $Na/Na_3SbS_4/Na$ cell at beam line 11-ID-B at APS using the radially accessible tubular *in situ* X-ray (RATIX) cell adapted for X-ray transmission(*121*). The cell was cycled at a constant current (0.1 mA/cm^2) for 25 h of the Na plating/stripping processes. The post-cycled cell was oriented vertically, with the X-ray beam transmitted through the cell horizontally. To achieve better mapping resolution, the size of the beam was reduced to 50 μm in the vertical direction along the cell. Diffraction patterns were obtained consecutively at 13 positions between two current collectors. Details of the experimental set-up are provided in the Methods section. **Figure 4-13a** displays SXRD patterns collected at different positions along the vertical direction of the Na/surface-hydrated Na_3SbS_4/Na symmetric cell. $Na_3SbS_4 \cdot 8H_2O$ is observed in three SXRD patterns next to Na metal (i.e., the patterns colored in red and yellow in **Figure 4-13a**). All the Bragg reflections from the bulk solid-state electrolyte region can be indexed to Na_3SbS_4 (e.g., the bolded pattern No. 4 colored in grey in **Figure 4-13a**), suggesting perfect sealing of the cell. Decomposition products, such as NaH and Na_2O, together with $Na_3SbS_4 \cdot 8H_2O$ were identified in the two layers closest to the Na metal (e.g., the bolded patterns No. 1 colored in red in **Figure 4-13**. The third closest layer (e.g., the bolded pattern No. 11 colored in yellow in **Figure 4-13a**) consisted of a two-phase mixture of $Na_3SbS_4 \cdot 8H_2O$ and Na_3SbS_4. The detection of NaH and Na_2O agrees well with our computational prediction for the reaction between Na metal and $Na_3SbS_4 \cdot 8H_2O$ in **Reaction (4-3)**. The presence of Na metal was observed after the cell was disassembled. These results confirm the protection of Na metal by hydration of the electrolyte.

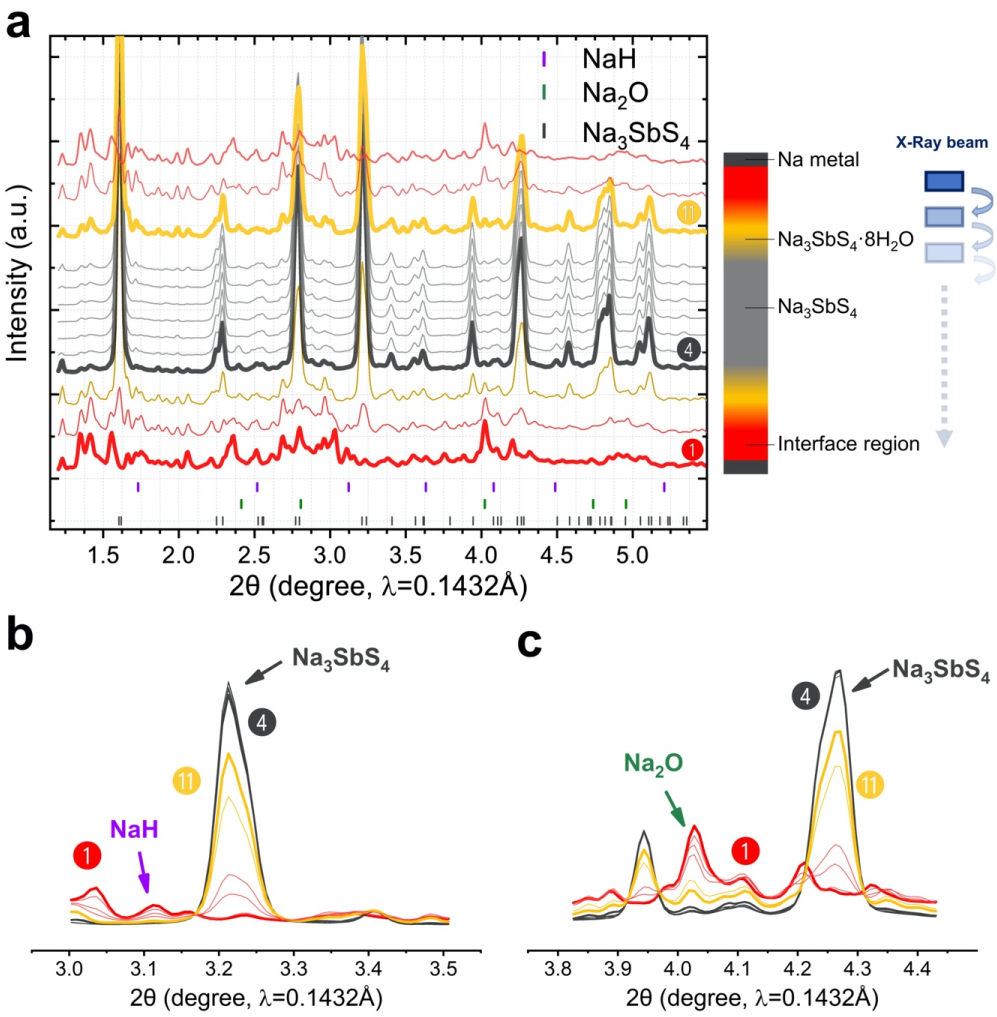


Figure 4-13 Spatially resolved *post-operando* SXRD profiles of Na/Na_3SbS_4/Na symmetric cell with surface hydrate coating. **(a)** SXRD depth profiling of symmetric cell along the vertical axis of the cell. Each pattern corresponds to one layer of the schematic illustration on the right marked by multiple colors. The three bolded patterns mark the three region boundaries in the symmetric cell. **(b-c)** Enlargement of XRD profiles from 3.0°-3.5° **(b)** and 3.8°-4.5° **(c)**. Visible peaks for NaH, Na_2O, and Na_3SbS_4 are marked by arrows.

4.5. Discussion

Most solid conductors are not stable against the strong reduction potential of alkali metal anodes and require the use of barrier layers or accidental passivation. The best passivation is one that is designed to give ionically conducting products from the reaction of the conductor with the alkali metal. This "built-in" passivation guarantees that even freshly generated interfaces are passivated, in contrast with externally applied barrier layers. In our example, we stabilized the interface between the sulfide conductor Na_3SbS_4 and Na metal by the formation of NaH and Na_2O through air exposure of the solid electrolyte pellet for a certain duration. The fast phase transformation between Na_3SbS_4, $Na_3SbS_4 \cdot 8H_2O$, and $Na_3SbS_4 \cdot 9H_2O$ in ambient air at room temperature suggests the fast reaction kinetics of water uptake and release, which may have led to the preferred generation of NaH and Na_2O over other products from the reduction of Sb when the hydrated compounds contacted Na metal. In fact, the stability between Na_3SbS_4 and Na metal might have been achieved accidentally without realizing the effect of hydrate protection. In contrast to other observations and theoretical predictions (*125*, *140*), the interface between Na_3SbS_4 and Na metal was reported to be stable in one previous study (*140*) in which Na_3SbS_4 was synthesized by heating $Na_3SbS_4 \cdot 9H_2O$. The reported thermogravimetric analysis results during the dehydration process indicated the presence of residual crystal water, which may explain the observed compatibility.

Hydrates have broadened the materials horizons of battery research (*126*, *141*), in particular as protective layers for metal anodes. To broaden the impact of the work presented in this chapter in metal-based solid-state batteries, we evaluated the reactions between all the unique Li/Na-containing hydrated compounds present in the Materials Project database and Li/Na metal[15]. All 32 of the unique Na-based hydrated compounds reacted with Na at 0 V (i.e., complete reduction) to form NaH, and 25 out of 32 reacted with Na to form Na_2O. In addition, all 37 of the unique Li-based hydrated compounds reacted with Li to form both LiH and Li_2O at 0 V. These predicted reactions are summarized in **Tables D-5** and **D-6 in Appendix D**. This suggests hydrates as promising materials for metal electrode protection in solid-state batteries, which, in certain cases, can be formed *in situ* simply through air exposure.

Furthermore, we highlight the importance of reverse interface design in this chapter. Rather than designing conductors for which reactivity with the electrodes is left to chance, reaction to passivating products should be designed from the start. Based on our high-throughput screening results on the decomposition products of multiple Na-ion conductors, we used hydrated compounds as a chemical initiator to beneficially react

[15] DFT computations of the reaction between hydrated compounds and Li/Na metal were performed by collaborator Dr. Daniel Hannah (LBNL, Ceder Group Postdoc).

with the alkali metal to construct the designed interface. The reaction between the hydrated compound and metallic electrode introduces preferred passivating products at the interface (i.e., NaH and Na_2O, as demonstrated in this chapter), and reduces the fraction of electronically conducting phases (i.e., Na_3Sb) that cause continuous interface growth. Using the proposed general strategy of interface reverse design, pretreatment using other chemicals can be performed to regulate the metal/electrolyte interface. For example, Li_2S is another passivating product that can be possibly introduced in the interface. Gas processing of sulfide-based conductors using SO_2 can produce a sulfur-rich layer on the electrolyte surface (such as the generation of S or Li_4GeS_4 in **reactions (4-4)** and **(4-5)** calculated by DFT), which may serve as initiators to introduce Li_2S at the metal/electrolyte interface. Interestingly, several gases (N_2, O_2, CO_2, SO_2) were considered for use as the pretreatment gas in a Li-metal liquid cell (*126*, *141*), and among these gases, SO_2 was determined to be the most effective gas for the construction of a thin passivation layer(*120*, *142–145*).

$$2\,SO_2 + Li_3PS_4 \rightarrow Li_3PO_4 + 6\,S \qquad \textbf{(4-4)}$$

$$2\,SO_2 + 0.5\,Li_{10}Ge(PS_6)_2 \rightarrow Li_3PO_4 + 0.5\,Li_4GeS_4 + 6\,S \qquad \textbf{(4-5)}$$

Finally, together with the phase fraction of each interface component, the spatial distribution of different components is equally important in determining interface transport properties. Developing of a rational strategy toward SEI morphology optimization in solid-state batteries has been hindered by the nanoscale thickness of this interfacial layer, which poses significant characterization challenges. *Ex situ* X-ray and/or neutron total scattering techniques can provide useful information regarding the interface decomposition products but require physical separation of the interfacial layer followed by powder grinding in sample preparation, which may lead to further reactions. **Figure 4-14** compares the *ex situ* and *post-operando* SXRD patterns of the Na/Na_3SbS_4·$8H_2O$ interface. Na_3SbS_4·$8H_2O$, NaH, and Na_2O can be clearly identified at the interface in the *post-operando* SXRD pattern but are not detectable in the *ex situ* diffraction pattern because of the presence of excess Na_3SbS_4 from the bulk electrolyte and the generation of Na_2S from the further reaction of Na metal and Na_3SbS_4 during grinding. These results suggest that non-destructive methods such as *in situ* depth-profiling experiments can provide more accurate information about the composition and spatial distribution of interfacial reaction products than *ex situ* experiments. We believe that future work using depth-profiling experiments and tomography (*146*) techniques will deepen our understanding of the morphological evolution of the interface, which is crucial for solid-state battery research.

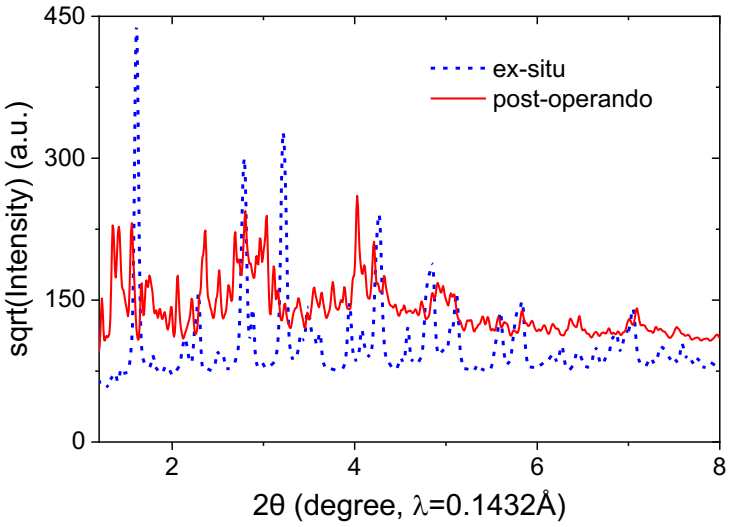


Figure 4-14 Comparison of *ex situ* and *post-operando* synchrotron XRD patterns of $Na/Na_3SbS_4 \cdot 8H_2O$ interface. The blue dashed and red solid curves represent the measured diffraction patterns obtained from the *ex situ* and *post-operando* experiments, respectively. $Na_3SbS_4 \cdot 8H_2O$, NaH, and Na_2O are identified at the interface in the *post-operando* XRD pattern, and excess Na_3SbS_4 and Na_2S are identified in the *ex situ* XRD pattern.

Chapter 5.

Conclusion remarks

In this thesis, I have proposed, implemented, and validated characterization tools of accurate evaluation of interfacial stability and construction of stable interfaces in solid-state batteries. I have sought to analyze interface degradation and develop stable or passivating interfaces between electrodes and solid electrolyte with combination of first-principles computations, electrochemistry and multiple structural and chemical characterization techniques.

In **Chapter 2**, we presented a methodology that combines computational and experimental tools to investigate the compatibility between solid electrolytes and cathodes. Relatively simple and rapid XRD and SDT experiments were proven to be very effective in describing the interfacial reactions between electrolytes and electrodes. By applying the method to the Na solid-state system, we were able to determine the voltage windows of the electrolytes (both the thermodynamic-driven lower bound and kinetic-stabilized upper bound), understand the thermodynamics and kinetics behind the reactions between incompatible electrolyte/electrode pairs. These data provide crucial information for new solid electrolyte design and electrolyte/electrode interfacial modification and serve as an essential guide for integrating these components. The methodology and insights obtained in this study can also be applied to other electrochemical systems of interest, such as Li-ion solid-state batteries.

In **Chapter 3**, we combined *ab initio* computation with electrochemical and electron microscopy investigations to identify lithium borate LBO as a promising coating for the thiophosphate system and explain its superior performance. Both DFT calculation and microscopic characterization suggest excellent chemical and oxidation stability of the LBO coating in an NCM^{523}–LPS cathode composite, effectively suppressing interfacial reactions, providing significantly higher capacity and enhanced capacity retention in a full-cell SSB. Direct observations from TEM and STEM reveal that LZrO is not stable at high voltages and is not effective for protecting the NCM^{523} cathode. We also employ *in situ* synchrotron XRD to study the first cycle capacity loss of solid electrolyte decomposition in a full-cell SSB. This chapter elucidates the critical parameters required for cathode coatings and provides insight into the design of coatings for high-voltage SSBs.

In **Chapter 4**, an effective strategy for the reverse design of the metal/electrolyte interface in solid-state batteries based on first-principles calculations of passivating

reaction products was presented. Using this strategy, the strongly reacting interface between Na_3SbS_4 and Na metal was partially stabilized via electrolyte hydration achieved by exposing the electrolyte pellet to ambient air. This rapid and simple air treatment greatly improved the stability of the Na_3SbS_4 electrolyte-Na metal interface upon electrochemical cycling. The formation of a newly discovered hydrate phase, $Na_3SbS_4 \cdot 8H_2O$, led to the generation of desired passivating products (i.e., NaH and Na_2O) at the interface, which suppressed the electrolyte decomposition. The spatially resolved multilayered phase distribution in the Na metal symmetric cell was characterized using non-destructive *post-operando* SXDP, providing valuable information about the metal-electrolyte interface that was consistent with our theoretical predictions. The work in this chapter identifies hydrates as a promising class of materials for stabilization of the metal-electrolyte interface of solid-state batteries, together with the interface reverse design strategy, providing a new path for the discovery of a wide range of other potential passivating products.

With major advancements in ionic conductivity, the chemical stability of various interfaces in SSBs has become the main concern for stable cycling of SSBs. Although the search for a promising SE with good conductivity ($\sigma > 10^{-4}$ S cm^{-1}) and both good cathodic (stable with Li metal) and anodic (> 4.5 V) stabilities remains ongoing, other methods have been used to alleviate these interfacial issues. Cathode coatings have been shown to stabilize the cathode–SE interface and allow the use of SEs beyond their intrinsic stability windows. However, the SE decomposition at the electron source could still be detrimental for the long-term cyclability of SSBs. Li metal dendrite formation is another challenge for high-energy-density SSBs. The practical issues associated with SSB fabrication mainly arise from the difficulty in making intimate particle–particle contact. For the composite electrode, forming an intimate interface between the SE and active material without a side reaction could be challenging, particularly for mechanically hard SEs such as garnet oxides. To reduce the separator thickness, binders could be used to improve the mechanical stability of the thin SE separator. Although the processing conditions will vary depending on the mechanical properties of the SE used, significant modifications to the current LIB production process are expected for SSB fabrication.

Appendix A. Energy density estimation for LIBs and SSBs

In the cell model applied in **Figure 1-2**, the following assumptions were made to ensure that the only variables affecting the resulting cell-level energy densities for LIBs, and Li metal SSBs were active-material inputs such as the capacity, voltage, and density for the electrode of interest. The following electrolyte, separator, and current collector inputs were derived from values used in Argonne National Laboratory's Battery Performance and Cost (BatPac) model for Li-ion batteries[1] listed as follows:

Parameter for LIBs

15-μm separator with 50 vol% porosity and density of 0.46 g cm^{-3}, electrolyte density of 1.2 g cm^{-3}, 10-μm copper anode current collector, and 15-μm aluminum cathode current collector. The positive electrode had a thickness of 100 μm with 89 wt% Li-ion cathode active material, 6 wt% conductive additives with a density of 1.825 g cm^{-3}, 5 wt% binder with a density of 1.77 g cm^{-3}, and 32 vol% porosity. A capacity ratio of 1.25 with excess anode loading was set to determine the anode thickness, and 95 wt% anode active material and 5 wt% binder with 34 vol% porosity. A graphite anode was applied in all LIBs with a gravimetric capacity of 360 Ah kg^{-1}, average voltage of 0.05 V vs. Li/Li^+, and density of 2.24 g cm^{-3}.

Parameter for Li metal SSBs

20-μm Li_2S-P_2S solid electrolyte separator with 5 vol% porosity and density of 1.87 g cm^{-3}, 10-μm copper anode current collector, and 15-μm aluminum cathode current collector. The positive electrode had a thickness of 100 μm with Li-ion cathode with 80-83 wt% cathode active material, 6 wt% conductive additives with a density of 1.825 g cm^{-3}, 11-14 wt% solid electrolyte, and 10 vol% porosity. A Li metal anode is used in all SSBs with a gravimetric capacity of 3860 Ah kg^{-1}, average voltage of 0 V vs. Li/Li^+, and density of 0.59 g cm^{-3}. A Li utilization of 0.80 was set to determine the anode thickness, and 100 wt% anode active material with 0 vol% porosity.

Appendix B. Experiment methods

Appendix B-1. Inorganic material synthesis

Synthesis of NaMO$_2$ (M=Cr, Mn, Fe, Co, Ni)

All the NaMO$_2$ cathode materials in **Chapter 2** were prepared by solid-state synthesis. Stoichiometric amounts of the precursors (typically ~1.0 g) were mixed by ball milling (tungsten carbide ball mill jar, Spex 8000M mixer/mill) and pressed into 1/2-in pellets. The pellets were then placed in alumina boats and heated at a rate of 10°C/min in appropriate atmospheres until the reaction was completed. The corresponding precursors and heating conditions are listed in **Table B-1**. The samples (except $NaMnO_2$) were cooled to 150°C at a rate of 30°C/min and immediately transferred to an Ar glovebox. $NaMnO_2$ was quenched to RT after synthesis and then immediately transferred to an Ar glovebox.

Table B-1 Synthesis conditions of NaMO$_2$ cathode materials

	Precursors	Heating Condition
$NaCrO_2$	Cr_2O_3 (Sigma–Aldrich, >99.5%), Na_2CO_3 (Sigma–Aldrich, 99%)	900°C in Ar (with 2% H_2) for 10 h
$NaMnO_2$	Mn_2O_3 (Sigma–Aldrich, >99.5%), Na_2CO_3 (Sigma–Aldrich, 99%)	700°C in air for 9 h
$NaFeO_2$	Fe_2O_3 (Sigma–Aldrich, >99%), Na_2O_2 (Sigma–Aldrich, 97%)	600°C in air for 20 h
$NaCoO_2$	Co_3O_4 (Sigma–Aldrich, 99.5%), Na_2O_2 (Sigma–Aldrich, 97%)	550°C in O_2 for 16 h
$NaNiO_2$	NiO (Sigma–Aldrich, 99%), Na_2O_2 (Sigma–Aldrich, 97%)	650°C in O_2 for 10 h

Synthesis of chemically desodiated $Na_{0.5}MO_2$

Synthesized pristine $NaMO_2$ powder, over-stoichiometric (ten-fold excess) iodine (GSS, 99.8%, beads), and ~15 mL of acetonitrile (Sigma–Aldrich, 99.8%, anhydrous) were placed in a glass sample vial containing an octagonal magnetic stirring bar. After being wrapped with Al foil to prevent light exposure, the sealed vial was placed on a stirrer and stirred at a speed of 1200 rpm in a Ar glovebox for 4 days. The solution was then centrifuged at 5000 rpm for 7 min. The solid residue was separated from the supernatant and washed with acetonitrile ~6 times until no iodine was observed in the solvent. After drying in the vacuum chamber of the Ar glovebox for ~12 h, the final product was transferred into the glovebox and ground into a powder for further characterization.

Synthesis of Na_3PS_4 and Na_3PSe_4

Na_3PX_4 (X = S, Se) in **Chapter 2** was synthesized using a solid-state sintering method. Na_2X (Alfa Aesar, 99.8%), red phosphorus (Sigma–Aldrich, ≥99.99% trace metal basis), and S/Se (Sigma–Aldrich, 99.99% trace metal basis) powder were mixed in a stoichiometric ratio in an Ar-filled glovebox. The mixture of the three compounds was then loaded into a BN tube (3-mm inner diameter and 4-mm outer diameter). The tube was wrapped with Al foil and sealed with a stainless steel Swagelok cap (3/8 in) at the open end. The synthesis was performed in a sealed alumina tube furnace, which was purged with Ar gas for 20 min, rapidly ramped to 300°C within 10 min, and held at the same temperature for 16 h for the reaction. Continuous Ar gas with a flow rate of ~ 30 mL/min flowed into the sealed furnace during the entire synthesis process. The final products were collected after the furnace was naturally cooled down to RT and were immediately transferred into the glovebox.

Synthesis of Na_3SbS_4

Na_3SbS_4 in **Chapter 3** was synthesized using a solid-state sintering method. Na_2S (Alfa Aesar, 99.8%), antimony (Sigma-Aldrich, 99.5% trace metals basis), and sulfur (Sigma-Aldrich, ≥99.5%) were used as precursors. A stoichiometric amount of powder precursors was mixed in an argon-filled glovebox. The resulting mixture (~1 g) was then placed into a BN tube (3-mm inner diameter and 4-mm outer diameter), which was wrapped in aluminum foil, with the open end sealed with a stainless-steel Swagelok cap (9.525 mm). This tube was transferred into a sealed alumina tube furnace, which was purged with pre-dried Ar gas (oxygen/moisture traps, model MT200-4-D, Agilent). The temperature of the furnace was rapidly increased to 550 °C within ~30 min and then held for 17 h to allow the reaction to complete. During the reaction, a continuous flow

of Ar gas with a flow rate of approximately 50 mL min^{-1} was used. The resulting products were collected after the furnace was naturally cooled to room temperature and then immediately transferred into the glovebox and manually ground into powder.

LBO/LZrO coating method

The coated NCM^{523} samples were prepared using the sol-gel method reported in previous work (*146*). For the LBO-coated NCM^{523} sample (0.5 mol % LBO coated NCM^{523}), the LBO coating solution was first prepared by dissolving stoichiometric amount of Li acetate and triisopropyl borate in super dehydrated ethanol at 60 °C. Next, the NCM^{523} powder was dispersed in the as-prepared coating solution with stirring. Then, the solvent from the flask was removed using a rotary evaporator in a hot water bath (60°C) with ultrasound sonication, followed by a heat treatment at 350 °C in air. The LZrO-coated NCM^{523} (0.5 mol%) sample was prepared using a similar process. Details of the material synthesis and coating process are reported in reference (*147*).

Appendix B-2. Electrochemical measurements

The electrochemical stability of Na_3PX_4 conductors in **Chapter 2** are determined using a conventional liquid-based cell set-up. The as-synthesized solid electrolytes were ground into fine powders and then mixed with carbon and polymer binders to form film-type working electrodes, which were assembled in Swagelok cells with a liquid electrolyte against Na metal. The working electrode composites were prepared by mixing the Na_3PX_4 powder, carbon black, and poly(tetrafluoroethylene) (PTFE) in a weight ratio of 80:15:5 with a mortar and pestle in an Ar glovebox. This powder mixture was rolled into a thin film using a stainless steel plate and roller. Circular disks of 5/16-in diameter were then punched with a loading of approximately 3–5 mg. These electrodes were assembled into Swagelok cells with Na metal as the counter electrode and 1 M $NaPF_6$ in a 1:1 (volumetric ratio) ethylene carbonate/diethyl carbonate (EC/DEC) solvent mixture as the liquid electrolyte. Two glass fiber separators were used in the cells. The charging and discharging of the Swagelok cells were performed with an Arbin battery cycler. The corresponding results are presented in **Chapter 2**.

Full cells presented in **Chapter 3** using uncoated or LZrO/LBO-coated NCM^{523} as the cathode, LPS as the bulk SE, and graphite as the anode/reference electrode were constructed and cycled at a constant current (0.05 mA cm^{-2}). Both the cathode and anode

composites contained 60% active material, 35% LPS, and 5% CNF. The cells were assembled under an Ar atmosphere using otherwise identical procedure, and LPS powder from the same batch to maximize consistency. To prepare the full-cell SSBs, ~100 mg of LPS powder was cold pressed into a loose "pellet" under small pressure. Then, 10 mg of the cathode composite powders and anode composite powders were carefully added to both sides of the LPS pellet before applying a pressure of ~350 MPa for 5 min within an in-house-designed pressure cell (13-mm inner diameter) in an Ar-filled glovebox.

The Na-ion conductivity of Na_3SbS_4 presented in **Chapter 4** was evaluated using electrochemical impedance spectroscopy (EIS) with tantalum electrodes at temperatures ranging from 25 °C to 80 °C. The as-prepared Na_3SbS_4 powder was uniaxially compressed under a pressure of 1.5 tons before being sandwiched by tantalum foils (~0.05-mm thick) (Sigma Aldrich, ≥ 99.9%), which corresponds to an applied pressure of approximately 520 MPa. The ionic conductivities were measured for a 2.33-mm-thick pellet with a diameter of 6 mm. EIS measurements were performed using an EC-Lab Electrochemistry SP300, Biologic. The measurements were conducted at the initial open-circuit voltage in the frequency range of 7 MHz to 10 mHz with the application of a 10-mV signal amplitude. The measurements were performed using a Biologic Controlled Environment Sample Holder assembled and sealed in an Ar-filled glove box.

For the preparation for the Na metal symmetric cells in **Chapter 4**, ~140 mg of Na_3SbS_4 powder was cold pressed into a pellet under a pressure of ~1.5 tons for 5 min within an in-house-designed pressure cell (7.7-mm inner diameter) in an Ar-filled glovebox. For the electrolyte hydration treatment, the resulting Na_3SbS_4 pellet (~1-mm thick) was exposed to ambient air (humidity ~68%) to coat the Na_3SbS_4 pellet. Two metallic Na foils (6-mm diameter and <50-μm thickness) were then carefully attached on both sides of the pellet. The cells were assembled under an Ar atmosphere with otherwise identical procedures and used Na_3SbS_4 from the same batch of sintered powder to maximize consistency. EIS measurements of the samples were performed at room temperature (~25 °C) immediately after cell assembly. The symmetric cells were then cycled with a constant current density of 0.1 mA cm^{-2} at room temperature for 25 h using an EC-Lab Electrochemistry VMP300, Biologic. During cycling, the current direction was reversed every 30 min. A constant spring pressure (~3 MPa) was applied within the pressure cells during cycling.

Appendix B-3. Material characterization

Lab-based and synchrotron XRD experiments

Lab-based XRD measurement was performed using a Rigaku Miniflex diffractometer and Cu Kα radiation. The powder sample was first sealed into a Kapton tube (0.9 mm in diameter, Cole Parmer) in the glovebox and then characterized in the diffractometer, which was equipped with a capillary stage to limit air exposure.

Synchrotron XRD experiments was performed to observe the phase transformation process of Na_3SbS_4 upon air exposure in **Chapter 4**. The as-prepared Na_3SbS_4 powder was exposed to ambient air (humidity ~68%) under continuous grinding with a mortar and pestle for certain air-exposure durations (0–120 min). The final products were collected and then packed and sealed into a 1.1049-mm diameter Kapton capillary for further characterization in an Ar-filled glove box. SXRD experiments were performed at beamline 11-ID-B at the Advanced Photon Source (APS) of Argonne National Laboratory using a constant wavelength of 0.1432 Å. The use of high-energy X-rays (E = 86.57 keV) minimizes absorption effects. The Rietveld refinements were performed using the TOPAS 5.0 software package (Bruker).

For lattice parameter measurements and analysis of the NCM cathode during cycling in a full-cell SSB in **Chapter 3**, *in situ* XRD patterns were collected at beamline 11-ID-B at APS using home-designed cell shown in **Figure 3-13**. The cells were prepared in an Ar atmosphere using the same materials as those used for the pressure cell measurements in **Figure 3-7**. The cell was oriented perpendicularly to the X-ray beam (λ = 0.1432 Å). The detector was positioned at a distance of 100 cm from the sample. Background measurements were collected using identical cells but without the testing materials present. X-ray diffraction of the LBO-coated NCM cathode composite was measured every 10 minutes while cycling the cell u at a constant current (0.05 mA cm^{-2}) using a Maccor electrochemical station provided by the beamline. The SXRD data were integrated into a function of intensity vs. 2θ using FIT2D (*147*). Standard corrections (background, Compton scattering, detector effects) were applied, and Rietveld refinements were performed using the TOPAS 6.0 software package (Bruker).

For phase determination of the products at the Na/solid electrolyte interface in **Chapter 4**, spatially resolved *post-operando* XRD patterns of the symmetric cells were collected at beamline 11-ID-B at APS using the Radially Accessible Tubular In situ X-ray (RATIX) cell adapted for X-ray transmission. The cells were prepared in an Ar atmosphere using the same materials as those used for the pressure cell measurements in **Figure 4-4**. The RATIX cell (*121*) was oriented perpendicularly to the X-ray beam (λ = 0.1432 Å). The detector was positioned at a distance of 95 cm from the sample. The acquisition time for each diffraction pattern was 1 s, and the diffraction patterns were obtained consecutively at 13 positions from top to bottom along the vertical direction of the cell. Background

measurements were collected using identical cells but without the testing materials present. A CeO_2 standard was used to determine the sample geometry and sample-to-detector distance. The data were integrated into a function of intensity vs. 2θ using FIT2D (*149*). Standard corrections (background, Compton scattering, detector effects) were applied, and Rietveld refinements were performed using the TOPAS 5.0 software package (Bruker).

Thermal experiments

SDT measurements in **Chapter 2** were performed using a TA Instruments SDT Q600. Approximately 15 mg of the powder sample was first placed into an alumina sample pan in the glovebox. The filled pan was then placed on the pre-tared cantilever of the analyzer. SDT standard measurements were then performed under continuous Ar flow with a flow rate of 100 mL/min. The measurement procedure usually involves heating and cooling processes. After equilibrating at 25°C, the sample was heated to the set temperature at a heating rate of 5°C/min. The temperature was held for at least 1 h to complete the reaction before cooling was initiated at a rate of 2°C/min. The sample was rapidly transferred to the glovebox after measurement for further characterization.

Spectroscopy experiments

Lab-based XPS measurements in **Chapter 2** were performed on a PHI 5400 ESCA/XPS system with a monochromatic Al Kα X-ray source. The powder samples were mixed with PTFE binder (5 wt%) and rolled into thin films in the Ar glovebox. The films were transferred into the XPS system and cleaned using Ar ion milling (3 kV, 25 mA) to remove surface-absorbed C and O. The core-level spectra were fitted using the commonly applied Gaussian peak shapes and Shirley background correction to extract the transition metal valence states based on the ratio of scaled peak areas.

Electron microscopy experiments

SEM images were obtained on a Zeiss Gemini Ultra-55 analytical field-emission scanning electron microscope at the Molecular Foundry at Lawrence Berkeley National Laboratory (LBNL).

For (S)TEM experiments in **Chapter 3**, the coated/uncoated cathodes were extracted from disassembled cells. The composite cathodes powders were diluted in hexane and sonicated to obtain good particle dispersion. The TEM samples were prepared by drop casting the solution onto a standard 400 copper mesh TEM grid with lacey carbon support. The samples were loaded into a Gatan 648 double-tilt vacuum-transfer holder to transfer the sample from the glovebox to the microscope in an inert Ar atmosphere. The HRTEM and STEM–EDX characterizations were performed using a FEI TitanX 60-300 microscope. For each sample, more than 20 interfacial regions have been examined from different LZrO or LBO coated primary particles. The electron beam currents were carefully controlled during imaging to prevent electron irradiation damage to the samples. The high-resolution STEM and EELS analyses were performed using the TEAM I microscope (a modified FEI Titan 80-300 microscope with double-aberration-corrected (scanning) transmission electron microscope).

Appendix C. Computation methods

Appendix C-1 Phase diagrams and bulk energies

Zero Kelvin phase diagrams were constructed using the pymatgen software package (*150*) and a database of DFT-computed bulk phase energies of materials with crystal structures obtained from the Inorganic Crystal Structure Database (ICSD) (*150*) or generated by applying data-mined chemical substitutions (*151*). To obtain these bulk energies, we employed DFT within the projector augmented wave (PAW) formalism (*152*) using the generalized gradient approximation (GGA)(*153*) to the exchange-correlation energy as implemented in the Vienna ab initio simulation package (VASP) (*154*) to calculate the formation energy of each electrolyte from the nearest phases present in the NIST-JANAF (*155*) or Kubaschewski (*156*) thermochemical tables or from the elements. To treat the sulfides and selenides equally, we added the formation energy of Na_2Se to this dataset (*157*, *158*). We uniquely define the nearest phases as those that define the Gibbs triangle (the low-energy facet) containing the desired composition in the phase diagram. As a result of this methodology, the formation energy input to the phase diagram calculation is exactly the experimentally determined enthalpy for compounds that are present in these thermochemical tables. For other compounds, we use the sum of the experimental formation enthalpies of the nearby phases and the DFT calculated reaction energy from these nearby phases to form the compound of interest. This reduces the formation energy error by minimizing electron transfer in the DFT calculated reactions.

For all the VASP calculations, a cutoff energy of 520 eV and a *k*-point grid of at least 500 per number of atoms were used. We applied the mixing scheme of Jain et al. (*151*) to combine GGA calculations with/without the rotationally invariant Hubbard (+U) correction (*150*) to properly treat insulators and metals.

Appendix C-2 Voltage stability calculations

To calculate the voltage stability of each electrolyte in **Chapter 2** and **Chapter 4**, we calculated the range of Na chemical potential (μ_{Na}) over which each electrolyte was observed to be on the convex hull and therefore stable in the relevant 0 K grand potential phase diagram. At the extremes of the stability window, we determined its decomposition products as the compositions defining its associated Gibbs triangle. Topotactic Na extraction voltage (upper kinetic stability limit) is calculated from the

energy of removing a single Na atom from a 4-formula unit supercell, constraining the supercell dimensions to that of the stoichiometric bulk material but allowing atomic relaxations.

The electrochemical stability windows of LPS, LZrO and LBO in **Chapter 3** were calculated using the grand potential method developed in previous work (*152*). The topotactic Li extraction voltage (kinetic stability limit) is calculated as the energy of removing one Li atom from a supercell with at least 16 formula units. The DFT calculations were performed in Perdew–Burke–Ernzerhof (PBE) generalized gradient approximation (*150*) as implemented in the Vienna Ab initio Simulation Package (VASP) (*151*). The interactions between ion cores and valence electrons are described using the projector augmented wave (PAW) method with a plane-wave energy cutoff of 520 eV and a k-point density of at least 1,000/n_{atom}. (*134*, *135*) All supercells were fully relaxed in the DFT calculations.

Appendix C-3 Interfacial stability calculations

To determine the interfacial stability in **Chapter 2**, we determine the reaction between electrode and electrolyte compositions with the highest driving force as first proposed by Richards el.[34]. Because arbitrary amounts of either phase can be consumed by this reaction, this process results in a driving force given by the equation

$$\Delta E[c_a, c_b] = \min_{x\in[0,1]}\{E_{pd}[xc_a + (1-x)c_b] - xE[c_a] - (1-x)E[c_b]\}$$

where c_a and c_b are the compositions of the electrode and electrolyte, respectively; $E[c_a]$ and $E[c_b]$ are their bulk energies, respectively; $E_{pd}[c]$ is a function returning the energy of the lowest energy equilibrium of phases at the composition c; and x is a mixing parameter between 0 and 1. These calculations were not performed at constant Na chemical potential, in slight contrast to the methodologies of reference (*133*, *134*), to more accurately reflect the experimental conditions used in this work.

The chemical reaction energy at the solid/solid interfaces (cathode/SE, cathode/coating, and SE/coating interfaces) in **Chapter 4** is calculated with DFT data obtained from the Materials Project (*135*, *136*). The interface reaction calculation functionality is available through the Interface Reactions App of the Materials Project website (*134*, *135*).

Appendix C-4 Ion diffusion calculations

To study the Na-ion diffusion in $Na_3SbS_4 \cdot 8H_2O$ and $Na_3SbS_4 \cdot 9H_2O$ in **Chapter 3**, we performed climbing-image nudged elastic band (NEB) calculations (*159*, *160*) to determine the vacancy migration mechanism using DFT-calculated energies and forces. The vacancy was created by removing one Na ion from the pristine structure. Supercells containing 8 formula units were used for $Na_3SbS_4 \cdot 8H_2O$ and $Na_3SbS_4 \cdot 9H_2O$ to minimize the interaction between periodic images. A $2 \times 1 \times 1$ *k*-point grid was used, and the plane-wave energy cutoff was set to 400 meV for the NEB calculations.

Appendix D. Additional computation results

Table D-1 DFT calculations for all possible products of the reaction between Na_xMO_2 (x = 0.5 or 1.0) and Na_3PX_4

	$NaCrO_2$	$NaMnO_2$	$NaFeO_2$	$NaCoO_2$	$NaNiO_2$
Na_3PS_4	Na_3PO_4, Na_3PS_4, $NaCrO_2$, Na_3PSO_3, Na_3PS_3O, $Na_3P(SO)_2$, $NaCrS_2$	Na_2SO_4, Na_3PO_4, Na_3PS_4, Na_3PSO_3, Na_3PS_3O, $NaMnS_2$, MnS, MnO, $NaMnO_2$, $Na_3P(SO)_2$, Na_2MnS_2, $Na_4Mn_3S_5$	Na_2SO_4, Na_3PO_4, Na_3PS_4, $NaFeO_2$, Na_3PSO_3, Na_3PS_3O, FeS_2, Fe_3O_4, $Na_3P(SO)_2$, $Na_3(FeS_2)_2$	Na_2SO_4, Co, Na_3PO_4, Na_3PS_4, $NaCoO_2$, Na_3CoO_3, Co_9S_8, $NaCoS_2$, Na_2S, Na_3PSO_3, Na_3PS_3O, $Na_3P(SO)_2$	Ni_3S_4, Ni_3S_2, Na_2SO_4, $Na_6S_2O_9$, Na_3PO_4, Ni, Na_3PS_4, Na_3PSO_3, Na_2S, NaS, NiO, Na_3PS_3O, Na_4NiO_3, $Na_3P(SO)_2$, $Na_2Ni_3S_4$
Na_3PSe_4	Na_3PSe_4, Cr_2O_3, Na_3PO_4, $Na_4P_2O_7$, Na_3PSeO_3, $NaCrO_2$, $NaCrSe_2$, Na_3PSe_3O, Na_2Se	Na_3PSe_4, Na_2MnSe_3, $NaMnO_2$, NaSe, Mn_3O_4, MnO, $NaMnPO_4$, Na_2Se, Na_3PO_4	Na_3PSe_4, $FeSe_2$, FeSe, Na_3PSe_3O, Na_3PO_4, $Na_4P_2O_7$, Fe_2O_3, $NaFeO_2$, Na_3PSeO_3, Fe_2P, FeP, Fe_3O_4, FeO, Na_2Se	Na_3PSe_4, Na_3PSe_3O, $CoSe_2$, $Na_4P_2O_7$, Co_9Se_8, $NaCoO_2$, $NaCo_7O_{11}$, Na_3PSeO_3, Co_2P, Co_3O_4, CoO, Co_5Se_8, Na_2Se, Na_3PO_4	Na_3PSe_4, Ni_2P, Ni_3Se_4, NiO, $Na_4P_2O_7$, $Ni_{12}P_5$, Na_5NiO_4, Na_3PSeO_3, Ni_5Se_8, Na_2SeO_3, $NiSe_2$, NaSe, Na_3PSe_3O, Na_2Se, Na_3PO_4

(Continued)

	$Na_{0.5}CrO_2$	$Na_{0.5}MnO_2$	$Na_{0.5}FeO_2$	$Na_{0.5}CoO_2$	$Na_{0.5}NiO_2$
Na_3PS_4	Na_2SO_4, Cr_2O_3, Na_3PO_4, $Na_6Cr(SO_4)_4$, Na_3PS_4, $Na_4P_2O_7$, $NaCrO_2$, $Na_3Cr(PO_4)_2$, Na_2PS_3, Na_3PSO_3, $Na_3P(SO)_2$, S, $Na_{2/3}CrS_2$, $Na_3Cr_2(PS_4)_3$, Na_3PS_3O, $NaCrS_2$	Na_2SO_4, $NaMnO_2$, $NaMnS_2$, Na_3PS_4, MnS, Mn_3S_4, Na_3PS_3O, Na_3PSO_3, MnO, $Na_3P(SO)_2$, Na_2MnS_2, $Na_4Mn_3S_5$, $Na_{1/3}MnS_2$, $Na_{2/3}MnS_2$, Na_3PO4	Na_2SO_4, Na_3PO_4, Na_3PS_4, $NaFeO_2$, Na_3PSO_3, Na_3PS_3O, FeS_2, Fe_3O_4, $Na_3P(SO)_2$, $Na_{3/2}FeS_2$	Na_2SO_4, Co, Na_3PO_4, Na_3PS_4, $NaCoO_2$, Co_9S_8, $NaCoS_2$, Na_2S, Na_3PSO_3, Na_3PS_3O, CoS_2, $Na_3P(SO)_2$, $Na_{2/3}CoS_2$, CoO	Na_2SO_4, $NaNiPO_4$, $Na_6S_2O_9$, Na_3PO_4, Ni_3S_4, Ni, Na_3PS_4, NaS, Na_2S, Na_3PSO_3, NaS_2, Ni_9S_8, Ni_3S_2, $Na_3P(SO)_2$, Na_3PS_3O, $Na_2Ni_3S_4$, NiO
Na_3PSe_4	$Na_2CrP_2O_7$, Cr_2O_3, Na_3PO_4, $Na_4P_2O_7$, Na_3PSe_4, Na_2SeO_3, $NaCrSe_2$, $Na_3Cr(PO_4)_2$, $NaCrO_2$, $NaSe_2$, NaSe, Na_3PSe_3O, Se	$MnSe_2$, Na_3PSe_4, Na_2MnSe_3, $NaMnO_2$, MnO, $NaSe_2$, Mn_3O_4, Na_2SeO_3, NaSe, $NaMnPO_4$, Na_3PO_4	Na_3PSe_4, $FeSe_2$, FeSe, Na_3PSe_3O, Na_3PO_4, $Na_4P_2O_7$, Fe_2O_3, FeO, Na_3PSeO_3, $NaSe_2$, Fe_2P, FeP, Na_2SeO_3, $NaFeO_2$, NaSe, Fe_3O_4, Na_2Se	Na_3PSe_4, Na_3PSe_3O, $CoSe_2$, $Na_4P_2O_7$, $NaCo_7O_{11}$, Na_3PSeO_3, Na_2SeO_3, Co_3O_4, Co_2P, Na_2Se, Co_5Se_8, CoO, Na_3PO_4	Na_3PSe_4, Ni_2P, Na_3PSe_3O, NiO, $Na_4P_2O_7$, Na_2SeO_4, Na_4SeO_5, Na_3PSeO_3, Na_2SeO_3, Ni_5Se_8, $NiSe_2$, NaSe, $Ni_{12}P_5$, Na_2Se, Na_3PO4

Table D-2 Reactions between cathode/SE, cathode/coating, and coating/SE with the maximum driving force

Interface	Reaction energy (meV/atom)	Reaction equation
NCM^{523}/LPS	−414	$0.333\ Li_3PS_4 + 0.667\ LiMn_{0.3}Co_{0.2}Ni_{0.5}O_2 \rightarrow 0.006\ Ni_3S_4 + 0.006\ Ni_9S_8 + 0.133\ Co(NiS_2)_2 + 0.2\ MnS_2 + 0.333\ Li_2S + 0.333\ Li_3PO_4$
NCM^{523}/LZrO	0	--
NCM^{523}/LBO	−27	$0.312\ Li_3B_{11}O_{18} + 0.688\ LiMn_{0.3}Co_{0.2}Ni_{0.5}O_2 \rightarrow 0.054\ Li_2Mn_3NiO_8 + 0.043\ Li_2MnCo_3O_8 + 0.476\ Li_3B_7O_{12} + 0.002\ Co_3O_4 + 0.097\ Ni_3BO_5$
LZrO/LPS	−111	$0.333\ Li_3PS_4 + 0.667\ Li_2ZrO_3 \rightarrow 0.667\ ZrSO + 0.333\ Li_3PO_4 + 0.667\ Li_2S$
LBO/LPS	0	--

Table D-3 Decomposition products of Na_3SbS_4 at various Na chemical potentials calculated by DFT

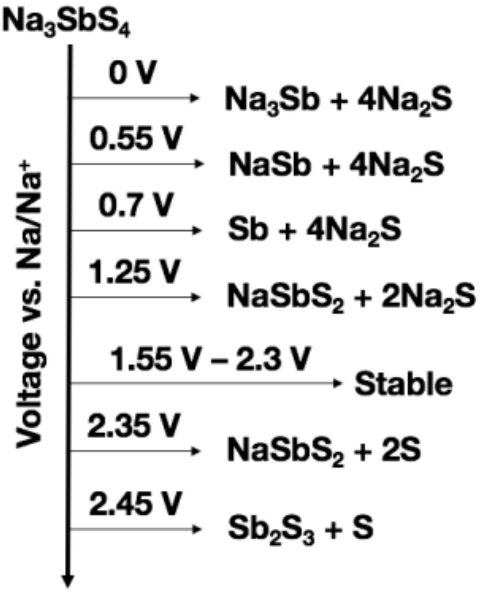


Table D-4 Decomposition products of $Na_3SbS_4 \cdot 9H_2O$ at various Na chemical potentials calculated by DFT

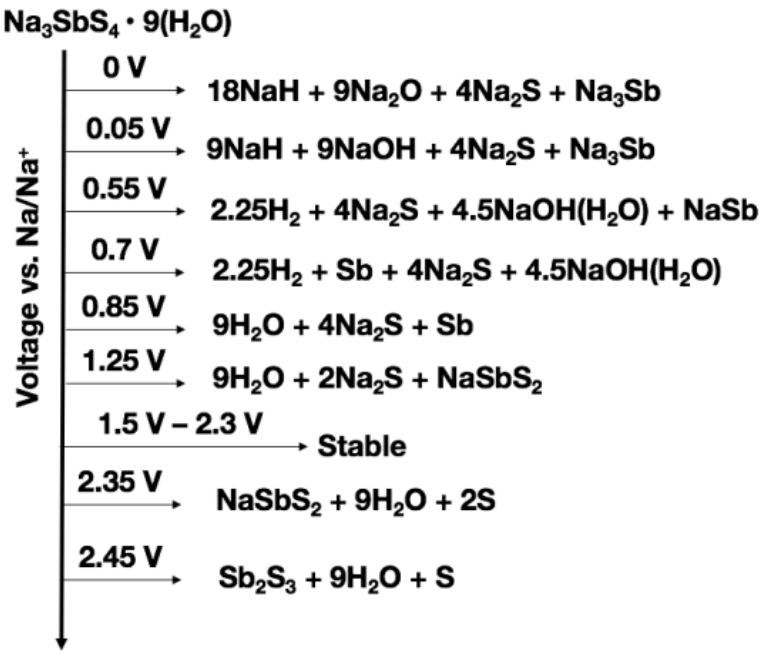


Table D-5 Decomposition of Na-containing hydrated compound in the Materials Project database with Na metal

Materials Project ID	Compound Formula	Reaction products with Na
mp-695982	$BaNaP_3(HO_2)_6$	BaNaP + BaO + **NaH** + Na_3PO_4
mp-720334	$Na_2P_2H_{14}O_{13}$	**Na_2O** + **NaH** + Na_3PO_4
mp-720570	$Na_2PH_{11}O_8$	**Na_2O** + **NaH** + Na_3PO_4
mp-708993	$Na_2PH_{15}O_{11}$	**Na_2O** + **NaH** + Na_3PO_4
mp-644245	$Na_2PH_3O_5$	**Na_2O** + **NaH** + Na_3PO_4
mp-698223	$Na_2PH_5O_6$	**Na_2O** + **NaH** + Na_3PO_4
mp-720853	$Na_2PH_5O_6$	**Na_2O** + **NaH** + Na_3PO_4
mp-722977	$Na_2Si(H_3O_2)_6$	Na_4SiO_4 + **Na_2O** + **NaH**
mp-24369	$Na_2Si(H_4O_3)_3$	Na_4SiO_4 + **Na_2O** + **NaH**
mp-707840	$Na_2Si(H_5O_4)_2$	Na_4SiO_4 + **Na_2O** + **NaH**
mp-698025	$Na_2Si_3(HO_4)_2$	Na_2SiO_3 + NaSi + **NaH**
mp-504605	$Na_2SiH_{16}O_{11}$	Na_4SiO_4 + **Na_2O** + **NaH**
mp-733509	$Na_2TiSi_4H_4O_{13}$	Na_4SiO_4 + Na_4TiO_4 + **NaH** + Ti_5Si_4
mp-740740	$Na_2ZnP(H_5O_4)_3$	**Na_2O** + $NaZn_{13}$ + **NaH** + Na_3PO_4
mp-707459	$Na_2ZnP_2(H_5O_6)_2$	**Na_2O** + $NaZn_{13}$ + **NaH** + Na_3PO_4
mp-540885	$Na_3PH_{16}(SO_2)_4$	**Na_2O** + Na_2S + **NaH** + Na_3PO_4

mp-761853	$Na_3PH_{22}(SO_4)_3$	**Na_2O** + Na_2S + **NaH** + Na_3PO_4
mp-761853	$Na_3PH_{22}(SO_4)_3$	Na_3PO_4 + **NaH** + Na_2S + **Na_2O**
mp-24440	$Na_3SbS_4(H_2O)_9$	**NaH** + Na_3Sb + **Na_2O** + Na_2S
mp-707571	$Na_3SiH_{11}O_9$	Na_4SiO_4 + **Na_2O** + **NaH**
mp-703468	$Na_3SiH_5O_6$	Na_4SiO_4 + **Na_2O** + **NaH**
mp-740750	$Na_4P_4(H_2O_5)_3$	Na_3P + **NaH** + Na_3PO_4
mp-703521	$Na_5P_3(H_3O_4)_4$	**Na_2O** + **NaH** + Na_3PO_4
mp-676991	$NaAlSi_2H_2O_7$	Na_2SiO_3 + $NaAlO_2$ + NaSi + **NaH**
mp-696175	$NaAsH_4O_5$	Na_3As + **NaH** + **Na_2O**
mp-696157	$NaP(HO)_6$	**Na_2O** + **NaH** + Na_3PO_4
mp-24109	$NaP(HO_2)_2$	**NaH** + Na_3PO_4
mp-554288	$NaPH_4O_5$	**Na_2O** + **NaH** + Na_3PO_4
mp-976402	$NaZnAs(H_2O_3)_2$	Na_3As + $NaZn_{13}$ + **NaH** + **Na_2O**

Table D-6 Decomposition of Li-containing hydrated compound in the Materials Project database with Li metal

Materials Project ID	Compound Formula	Reaction products with Li
mp-774386	$Li_2Cr_3P_4(HO_4)_4$	Li_3P + Cr + **LiH** + **Li_2O**
mp-779945	$Li_2CrP_4(H_2O_3)_6$	Cr + Li_3P + **LiH** + **Li_2O**
mp-763724	$Li_2CrP_4(H_4O_5)_4$	Li_3P + Cr + **Li_2O** + **LiH**
mp-850031	$Li_2Fe_3P_4(HO_4)_4$	Li3P + Fe + **LiH** + **Li_2O**
mp-763722	$Li_2FeP_4(H_4O_5)_4$	Li_3P + Fe + **Li_2O** + **LiH**
mp-778628	$Li_2Mn_3P_4(HO_4)_4$	Li_3P + Mn + **LiH** + **Li_2O**
mp-762848	$Li_2MnP_4(H_4O_5)_4$	Li_3P + **LiH** + **Li_2O** + Mn
mp-703343	$Li_2Sn(H_5O_4)_2$	$Li_{17}Sn_4$ + **LiH** + **Li_2O**
mp-850076	$Li_2V_3P_4(HO_4)_4$	Li_3P + V + **Li_2O** + **LiH**
mp-780300	$Li_2VP_4(H_2O_3)_6$	Li_3P + V + **Li_2O** + **LiH**
mp-763755	$Li_2VP_4(H_4O_5)_4$	Li_3P + V + **Li_2O** + **LiH**
mp-24104	$LiAlSi_2H_2O_7$	$Li_{21}Si_5$ + Li_9Al_4 + **LiH** + **Li_2O**
mp-697020	$LiAlSiH_2O_5$	$Li_{21}Si_5$ + Li_9Al_4 + **Li_2O** + **LiH**
mp-556562	$LiAsH_6(OF_2)_3$	Li_3As + LiF + **Li_2O** + **LiH**
mp-780488	$LiCrP_2H_5O_9$	Li_3P + Cr + **LiH** + **Li_2O**
mp-782655	$LiFeP(H_6O_5)_2$	Li_3P + Fe + **LiH** + **Li_2O**
mp-850377	$LiFeP_2H_5O_9$	Li_3P + Fe + **LiH** + **Li_2O**

mp-850955	$LiFeP_3(H_7O_8)_2$	Li_3P + Fe + **LiH** + **Li_2O**
mp-779204	$LiFeP_3H_8O_{13}$	Li_3P + Fe + **LiH** + **Li_2O**
mp-780206	$LiFePH_2O_5$	Li_3P + Fe + **Li_2O** + **LiH**
mp-850407	$LiMnP(H_6O_5)_2$	Li_3P + Mn + **LiH** + **Li_2O**
mp-780930	$LiMnP_3H_8O_{13}$	Li_3P + **LiH** + **Li_2O** + Mn
mp-763764	$LiMnPH_2O_5$	Li_3P + Mn + **LiH** + **Li_2O**
mp-560246	$LiUP(H_4O5)_2$	Li_3P + U + **Li_2O** + **LiH**
mp-780313	$LiVP_3(H_7O_8)_2$	V + Li_3P + **LiH** + **Li_2O**
mp-778576	$LiVP_4(H_2O_7)_2$	V + Li_3P + **Li_2O** + **LiH**
mp-774651	$LiZnAsH_2O_5$	Li_3As + LiZn + **LiH** + **Li_2O**
mp-24585	$LiZnPH_2O_5$	Li_3P + LiZn + **Li_2O** + **LiH**

Appendix E. Additional experiment results

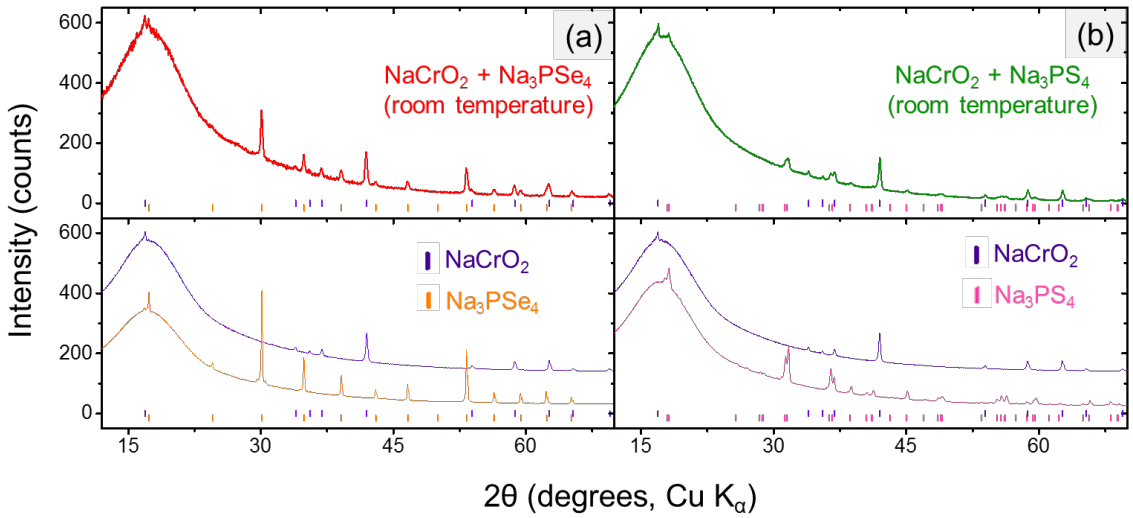


Figure E-1 (a–b) Diffraction patterns of $NaCrO_2$, Na_3PX_4, and mixture of the paired materials at RT (25°C); the tick marks indicate $NaCrO_2$ (purple, top) and Na_3PX_4 (orange for Na_3PSe_4, pink for Na_3PS_4, bottom) peaks. The diffraction pattern of the mixed materials is almost the same as the sum of those of each individual component, suggesting that no bulk reaction occurs between $NaCrO_2$ and Na_3PX_4 after mixing at RT.

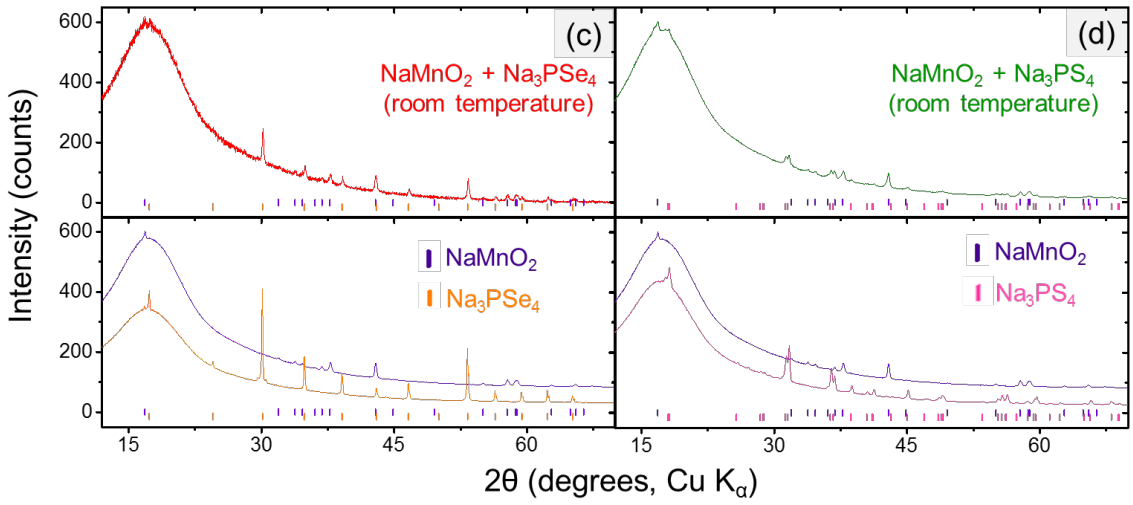


Figure E-1 (c–d) Diffraction patterns of $NaMnO_2$, Na_3PX_4, and a mixture of the paired materials at RT (25°C); the tick marks indicate $NaMnO_2$ (purple, top) and Na_3PX_4 (orange for Na_3PSe_4, pink for Na_3PS_4, bottom) peaks. No bulk reaction is observed between $NaMnO_2$ and Na_3PX_4 after mixing at RT.

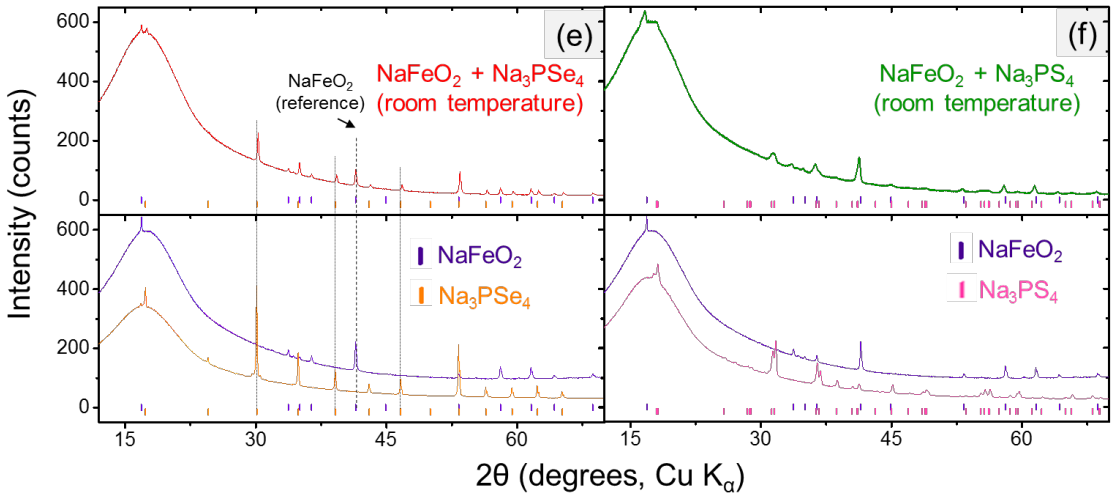


Figure E-1 (e–f) Diffraction patterns of $NaFeO_2$, Na_3PX_4, and a mixture of the paired materials RT (25°C); the tick marks indicate $NaFeO_2$ (purple, top) and Na_3PX_4 (orange for Na_3PSe_4, pink for Na_3PS_4, bottom) peaks. Peak shifts are observed in (e) at 30°, 39°, and 46°, indicating that $NaFeO_2$ reacts with Na_3PSe_4 at RT. Note that only peak shifts of Na_3PSe_4 are observed (one peak of $NaFeO_2$ is marked as reference). No bulk reaction is observed between $NaCrO_2$ and Na_3PS_4 after mixing at RT in (f).

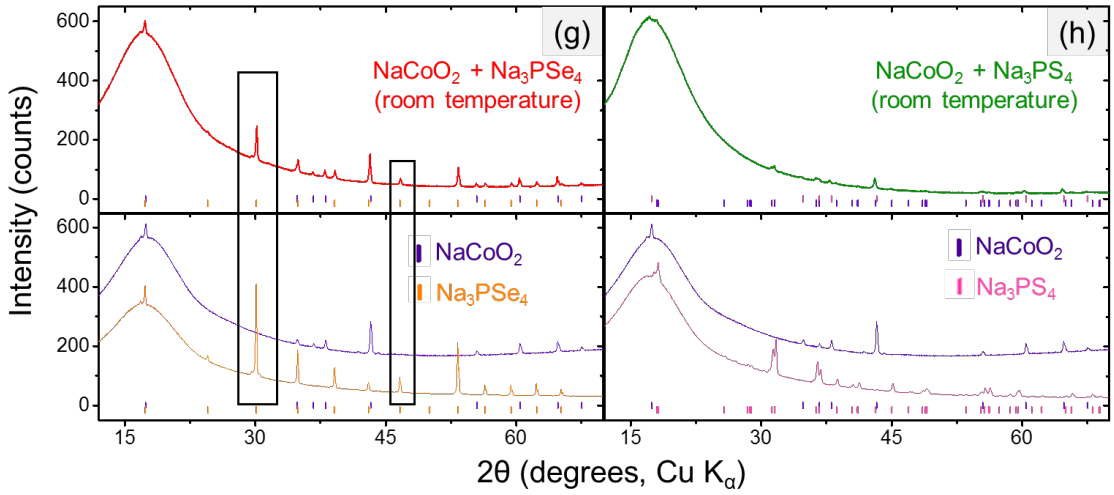


Figure E-1 (g–h) Diffraction patterns of $NaCoO_2$, Na_3PX_4, and a mixture of the paired materials at RT (25°C); the tick marks indicate $NaCoO_2$ (purple, top) and Na_3PX_4 (orange for Na_3PSe_4, pink for Na_3PS_4, bottom) peaks. Peak shape changes are observed in (g) at 30° and 46°, indicating that $NaCoO_2$ reacts with Na_3PSe_4 at RT. No bulk reaction is observed between $NaCoO_2$ and Na_3PS_4 after mixing at RT in (h).

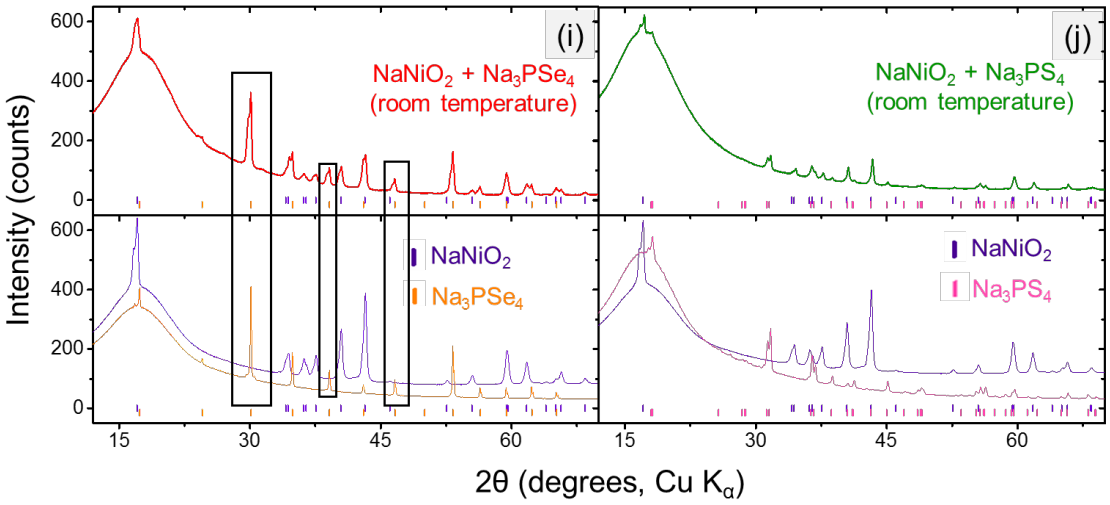


Figure E-1 (i–j) Diffraction patterns of $NaNiO_2$, Na_3PX_4, and a mixture of the paired materials at RT (25°C); the tick marks indicate $NaNiO_2$ (purple, top) and Na_3PX_4 (orange for Na_3PSe_4, pink for Na_3PS_4, bottom) peaks. Peak shape changes are observed in (i) at 30°, 39°, and 46°, indicating that $NaNiO_2$ reacts with Na_3PSe_4 at RT. No bulk reaction is observed between $NaNiO_2$ and Na_3PS_4 after mixing at RT in (j).

Appendix F. Crystal structure of $Na_3SbS_4 \cdot 8H_2O$

$Na_{12}Sb_4S_{16} \cdot 32H_2O$ (i.e., $Na_3SbS_4 \cdot 8H_2O$ written in empirical formula) is crystallized in the space group of $P12_1/c1$ (space group No. 14). The structure consists of $Na(H_2O,S)_6$ octahedra and SbS_4 tetrahedra that are linked to form corrugated layers parallel to (010), as shown in **Figure F-1**. Na ions occupy four different crystallographic sites. Na(1) and Na(2) are coordinated by four H_2O and two S^{2-}, Na(3) by five H_2O and one S^{2-}, and Na(4) by six H_2O. The Na(3) octahedron shares an edge defined by pairs of H_2O molecules with the Na(1) octahedron and shares another edge with another Na(3) octahedron, forming a Na(1)–Na(3)–Na(3)–Na(1)–… Na conduction channel, as shown in **Figure F-2**. Similarly, the Na(4) octahedron shares an edge with the Na(2) octahedron and shares another edge with another Na(4) octahedron, forming another Na(2)–Na(4)–Na(4)–Na(2)–… Na conduction channel. The Na(4) octahedron is also connected to the Na(3) octahedron by one H_2O molecule, forming a third Na(4)–Na(2)–Na(4)–Na(3)–Na(1)–Na(3)–… Na conduction channel. The SbS_4 tetrahedra are present on both sides of the (010) face by sharing three of their four S atoms with the Na octahedra, while the other S atom protrudes from the (010) face and is not shared with any other Na or Sb polyhedral. Parallel to the (010) lattice direction, the structure consists of corrugated layers with the composition $Na_3SbS_4 \cdot 8H_2O$. The atomic positions of the H atoms were fixed in the Rietveld refinement process. According to a previous neutron diffraction study of $Na_3AsS_4 \cdot 8D_2O$ (*133*, *134*), the layers are reinforced by nine independent intralayer hydrogen bonds formed by water molecules; these layers are stacked above each other by the c-glide plane symmetry operation and are interconnected by six interlayer hydrogen bonds.

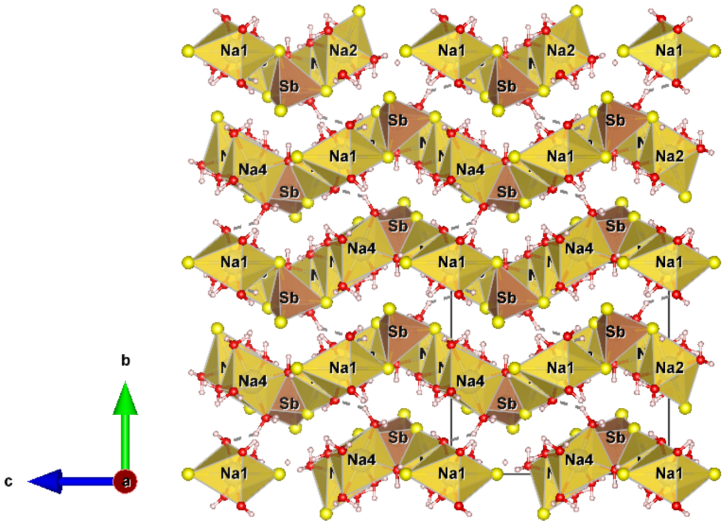


Figure F-1 The linkage between $Na(H_2O,S)_6$ octahedra and SbS_4 tetrahedra in $Na_3SbS_4 \cdot 8H_2O$ forming corrugated layers parallel to (010).

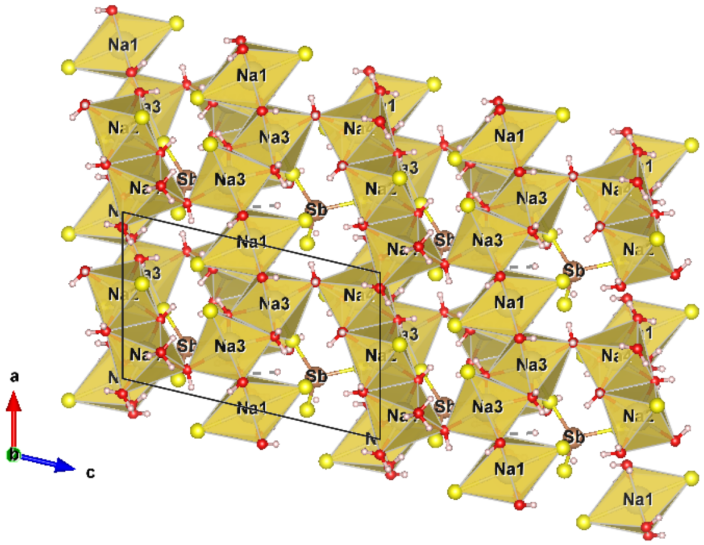


Figure F-2 Different Na diffusion channels in $Na_3SbS_4 \cdot 8H_2O$. Three channels are identified: Na(1)–Na(3)–Na(3)–Na(1)–…, Na(2)–Na(4)–Na(4)–Na(2)–…, and Na(4)–Na(2)–Na(4)–Na(3)–Na(1)–Na(3)–….

Table F-1 Atomic site information for $Na_3SbS_4 \cdot 8H_2O$ based on Rietveld refinement of synchrotron XRD data. The atomic coordinates for hydrogen atoms from the isostructural compound of $Na_3AsS_4.8D_2O$ were adopted and were fixed during the refinement.

Atom symbol	Wyckoff position	Site symmetry	x/a	y/b	z/c
Na1	2d	-1	1/2	0	1/2
Na2	2a	-1	0	0	0
Na3	4e	1	0.171(3)	0.566(2)	0.085(3)
Na4	4e	1	0.658(3)	0.0494(2)	0.086(2)
Sb	4e	1	0.2820(6)	0.1698(4)	0.2495(5)
S1	4e	1	0.208(2)	-0.0002(1)	0.2085(1)
S2	4e	1	0.4039(2)	0.1872(2)	0.4243(1)
S3	4e	1	0.4698(2)	0.2132(1)	0.1596(1)
S4	4e	1	0.073(2)	0.2812(1)	0.2157(1)
O1	4e	1	0.09119	0.38977	0.0008

O2	4e	1	0.14605	0.51933	0.2508
O3	4e	1	0.14888	0.65019	0.4662
O4	4e	1	0.19527	0.39663	0.4591
O5	4e	1	0.21189	0.73432	0.1490
O6	4e	1	0.40900	0.46034	0.1453
O7	4e	1	0.53093	0.42688	0.4108
O8	4e	1	0.73931	0.40236	0.0655
H01	4e	1	0.04674	0.53486	0.2669
H02	4e	1	0.07532	0.69039	0.4180
H03	4e	1	0.09599	0.35007	0.0606
H04	4e	1	0.13807	0.74534	0.1904
H05	4e	1	0.14681	0.44537	0.2519
H06	4e	1	0.16799	0.13989	0.4688
H07	4e	1	0.17391	0.80938	0.1026
H08	4e	1	0.17667	0.34779	0.4050
H09	4e	1	0.25892	0.14099	0.1014
H10	4e	1	0.41115	0.38639	0.1462
H11	4e	1	0.50208	0.47942	0.1949
H12	4e	1	0.49548	0.35749	0.3951
H13	4e	1	0.60649	0.44308	0.3719
H14	4e	1	0.68646	0.23245	0.3048
H15	4e	1	0.71145	0.33204	0.0747
H16	4e	1	0.77352	0.43011	0.1319

Bibliography

1. G. E. Blomgren, The Development and Future of Lithium Ion Batteries. *J. Electrochem. Soc.* **164**, A5019–A5025 (2017).

2. P. Albertus, S. Babinec, S. Litzelman, A. Newman, Status and challenges in enabling the lithium metal electrode for high-energy and low-cost rechargeable batteries. *Nature Energy*. **3**, 16–21 (2018).

3. E. A. Olivetti, G. Ceder, G. G. Gaustad, X. Fu, Lithium-Ion Battery Supply Chain Considerations: Analysis of Potential Bottlenecks in Critical Metals. *Joule*. **1**, 229–243 (2017).

4. Z. P. Cano, D. Banham, S. Ye, A. Hintennach, J. Lu, M. Fowler, Z. Chen, Batteries and fuel cells for emerging electric vehicle markets. *Nature Energy*. **3**, 279–289 (2018).

5. A. Kwade, W. Haselrieder, R. Leithoff, A. Modlinger, F. Dietrich, K. Droeder, Current status and challenges for automotive battery production technologies. *Nature Energy*. **3**, 290–300 (2018).

6. Global EV Outlook 2019, (available at https://www.iea.org/publications/reports/globalevoutlook2019/).

7. G. Crabtree, The coming electric vehicle transformation. *Science*. **366**, 422–424 (2019).

8. P. Canepa, G. Sai Gautam, D. C. Hannah, R. Malik, M. Liu, K. G. Gallagher, K. A. Persson, G. Ceder, Odyssey of Multivalent Cathode Materials: Open Questions and Future Challenges. *Chem. Rev.* **117**, 4287–4341 (2017).

9. D. Andre, S.-J. Kim, P. Lamp, S. F. Lux, F. Maglia, O. Paschos, B. Stiaszny, Future generations of cathode materials: an automotive industry perspective. *J. Mater. Chem. A Mater. Energy Sustain.* **3**, 6709–6732 (2015).

10. R. Schmuch, R. Wagner, G. Hörpel, T. Placke, M. Winter, Performance and cost of materials for lithium-based rechargeable automotive batteries. *Nature Energy*. **3**, 267–278 (2018).

11. O. Gröger, H. A. Gasteiger, J.-P. Suchsland, Erratum: Review—Electromobility: Batteries or Fuel Cells?[J. Electrochem. Soc., 162, A2605 (2015)]. *J. Electrochem. Soc.* **163**, X3–X3 (2016).

12. A. Hern, Samsung must act fast to keep an exploding phone from blowing up its brand. *The Guardian* (2016), (available at http://www.theguardian.com/technology/2016/oct/10/samsung-galaxy-note-7-exploding-phone-brand).

13. B. Vlasic, Car Fire a Test for High-Flying Tesla. *The New York Times* (2013), (available at https://www.nytimes.com/2013/10/04/business/car-fire-a-test-for-high-flying-tesla.html).

14. W. D. Richards, L. J. Miara, Y. Wang, J. C. Kim, G. Ceder, Interface Stability in Solid-State Batteries. *Chem. Mater.* **28**, 266–273 (2016).

15. Solid Power, BMW partner to develop next-generation EV batteries. *Reuters* (2017), (available at https://www.reuters.com/article/us-bmw-solid-power-idUSKBN1EC16V).

16. Toyota set to sell long-range, fast-charging electric cars in 2022: paper. *Reuters* (2017), (available at https://www.reuters.com/article/us-toyota-electric-cars-idUSKBN1AA035).

17. S. Ji-hye, [Exclusive] Hyundai Motor solely developing EV batteries. *The Korea Herald* (2017), (available at http://www.koreaherald.com/view.php?ud=20170405000762).

18. B. Halvorson, B. H.-S. Editor, A. C.-M. Editor, B. Hurd-Contributor, VW confirms it's planning for solid-state batteries by 2025. *Green Car Reports*, (available at https://www.greencarreports.com/news/1119182_vw-confirms-its-planning-for-solid-state-batteries-by-2025).

19. Y. Kato, S. Hori, T. Saito, K. Suzuki, M. Hirayama, A. Mitsui, M. Yonemura, H. Iba, R. Kanno, High-power all-solid-state batteries using sulfide superionic conductors. *Nature Energy*. **1**, 16030 (2016).

20. P. Nelson, K. Gallagher, I. Bloom, BatPaC: A lithium-ion battery performance and cost model for electric-drive vehicles. *Chemical Science and Engineering Division, Argonne National Laboratory, Tech. Rep* (2015).

21. L. Fan, S. Wei, S. Li, Q. Li, Y. Lu, Recent progress of the solid - state electrolytes for high - energy metal - based batteries. *Advanced Energy Materials* (2018) (available at https://onlinelibrary.wiley.com/doi/abs/10.1002/aenm.201702657).

22. Z. Gao, H. Sun, L. Fu, F. Ye, Y. Zhang, W. Luo, Y. Huang, Promises, Challenges, and Recent Progress of Inorganic Solid-State Electrolytes for All-Solid-State Lithium Batteries. *Adv. Mater.* (2018), doi:10.1002/adma.201705702.

23. U. v. Alpen, A. Rabenau, G. H. Talat, Ionic conductivity in Li3N single crystals. *Appl. Phys. Lett.* **30**, 621–623 (1977).

24. R. Murugan, V. Thangadurai, W. Weppner, Fast Lithium Ion Conduction in Garnet-Type Li7La3Zr2O12. *Angew. Chem. Int. Ed.* **46**, 7778–7781 (2007).

25. Y. X. Gao, X. P. Wang, W. G. Wang, Z. Zhuang, D. M. Zhang, Q. F. Fang, Synthesis, ionic conductivity, and chemical compatibility of garnet-like lithium ionic conductor Li5La3Bi2O12. *Solid State Ionics*. **181**, 1415–1419 (2010).

26. S. Ohta, T. Kobayashi, T. Asaoka, High lithium ionic conductivity in the garnet-type oxide Li7−X La3(Zr2−X, NbX)O12 (X=0–2). *J. Power Sources*. **196**, 3342–3345 (2011).

27. Y. Li, J.-T. Han, C.-A. Wang, H. Xie, J. B. Goodenough, Optimizing Li+ conductivity in a garnet framework. *J. Mater. Chem.* **22**, 15357–15361 (2012).

28. H. Yamane, M. Shibata, Y. Shimane, T. Junke, Y. Seino, S. Adams, K. Minami, A. Hayashi, M. Tatsumisago, Crystal structure of a superionic conductor, Li7P3S11. *Solid State Ionics*. **178**, 1163–1167 (2007).

29. N. Kamaya, K. Homma, Y. Yamakawa, M. Hirayama, R. Kanno, M. Yonemura, T. Kamiyama, Y. Kato, S. Hama, K. Kawamoto, A. Mitsui, A lithium superionic conductor. *Nat. Mater.* **10**, 682–686 (2011).

30. H. Aono, E. Sugimoto, Y. Sadaoka, N. Imanaka, G. Adachi, Ionic Conductivity of Solid Electrolytes Based on Lithium Titanium Phosphate. *J. Electrochem. Soc.* **137**, 1023–1027 (1990).

31. P. Bron, S. Johansson, K. Zick, J. S. A. Der Günne, S. Dehnen, B. Roling, J. Schmedt auf der Günne, S. Dehnen, B. Roling, Li10SnP2S12: An Affordable Lithium Superionic Conductor. *J. Am. Chem. Soc.* **135**, 15694–15697 (2013).

32. Z. Liu, W. Fu, E. A. Payzant, X. Yu, Z. Wu, N. J. Dudney, J. Kiggans, K. Hong, A. J. Rondinone, C. Liang, Anomalous High Ionic Conductivity of Nanoporous β-Li3PS4. *J. Am. Chem. Soc.* **135**, 975 – 978 (2013).

33. A. Kuhn, V. Duppel, B. V. Lotsch, Tetragonal Li 10 GeP 2 S 12 and Li 7 GePS 8--exploring the Li ion dynamics in LGPS Li electrolytes. *Energy Environ. Sci.* **6**, 3548–3552 (2013).

34. N. Suzuki, W. D. Richards, Y. Wang, L. J. Miara, J. C. Kim, I.-S. Jung, T. Tsujimura, G. Ceder, Synthesis and Electrochemical Properties of I4̄-Type Li1+2xZn1–xPS4 Solid Electrolyte. *Chem. Mater.* **30**, 2236–2244 (2018).

35. H.-J. Deiseroth, S.-T. Kong, H. Eckert, J. Vannahme, C. Reiner, T. Zaiss, M. Schlosser, Li6PS5X: a class of crystalline Li-rich solids with an unusually high Li+ mobility. *Angew. Chem. Int. Ed.* **47**, 755–758 (2008).

36. H.-P. Hong, Crystal structures and crystal chemistry in the system Na1+ xZr2SixP3- xO12. *Mater. Res. Bull.* **11**, 173–182 (1976).

37. E. M. Vogel, R. J. Cava, E. Rietman, Na+ ion conductivity and crystallographic cell characterization in the Hf-nasicon system Na1+ xHf2SixP3- xO12. *Solid State Ionics*. **14**, 1–6 (1984).

38. T. Takahashi, K. Kuwabara, M. Shibata, Solid-state ionics - conductivities of Na+ ion conductors based on NASICON. *Solid State Ionics*. **1**, 163–175 (1980).

39. A. Hooper, P. McGeehin, A. E. Hughes, in *Superionic Conductors*, G. D. Mahan, W. L. Roth, Eds. (Springer US, Boston, MA, 1976), pp. 99–100.

40. W. S. Tang, A. Unemoto, W. Zhou, V. Stavila, M. Matsuo, H. Wu, S.-I. Orimo, T. J. Udovic, Unparalleled Lithium and Sodium Superionic Conduction in Solid Electrolytes with Large Monovalent Cage-like Anions. *Energy Environ. Sci.* **8**, 3637–3645 (2015).

41. W. S. Tang, K. Yoshida, A. V. Soloninin, R. V. Skoryunov, O. A. Babanova, A. V. Skripov, M. Dimitrievska, V. Stavila, S.-I. Orimo, T. J. Udovic, Stabilizing Superionic-Conducting Structures via Mixed-Anion Solid Solutions of Monocarba-closo-borate Salts. *ACS Energy Lett.* **1**, 659–664 (2016).

42. A. Banerjee, K. H. Park, J. W. Heo, Y. J. Nam, C. K. Moon, S. M. Oh, S.-T. Hong, Y. S. Jung, Na3 SbS4 : A Solution Processable Sodium Superionic Conductor for All-Solid-State Sodium-Ion Batteries. *Angew. Chem. Int. Ed Engl.* **55**, 9634–9638 (2016).

43. A. Hayashi, K. Noi, A. Sakuda, M. Tatsumisago, Superionic glass-ceramic electrolytes for room-temperature rechargeable sodium batteries. *Nat. Commun.* **3**, 856 (2012).

44. S.-H. Bo, Y. Wang, J. C. Kim, W. D. Richards, G. Ceder, Computational and Experimental Investigations of Na-Ion Conduction in Cubic Na3PSe4. *Chem. Mater.* **28**, 252–258 (2016).

45. Z. Zhang, E. Ramos, F. Lalère, A. Assoud, K. Kaup, P. Hartman, L. F. Nazar, Na11Sn2PS12: a new solid state sodium superionic conductor. *Energy Environ. Sci.* **11**, 87–93 (2018).

46. T. J. Udovic, M. Matsuo, W. S. Tang, H. Wu, V. Stavila, A. V. Soloninin, R. V. Skoryunov, O. A. Babanova, A. V. Skripov, J. J. Rush, Others, Exceptional Superionic Conductivity in Disordered Sodium Decahydro-closo-decaborate. *Adv. Mater.* **26**, 7622–7626 (2014).

47. W. D. Richards, T. Tsujimura, L. J. Miara, Y. Wang, J. C. Kim, S. P. Ong, I. Uechi, N. Suzuki, G. Ceder, Design and synthesis of the superionic conductor Na10SnP2S12. *Nat. Commun.* **7**, 11009 (2016).

48. Y. Wang, W. D. Richards, S. P. Ong, L. J. Miara, J. C. Kim, Y. Mo, G. Ceder, Design principles for solid-state lithium superionic conductors. *Nat. Mater.* **14**, 1026 (2015).

49. Y. Sun, Y.-C. Wang, X. Liang, Y. Xia, L. Peng, H. Jia, H. Li, L. Bai, J. Feng, H. Jiang, J. Xie, Rotational Cluster Anion Enabling Superionic Conductivity in Sodium-Rich Antiperovskite Na3OBH4. *J. Am. Chem. Soc.* (2019), doi:10.1021/jacs.9b01746.

50. C. K. Moon, H. J. Lee, K. H. Park, H. Kwak, J. W. Heo, K. Choi, H. Yang, M. S. Kim, S. T. Hong, J. H. Lee, S. J. Yoon, Vacancy-Driven Na+ Superionic Conduction in New Ca-Doped Na3PS4 for All-Solid-State Na-Ion Batteries. *ACS Energy Letters*. **3**, 2504–2512 (2018).

51. A. M. Nolan, Y. Zhu, X. He, Q. Bai, Y. Mo, Computation-Accelerated Design of Materials and Interfaces for All-Solid-State Lithium-Ion Batteries. *Joule*. **2**, 2016–2046 (2018).

52. M. Xu, M. S. Park, J. M. Lee, T. Y. Kim, Y. S. Park, E. Ma, Mechanisms of Li + transport in garnet-type cubic Li 3 + x La 3 M 2 O 12 (M = Te, Nb, Zr). *Phys. Rev. B Condens. Matter*. **85**, 52301 (2012).

53. X. He, Y. Zhu, Y. Mo, Origin of fast ion diffusion in super-ionic conductors. *Nat. Commun.* **8**, 15893 (2017).

54. K. Nie, Y. Hong, J. Qiu, Q. Li, X. Yu, H. Li, L. Chen, Interfaces Between Cathode and Electrolyte in Solid State Lithium Batteries: Challenges and Perspectives. *Front Chem*. **6**, 616 (2018).

55. W. Zhang, D. A. Weber, H. Weigand, T. Arlt, I. Manke, D. Schröder, R. Koerver, T. Leichtweiss, P. Hartmann, W. G. Zeier, J. Janek, Interfacial Processes and Influence of Composite Cathode Microstructure Controlling the Performance of All-Solid-State Lithium Batteries. *ACS Appl. Mater. Interfaces*. **9**, 17835–17845 (2017).

56. R. Koerver, I. Aygün, T. Leichtweiß, C. Dietrich, W. Zhang, J. O. Binder, P. Hartmann, W. G. Zeier, J. Janek, Capacity Fade in Solid-State Batteries: Interphase Formation and Chemomechanical Processes in Nickel-Rich Layered Oxide Cathodes and Lithium Thiophosphate Solid Electrolytes. *Chem. Mater.* **29**, 5574–5582 (2017).

57. Y. Xiao, Y. Wang, S.-H. Bo, J. C. Kim, L. J. Miara, G. Ceder, Understanding interface stability in solid-state batteries. *Nature Reviews Materials* (2019), doi:10.1038/s41578-019-0157-5.

58. G. Hautier, C. Fischer, V. Ehrlacher, A. Jain, G. Ceder, Data mined ionic substitutions for the discovery of new compounds. *Inorg. Chem.* **50**, 656–663 (2011).

59. A. Hayashi, K. Noi, N. Tanibata, M. Nagao, M. Tatsumisago, High sodium ion conductivity of glass–ceramic electrolytes with cubic Na3PS4. *J. Power Sources*. **258**, 420–423 (2014).

60. S. Wenzel, T. Leichtweiss, D. A. Weber, J. Sann, W. G. Zeier, J. Janek, Interfacial Reactivity Benchmarking of the Sodium Ion Conductors Na3PS4 and Sodium β-Alumina for Protected Sodium Metal Anodes and Sodium All-Solid-State Batteries. *ACS Appl. Mater. Interfaces*. **8**, 28216–28224 (2016).

61. Y. Tian, T. Shi, W. D. Richards, J. Li, J. C. Kim, S.-H. Bo, G. Ceder, Compatibility issues between electrodes and electrolytes in solid-state batteries. *Energy Environ. Sci.* **10**, 1150–1166 (2017).

62. Y. Tian, Y. Sun, D. C. Hannah, Y. Xiao, H. Liu, Reactivity-Guided Interface Design in Na Metal Solid-State Batteries. *Joule* (2019) (available at https://www.sciencedirect.com/science/article/pii/S2542435118306251).

63. P. Hartmann, T. Leichtweiss, M. R. Busche, M. Schneider, M. Reich, J. Sann, P. Adelhelm, J. Janek, Degradation of NASICON-Type Materials in Contact with Lithium Metal: Formation of Mixed Conducting Interphases (MCI) on Solid Electrolytes. *J. Phys. Chem. C.* **117**, 21064–21074 (2013).

64. J. Kasemchainan, S. Zekoll, D. Spencer Jolly, Z. Ning, G. O. Hartley, J. Marrow, P. G. Bruce, Critical stripping current leads to dendrite formation on plating in lithium anode solid electrolyte cells. *Nat. Mater.* (2019), doi:10.1038/s41563-019-0438-9.

65. M. J. Wang, R. Choudhury, J. Sakamoto, Characterizing the Li-Solid-Electrolyte Interface Dynamics as a Function of Stack Pressure and Current Density. *Joule*. **0** (2019), doi:10.1016/j.joule.2019.06.017.

66. T. Swamy, R. Park, B. W. Sheldon, D. Rettenwander, L. Porz, S. Berendts, R. Uecker, W. Craig Carter, Y.-M. Chiang, Lithium Metal Penetration Induced by Electrodeposition through Solid Electrolytes: Example in Single-Crystal Li6La3ZrTaO12 Garnet. *J. Electrochem. Soc.* **165**, A3648–A3655 (2018).

67. E. J. Cheng, A. Sharafi, J. Sakamoto, Intergranular Li metal propagation through polycrystalline Li6.25Al0.25La3Zr2O12 ceramic electrolyte. *Electrochim. Acta*. **223**, 85–91 (2017).

68. F. Han, A. S. Westover, J. Yue, X. Fan, F. Wang, M. Chi, D. N. Leonard, N. J. Dudney, H. Wang, C. Wang, High electronic conductivity as the origin of lithium dendrite formation within solid electrolytes. *Nature Energy*, 1 (2019).

69. M. Calpa, N. C. Rosero-Navarro, A. Miura, K. Tadanaga, Electrochemical performance of bulk-type all-solid-state batteries using small-sized Li7P3S11 solid electrolyte prepared by liquid phase as the ionic conductor in the composite cathode. *Electrochim. Acta*. **296**, 473–480 (2019).

70. N. Sun, Q. Liu, Y. Cao, S. Lou, M. Ge, X. Xiao, W.-K. Lee, Y. Gao, G. Yin, J. Wang, X. Sun, Anisotropically Electrochemo-Mechanical Evolution in Solid-State Batteries and Interfacial Tailored Strategy. *Angew. Chem. Int. Ed Engl.* (2019), doi:10.1002/anie.201910993.

71. S. P. Ong, Y. Mo, W. D. Richards, L. Miara, H. S. Lee, G. Ceder, Phase stability, electrochemical stability and ionic conductivity of the Li 10±1 MP 2 X 12 (M= Ge, Si, Sn, Al or P, and X= O, S or Se) family of superionic conductors. *Energy Environ. Sci.* **6**, 148–156 (2013).

72. C. Yada, Y. Iriyama, T. Abe, K. Kikuchi, Z. Ogumi, A novel all-solid-state thin-film-type lithium-ion battery with in situ prepared positive and negative electrode materials. *Electrochem. commun.* **11**, 413–416 (2009).

73. J. Xie, N. Imanishi, T. Zhang, A. Hirano, Y. Takeda, O. Yamamoto, Li-ion transport in all-solid-state lithium batteries with LiCoO2 using NASICON-type glass ceramic electrolytes. *J. Power Sources*. **189**, 365–370 (2009).

74. J. Wolfenstine, J. L. Allen, J. Sumner, J. Sakamoto, Electrical and mechanical properties of hot-pressed versus sintered LiTi2(PO4)3. *Solid State Ionics*. **180**, 961–967 (2009).

75. J. L. Allen, J. Wolfenstine, E. Rangasamy, J. Sakamoto, Effect of substitution (Ta, Al, Ga) on the conductivity of Li7La3Zr2O12. *J. Power Sources*. **206**, 315–319 (2012).

76. L. J. Miara, W. D. Richards, Y. E. Wang, G. Ceder, First-Principles Studies on Cation Dopants and Electrolyte|Cathode Interphases for Lithium Garnets. *Chem. Mater.* **27**, 4040–4047 (2015).

77. M. Tatsumisago, M. Nagao, A. Hayashi, Recent development of sulfide solid electrolytes and interfacial modification for all-solid-state rechargeable lithium batteries. *Journal of Asian Ceramic Societies*. **1**, 17–25 (2013).

78. G. Hautier, A. Jain, S. P. Ong, B. Kang, C. Moore, R. Doe, G. Ceder, Phosphates as lithium-ion battery cathodes: An evaluation based on high-throughput ab initio calculations. *Chem. Mater.* **23**, 3495–3508 (2011).

79. Y. Zhu, X. He, Y. Mo, First principles study on electrochemical and chemical stability of solid electrolyte–electrode interfaces in all-solid-state Li-ion batteries. *J. Mater. Chem. A Mater. Energy Sustain.* **4**, 3253–3266 (2016).

80. T. Minami, A. Hayashi, M. Tatsumisago, Recent progress of glass and glass-ceramics as solid electrolytes for lithium secondary batteries. *Solid State Ionics*. **177**, 2715–2720 (2006).

81. Y. Xiao, L. J. Miara, Y. Wang, G. Ceder, Computational Screening of Cathode Coatings for Solid-State Batteries. *Joule*. **0** (2019), doi:10.1016/j.joule.2019.02.006.

82. N. Ohta, K. Takada, L. Zhang, R. Ma, M. Osada, T. Sasaki, Enhancement of the High-Rate Capability of Solid-State Lithium Batteries by Nanoscale Interfacial Modification. *Adv. Mater.* **18**, 2226–2229 (2006).

83. K. Takada, N. Ohta, L. Zhang, K. Fukuda, I. Sakaguchi, R. Ma, M. Osada, T. Sasaki, Interfacial modification for high-power solid-state lithium batteries. *Solid State Ionics*. **179**, 1333–1337 (2008).

84. N. Ohta, K. Takada, I. Sakaguchi, L. Zhang, R. Ma, K. Fukuda, M. Osada, T. Sasaki, LiNbO3-coated LiCoO2 as cathode material for all solid-state lithium secondary batteries. *Electrochem. commun.* **9**, 1486–1490 (2007).

85. H. Wang, Y. Chen, Z. D. Hood, G. Sahu, A. S. Pandian, J. K. Keum, K. An, C. Liang, An Air-Stable Na3SbS4 Superionic Conductor Prepared by a Rapid and Economic Synthetic Procedure. *Angewandte Chemie - International Edition*. **55**, 8551–8555 (2016).

86. L. Zhang, D. Zhang, K. Yang, X. Yan, L. Wang, J. Mi, B. Xu, Y. Li, Vacancy-Contained Tetragonal Na3SbS4 Superionic Conductor. *Adv. Sci. Lett.* **3**, 1600089 (2016).

87. S. Wenzel, S. Randau, T. Leichtweiß, D. A. Weber, J. Sann, W. G. Zeier, J. Janek, Direct Observation of the Interfacial Instability of the Fast Ionic Conductor Li10GeP2S12 at the Lithium Metal Anode. *Chem. Mater.* **28**, 2400–2407 (2016).

88. K. H. Kim, Y. Iriyama, K. Yamamoto, S. Kumazaki, T. Asaka, K. Tanabe, C. A. J. Fisher, T. Hirayama, R. Murugan, Z. Ogumi, Characterization of the interface between LiCoO2 and Li7La3Zr2O12 in an all-solid-state rechargeable lithium battery. *J. Power Sources*. **196**, 764–767 (2011).

89. A. Sakuda, A. Hayashi, M. Tatsumisago, Interfacial observation between LiCoO2 electrode and Li 2S-P2S5 solid electrolytes of all-solid-state lithium secondary batteries using transmission electron microscopy. *Chem. Mater.* **22**, 949–956 (2010).

90. S. Wenzel, T. Leichtweiss, D. Krüger, J. Sann, J. Janek, Interphase formation on lithium solid electrolytes—An in situ approach to study interfacial reactions by photoelectron spectroscopy. *Solid State Ionics*. **278**, 98–105 (2015).

91. M. Tatsumisago, A. Hayashi, Sulfide Glass-Ceramic Electrolytes for All-Solid-State Lithium and Sodium Batteries. *International Journal of Applied Glass Science*. **5**, 226–235 (2014).

92. V. Palomares, P. Serras, I. Villaluenga, K. B. Hueso, J. Carretero-González, T. Rojo, Na-ion batteries, recent advances and present challenges to become low cost energy storage systems. *Energy Environ. Sci.* **5**, 5884 (2012).

93. L. P. Wang, L. Yu, X. Wang, M. Srinivasan, Z. J. Xu, Recent developments in electrode materials for sodium-ion batteries. *J. Mater. Chem. A Mater. Energy Sustain.* **3**, 9353–9378 (2015).

94. N. Yabuuchi, H. Yoshida, S. Komaba, Crystal Structures and Electrode Performance of Alpha-$NaFeO_2$ for Rechargeable Sodium Batteries. *Electrochemistry* . **80**, 716–719 (2012).

95. R. Kanno, M. Murayama, Lithium Ionic Conductor Thio-LISICON: The Li2 S - GeS2 - P 2 S 5 System. *J. Electrochem. Soc.* **148**, A742–A746 (2001).

96. S. Boulineau, M. Courty, J.-M. Tarascon, V. Viallet, Mechanochemical synthesis of Li-argyrodite Li6PS5X (X=Cl, Br, I) as sulfur-based solid electrolytes for all solid state batteries application. *Solid State Ionics*. **221**, 1–5 (2012).

97. F. Han, Y. Zhu, X. He, Y. Mo, C. Wang, Electrochemical Stability of Li 10 GeP 2 S 12 and Li 7 La 3 Zr 2 O 12 Solid Electrolytes. *Adv. Energy Mater.* **6**, 1501590 (2016).

98. Y. Mo, S. P. Ong, G. Ceder, First Principles Study of the Li10GeP2S12 Lithium Super Ionic Conductor Material. *Chem. Mater.* **24**, 15–17 (2012).

99. Y. Zhu, X. He, Y. Mo, Origin of Outstanding Stability in the Lithium Solid Electrolyte Materials: Insights from Thermodynamic Analyses Based on First-Principles Calculations. *ACS Appl. Mater. Interfaces*. **7**, 23685–23693 (2015).

100. R. Moshtev, V. Manev, A. Nassalevska, A. Gushev, G. Pistoia, Chemically desodiated thiochromites as cathode materials in secondary lithium cells. *J. Power Sources*. **26**, 285–292 (1989).

101. A. I. Popov, D. H. Geske, Studies on the Chemistry of Halogen and of Polyhalides. XIII. Voltammetry of Iodine Species in Acetonitrile. *J. Am. Chem. Soc.* **80**, 1340–1352 (1958).

102. L. Zhang, K. Yang, J. Mi, L. Lu, L. Zhao, L. Wang, Y. Li, H. Zeng, Na3PSe4: A Novel Chalcogenide Solid Electrolyte with High Ionic Conductivity. *Advanced Energy Materials*. **5**, 1501294 (2015).

103. A. Abouimrane, D. Dambournet, K. W. Chapman, P. J. Chupas, W. Weng, K. Amine, A new class of lithium and sodium rechargeable batteries based on selenium and selenium-sulfur as a positive electrode. *J. Am. Chem. Soc.* **134**, 4505–4508 (2012).

104. Z. Chen, Y. Qin, K. Amine, Redox shuttles for safer lithium-ion batteries. *Electrochim. Acta*. **54**, 5605–5613 (2009).

105. A. R. Wizansky, P. E. Rauch, F. J. Disalvo, Powerful oxidizing agents for the oxidative deintercalation of lithium from transition-metal oxides. *J. Solid State Chem.* **81**, 203–207 (1989).

106. J. C. Kim, X. Li, C. J. Moore, S. H. Bo, P. G. Khalifah, C. P. Grey, G. Ceder, Analysis of charged state stability for monoclinic LiMnBO3Cathode. *Chem. Mater.* **26**, 4200–4206 (2014).

107. A. Jain, S. P. Ong, G. Hautier, W. Chen, W. D. Richards, S. Dacek, S. Cholia, D. Gunter, D. Skinner, G. Ceder, K. A. Persson, Commentary: The Materials Project: A materials genome approach to accelerating materials innovation. *APL Materials*. **1**, 011002 (2013).

108. S. Geller, Refinement of the crystal structure of Co9S8. *Acta Crystallogr.* **15**, 1195–1198 (1962).

109. J. B. Parise, Structure of hazelwoodite (Ni3S2). *Acta Crystallogr. B.* **36**, 1179–1180 (1980).

110. A. Schwöbel, R. Hausbrand, W. Jaegermann, Interface reactions between LiPON and lithium studied by in-situ X-ray photoemission. *Solid State Ionics*. **273**, 51–54 (2015).

111. Z. Wang, J. Z. Lee, H. L. Xin, L. Han, N. Grillon, D. Guy-Bouyssou, E. Bouyssou, M. Proust, Y. S. Meng, Effects of cathode electrolyte interfacial (CEI) layer on long

term cycling of all-solid-state thin-film batteries. *J. Power Sources*. **324**, 342–348 (2016).

112. H. Kitaura, A. Hayashi, T. Ohtomo, S. Hama, M. Tatsumisago, Fabrication of electrode–electrolyte interfaces in all-solid-state rechargeable lithium batteries by using a supercooled liquid state of the glassy electrolytes. *J. Mater. Chem.* **21**, 118–124 (2010).

113. L. Xu, S. Tang, Y. Cheng, K. Wang, J. Liang, C. Liu, Y.-C. Cao, F. Wei, L. Mai, Interfaces in Solid-State Lithium Batteries. *Joule* (2018), doi:10.1016/j.joule.2018.07.009.

114. W. Zhang, F. H. Richter, S. P. Culver, T. Leichtweiss, J. G. Lozano, C. Dietrich, P. G. Bruce, W. G. Zeier, J. Janek, Degradation mechanisms at the Li10GeP2S12/LiCoO2 cathode interface in an all-solid-state lithium-ion battery. *ACS Appl. Mater. Interfaces*. **10**, 22226–22236 (2018).

115. S. P. Culver, R. Koerver, W. G. Zeier, J. Janek, On the Functionality of Coatings for Cathode Active Materials in Thiophosphate-Based All-Solid-State Batteries. *Advanced Energy Materials*. **0**, 1900626 (2019).

116. G. Oh, M. Hirayama, O. Kwon, K. Suzuki, R. Kanno, Bulk-Type All Solid-State Batteries with 5 V Class LiNi0.5Mn1.5O4 Cathode and Li10GeP2S12 Solid Electrolyte. *Chem. Mater.* **28**, 2634–2640 (2016).

117. K. H. Park, D. Y. Oh, Y. E. Choi, Y. J. Nam, L. Han, J. Y. Kim, H. Xin, F. Lin, S. M. Oh, Y. S. Jung, Solution-Processable Glass LiI-Li4SnS4 Superionic Conductors for All-Solid-State Li-Ion Batteries. *Adv. Mater.* **28**, 1874–1883 (2016).

118. J. W. Lee, Y. J. Park, Enhanced Cathode/Sulfide Electrolyte Interface Stability Using an Li_2ZrO_3 Coating for All-Solid-State Batteries. *J. Solid State Electrochem.* **9**, 176–183 (2018).

119. S. Ito, S. Fujiki, T. Yamada, Y. Aihara, Y. Park, T. Y. Kim, S.-W. Baek, J.-M. Lee, S. Doo, N. Machida, A rocking chair type all-solid-state lithium ion battery adopting Li2O–ZrO2 coated LiNi0.8Co0.15Al0.05O2 and a sulfide based electrolyte. *J. Power Sources*. **248**, 943–950 (2014).

120. S. Choi, B.-N. Yun, W. D. Jung, T. H. Kim, K.-Y. Chung, J.-W. Son, B.-I. Sang, H.-G. Jung, H. Kim, Tomographical analysis of electrochemical lithiation and

delithiation of LiNi0.6Co0.2Mn0.2O2 cathodes in all-solid-state batteries. *Scr. Mater.* **165**, 10–14 (2019).

121. H. Liu, P. K. Allan, O. J. Borkiewicz, C. Kurtz, C. P. Grey, K. W. Chapman, P. J. Chupas, A radially accessible tubular in situ X-ray cell for spatially resolved operando scattering and spectroscopic studies of electrochemical energy storage devices. *J. Appl. Crystallogr.* **49**, 1665–1673 (2016).

122. H. Tsukasaki, T. Uchiyama, K. Yamamoto, S. Mori, Y. Uchimoto, H. Kowada, A. Hayashi, M. Tatsumisago, Exothermal mechanisms in the charged LiNi1/3Mn1/3Co1/3O2 electrode layers for sulfide-based all-solid-state lithium batteries. *J. Power Sources*. **434**, 226714 (2019).

123. F. Walther, R. Koerver, T. Fuchs, S. Ohno, J. Sann, M. Rohnke, W. G. Zeier, J. Janek, Visualization of the interfacial decomposition of composite cathodes in argyrodite based all-solid-state batteries using time-of-flight secondary ion mass spectrometry. *Chem. Mater.* (2019), doi:10.1021/acs.chemmater.9b00770.

124. M. Gruber, A. Leitner, D. Kiener, P. Supancic, R. Bermejo, Incipient plasticity and surface damage in LiTaO3 and LiNbO3 single crystals. *Mater. Des.* **153**, 221–231 (2018).

125. D. Qian, C. Ma, K. L. More, Y. S. Meng, M. Chi, Advanced analytical electron microscopy for lithium-ion batteries. *NPG Asia Materials*. **7**, e193–e193 (2015).

126. X. B. Cheng, R. Zhang, C. Z. Zhao, Q. Zhang, Toward Safe Lithium Metal Anode in Rechargeable Batteries: A Review. *Chem. Rev.* **117**, 10403–10473 (2017).

127. X. Han, Y. Gong, K. K. Fu, X. He, G. T. Hitz, J. Dai, A. Pearse, B. Liu, H. Wang, G. Rubloff, Y. Mo, V. Thangadurai, E. D. Wachsman, L. Hu, Negating interfacial impedance in garnet-based solid-state Li metal batteries. *Nat. Mater.* **16**, 572–579 (2017).

128. C. Wang, Y. Gong, B. Liu, K. Fu, Y. Yao, E. Hitz, Y. Li, J. Dai, S. Xu, W. Luo, E. D. Wachsman, L. Hu, Conformal, Nanoscale ZnO Surface Modification of Garnet-Based Solid-State Electrolyte for Lithium Metal Anodes. *Nano Lett.* **17**, 565–571 (2017).

129. M. D. Tikekar, S. Choudhury, Z. Tu, L. A. Archer, Design principles for electrolytes and interfaces for stable lithium-metal batteries. *Nature Energy*. **1**, 16114 (2016).

130. X. Liang, Q. Pang, I. R. Kochetkov, M. S. Sempere, H. Huang, X. Sun, L. F. Nazar, A facile surface chemistry route to a stabilized lithium metal anode. *Nature Energy*. **2**, 17119 (2017).

131. Y. Lu, L. Li, Q. Zhang, Z. Niu, J. Chen, Electrolyte and Interface Engineering for Solid-State Sodium Batteries. *Joule*. **0** (2018), doi:10.1016/j.joule.2018.07.028.

132. J. W. Wang, X. H. Liu, S. X. Mao, J. Y. Huang, Microstructural evolution of tin nanoparticles during in situ sodium insertion and extraction. *Nano Lett*. **12**, 5897–5902 (2012).

133. S. Hao, D. S. Sholl, Role of Schottky Defects in Hydrogen and Metal Diffusion in NaH, MgH2, and NaMgH3. *J. Phys. Chem. Lett*. **1**, 2968–2973 (2010).

134. E. A. Wu, C. S. Kompella, Z. Zhu, J. Z. Lee, S. C. Lee, I.-H. Chu, H. Nguyen, S. P. Ong, A. Banerjee, Y. S. Meng, New Insights into the Interphase between the Na Metal Anode and Sulfide Solid-State Electrolytes: A Joint Experimental and Computational Study. *ACS Appl. Mater. Interfaces*. **10**, 10076–10086 (2018).

135. G. Dittmar, H. Schäfer, Die Kristallstruktur von Na3AsS4• 8 H2O/The Crystal Structure of Na3AsS4• 8 H2O. *Zeitschrift für Naturforschung B*. **33**, 678–681 (1978).

136. K. Mereiter, A. Preisinger, O. Baumgartner, G. Heger, W. Mikenda, H. Steidl, Hydrogen bonds in Na3AsS4. 8D2O: neutron diffraction, X-ray diffraction and vibrational spectroscopic studies. *Acta Crystallogr. B*. **38**, 401–408 (1982).

137. W. Sun, S. T. Dacek, S. P. Ong, G. Hautier, A. Jain, W. D. Richards, A. C. Gamst, K. A. Persson, G. Ceder, The thermodynamic scale of inorganic crystalline metastability. *Sci Adv*. **2**, e1600225 (2016).

138. X. Yu, J. B. Bates, G. E. Jellison, F. X. Hart, A Stable Thin - Film Lithium Electrolyte: Lithium Phosphorus Oxynitride. *J. Electrochem. Soc.* **144**, 524 – 532 (1997).

139. S. Zhao, Z. Fu, Q. Qin, A solid-state electrolyte lithium phosphorus oxynitride film prepared by pulsed laser deposition. *Thin Solid Films*. **415**, 108–113 (2002).

140. Y. Yamada, K. Usui, K. Sodeyama, S. Ko, Y. Tateyama, A. Yamada, Hydrate-melt electrolytes for high-energy-density aqueous batteries. *Nature Energy*. **1**, 16129 (2016).

141. S. L. Koch, B. J. Morgan, S. Passerini, G. Teobaldi, Density functional theory screening of gas-treatment strategies for stabilization of high energy-density lithium metal anodes. *J. Power Sources*. **296**, 150–161 (2015).

142. F. Sun, K. Dong, M. Osenberg, A. Hilger, S. Risse, Y. Lu, P. H. Kamm, M. Klaus, H. Markötter, F. García-Moreno, T. Arlt, I. Manke, Visualizing the morphological and compositional evolution of the interface of InLi-anode|thio-LISION electrolyte in an all-solid-state Li–S cell by in operando synchrotron X-ray tomography and energy dispersive diffraction. *J. Mater. Chem. A Mater. Energy Sustain.* **6**, 22489–22496 (2018).

143. D. Schröder, C. L. Bender, T. Arlt, M. Osenberg, A. Hilger, S. Risse, M. Ballauff, I. Manke, J. Janek, In operando x-ray tomography for next-generation batteries: a systematic approach to monitor reaction product distribution and transport processes. *J. Phys. D Appl. Phys.* **49**, 404001 (2016).

144. C. Zhao, T. Wada, V. De Andrade, D. Gürsoy, H. Kato, Y.-C. K. Chen-Wiegart, Imaging of 3D morphological evolution of nanoporous silicon anode in lithium ion battery by X-ray nano-tomography. *Nano Energy*. **52**, 381–390 (2018).

145. F. Shen, M. B. Dixit, X. Xiao, K. B. Hatzell, Effect of Pore Connectivity on Li Dendrite Propagation within LLZO Electrolytes Observed with Synchrotron X-ray Tomography. *ACS Energy Lett.* **3**, 1056–1061 (2018).

146. M. Agostini, U. Ulissi, D. Di Lecce, Y. Ahiara, S. Ito, J. Hassoun, A Lithium-Ion Battery based on an Ionic Liquid Electrolyte, Tin-Carbon Nanostructured Anode, and Li 2 O-ZrO 2 -Coated Li[Ni 0.8 Co 0.15 Al 0.05]O 2 Cathode. *Energy Technology*. **3**, 632–637 (2015).

147. A. P. Hammersley, Others, FIT2D: an introduction and overview. *European Synchrotron Radiation Facility Internal Report ESRF97HA02T*. **68**, 58 (1997).

148. S. P. Ong, W. D. Richards, A. Jain, G. Hautier, M. Kocher, S. Cholia, D. Gunter, V. L. Chevrier, K. A. Persson, G. Ceder, Python Materials Genomics (pymatgen): A robust, open-source python library for materials analysis. *Comput. Mater. Sci.* **68**, 314–319 (2013).

149. A. Belsky, M. Hellenbrandt, V. L. Karen, P. Luksch, New developments in the Inorganic Crystal Structure Database (ICSD): accessibility in support of materials research and design. *Acta Crystallogr. B*. **58**, 364–369 (2002).

150. P. E. Blöchl, Projector augmented-wave method. *Phys. Rev. B Condens. Matter.* **50**, 17953–17979 (1994).

151. J. P. Perdew, K. Burke, M. Ernzerhof, Generalized Gradient Approximation Made Simple. *Phys. Rev. Lett.* **77**, 3865–3868 (1996).

152. G. Kresse, J. Furthmüller, Efficient iterative schemes for ab initio total-energy calculations using a plane-wave basis set. *Phys. Rev. B Condens. Matter.* **54**, 11169–11186 (1996).

153. M. W. Chase, NIST - JANAF Thermochemical Tables for Oxygen Fluorides. *J. Phys. Chem. Ref. Data.* **25**, 551 – 603 (1996).

154. O. Kubaschewski, C. B. Alcock, P. J. Spencer, Materials Thermochemistry. Revised. *Pergamon Press Ltd, Headington Hill Hall, Oxford OX 3 0 BW, UK, 1993. 363* (1993).

155. J. Sangster, A. D. Pelton, The Na-S (Sodium-Sulfur) system. *J. Phase Equilib. Diffus.* **18**, 89 (1997).

156. A. Jain, G. Hautier, S. P. Ong, C. J. Moore, C. C. Fischer, K. A. Persson, G. Ceder, Formation enthalpies by mixing GGA and GGA+ U calculations. *Phys. Rev. B: Condens. Matter Mater. Phys.* **84**, 045115 (2011).

157. V. I. Anisimov VI, J. Zaanen, O. K. Andersen, Band theory and Mott insulators: Hubbard U instead of Stoner I. *Phys. Rev. B Condens. Matter.* **44**, 943–954 (1991).

158. S. L. Dudarev, G. A. Botton, S. Y. Savrasov, C. J. Humphreys, A. P. Sutton, Electron-energy-loss spectra and the structural stability of nickel oxide: An LSDA+ U study. *Phys. Rev. B: Condens. Matter Mater. Phys.* **57**, 1505 (1998).

159. H. Jónsson, G. Mills, K. W. Jacobsen, Nudged Elastic Band Method for Finding Minimum Energy Paths of Transitions (1998) (available at http://citeseerx.ist.psu.edu/viewdoc/summary?doi=10.1.1.31.531).

160. G. Henkelman, B. P. Uberuaga, H. Jónsson, A climbing image nudged elastic band method for finding saddle points and minimum energy paths. *J. Chem. Phys.* **113**, 9901–9904 (2000).